University of Glasgow

Iqbal, Rashid (2026) *Towards intelligent and adaptive optical wireless communications and sensing for 6G.* PhD thesis.

https://theses.gla.ac.uk/86329/

Copyright and moral rights for this work are retained by the author

A copy can be downloaded for personal non-commercial research or study, without prior permission or charge

This work cannot be reproduced or quoted extensively from without first obtaining permission from the author

The content must not be changed in any way or sold commercially in any format or medium without the formal permission of the author

When referring to this work, full bibliographic details including the author, title, awarding institution and date of the thesis must be given

Enlighten: Theses
https://theses.gla.ac.uk/
research-enlighten@glasgow.ac.uk

Towards Intelligent and Adaptive Optical Wireless Communications and Sensing for 6G

Rashid Iqbal

SUBMITTED IN FULFILMENT OF THE REQUIREMENTS FOR THE DEGREE OF
DOCTOR OF PHILOSOPHY

JAMES WATT SCHOOL OF ENGINEERING



28/09/2026

Abstract

Future sixth generation (6G) networks are expected to support high-speed communication together with secure, adaptive, and environment-aware operation. Meeting these requirements motivates the use of complementary wireless technologies that can provide additional bandwidth while supporting precise spatial control. Optical wireless communication (OWC) is promising in this context because it offers large unlicensed bandwidth, spatial confinement, immunity to radio-frequency electromagnetic interference, and the potential to support communication, localisation, and sensing. Within the broader OWC family, visible light communication (VLC) is particularly attractive for indoor environments because visible light can be used for both illumination and wireless transmission. However, the performance of indoor optical wireless systems remains strongly dependent on blockage, user orientation, receiver field-of-view (FoV), transmitter–receiver geometry, and the presence of eavesdroppers.

These limitations motivate the development of optical wireless systems that can actively control propagation and obtain information about their surrounding environment. Accordingly, this thesis investigates intelligent and adaptive OWC and sensing techniques for future indoor 6G networks. The research focuses on improving security, spatial adaptability, and environmental awareness through optical reconfigurable intelligent surfaces (ORISs), light-emitting reconfigurable intelligent surfaces (LeRISs), and adaptive beam-management techniques.

First, to address the security limitations of conventional indoor VLC, ORIS-assisted VLC is investigated for physical layer security (PLS). The proposed approach exploits ORIS-induced propagation delays to control the reflected optical paths and improve the secrecy of the legitimate link. For the single-eavesdropper worst-case geometry, the proposed ORIS allocation improves the secrecy capacity by 253.7% at an optical transmit power of 3 W compared with the line-of-sight (LoS)-only case. When the analysis is extended to multiple eavesdroppers, the proposed proximal policy optimisation (PPO)-based allocation achieves secrecy-capacity improvements of up to 235% compared with allocating all ORIS elements to the legitimate receiver.

Building on this ability to control reflected optical paths, the second part of the thesis focuses on where the reflected beams are directed. A geometry-aware non-uniform codebook is therefore developed for ORIS-assisted VLC to improve spatial coverage and support multi-user resource allocation. When combined with sparrow search algorithm (SSA)-based power allocation, the proposed LoS+ORIS framework increases the sum rate from approximately 4.4 bps/Hz to 9.6 bps/Hz over the considered ORIS-size range while maintaining improved multi-user fairness.

While adaptive beam control improves communication performance, further adaptability requires knowledge of the user location and surrounding obstacles. The third part of the thesis therefore extends the reconfigurable surface from communication control to environmental awareness through a vertical-cavity surface-emitting laser (VCSEL)-based LeRIS architecture. Narrow VCSEL beams are used for user localisation and obstacle mapping, and the resulting spatial information is then used to support blockage-aware millimetre wave (mmWave) communication. For the considered simulation settings, the proposed VCSEL-based architecture achieves millimetre-level localisation accuracy, compared with centimetre-level accuracy for a light-emitting diode (LED)-based LeRIS benchmark, while the localisation and mapping information enables adaptive route selection and improved blockage resilience.

Overall, the three contributions follow a common progression from securing the optical link, to controlling the spatial distribution of reflected beams, and finally to using optical sensing to make the communication environment aware of users and obstacles. The results demonstrate that programmable optical surfaces, optical sensing, and adaptive beam management can jointly improve the security, adaptability, and environmental awareness of indoor wireless systems, contributing towards intelligent OWC and sensing for future 6G networks.

Contents

Abstract ii

List of Tables vi

List of Figures vii

List of Publications x

Acknowledgements xii

Dedication xiii

Declaration xiv

Abbreviations xv

List of Symbols xviii

1 Introduction 1

1.1 Motivation 1

1.2 Contributions 7

1.3 Thesis Outline 8

2 Background and Related Work 10

2.1 Introduction 10

2.2 Optical Wireless System Structure 14

2.2.1 Basic Structure 14

2.2.2 Optical Transmitters 16

2.2.3 Optical Receivers . . . 19
2.2.4 Optical Channel Model . . . 21
2.2.5 Noise Modelling in Optical Wireless Systems . . . 25
2.2.6 Achievable Data Rate . . . 26
2.2.7 Blockage and Mobility . . . 27
2.3 ORIS and LeRIS . . . 27
2.3.1 Basic Concept . . . 27
2.3.2 ORIS . . . 28
2.3.3 LeRIS . . . 31
2.3.4 Practical Design Considerations . . . 32
2.4 Physical Layer Security . . . 33
2.4.1 Security in VLC . . . 33
2.4.2 ORIS-Assisted PLS . . . 34
2.4.3 Delay-Aware Security . . . 35
2.5 Codebook Design and Multiple Access . . . 36
2.5.1 Codebook-Based Beam Steering . . . 36
2.5.2 Non-Uniform Codebook Design . . . 36
2.5.3 Resource Allocation in NOMA . . . 38
2.6 Optical Localisation and Sensing . . . 39
2.6.1 Optical Wireless Positioning . . . 39
2.6.2 VCSEL-Based Localisation and Sensing . . . 41
2.6.3 Environment-Aware mmWave Communication . . . 42
2.7 Summary . . . 43

3 Delay-Aware Physical Layer Security in ORIS-Assisted VLC Systems 46
3.1 Introduction . . . 46
3.2 System and Channel Model . . . 49
3.2.1 ORIS-Assisted Indoor VLC Network . . . 49
3.2.2 Channel Model and ORIS-Induced Time Delay . . . 50
3.3 Secrecy Performance Analysis . . . 54

3.3.1 Single-Eavesdropper Scenario 55
3.3.2 Single-Eavesdropper Scenario 56
3.3.3 Multiple-Eavesdropper Scenario 57
3.3.4 Approximate Secrecy Analysis 58
3.4 Delay-Aware ORIS Element Allocation and Optimisation 61
3.4.1 ORIS Element Allocation Problem 61
3.4.2 GA-Based Allocation 62
3.4.3 PPO-Based Allocation 65
3.5 Simulation Results and Discussion 67
3.5.1 Simulation Setup 67
3.5.2 Single-Eavesdropper Results 71
3.5.3 Multiple-Eavesdropper Results 73
3.6 Summary 76

4 Codebook Design for ORIS-Assisted VLC Systems 78
4.1 Introduction 78
4.2 System Model 81
4.2.1 LoS and ORIS-Assisted Channel 82
4.2.2 Codebook-Based ORIS Beam Steering 84
4.3 Geometric-Optics-Based Non-Uniform Codebook Design 86
4.3.1 Mirror Orientation and Reflected Beam Mapping 86
4.3.2 Uniform Angular Codebook and Spatial Mapping Limitation . . 87
4.3.3 Element-Wise Non-Uniform Codebook Design 90
4.3.4 Codebook Error Metric 92
4.4 NOMA-Based ORIS Resource Allocation 94
4.4.1 Effective Channel and NOMA Signal Model 94
4.4.2 Fairness-Aware Optimisation Problem 96
4.4.3 QoS-Oriented ORIS Element Allocation 97
4.4.4 GRPA and SSA Power Allocation 98
4.5 Simulation Results and Discussion 100

4.5.1 Simulation Setup . . . 101
4.5.2 Uniform and Non-Uniform Codebook Comparison . . . 103
4.5.3 Codebook Error Performance . . . 104
4.5.4 NOMA Sum-Rate and Fairness Performance . . . 106
4.6 Summary . . . 111

5 Integrated Localisation, Mapping, and Communication Through VCSEL-Based LeRIS 113

5.1 Introduction . . . 113
5.2 System and Channel Model . . . 116
5.2.1 VCSEL-Based LeRIS Architecture . . . 116
5.2.2 Optical VCSEL Channel Model . . . 117
5.2.3 mmWave Communication Model . . . 119
5.3 VCSEL-Based Localisation and Mapping . . . 123
5.3.1 Closed-Form User Localisation . . . 123
5.3.2 Dual-Mode VCSEL Localisation . . . 126
5.3.3 VCSEL-Based Obstacle Mapping . . . 129
5.4 LeRIS-Assisted Communication . . . 132
5.4.1 Obstacle-Aware Route Selection . . . 133
5.4.2 TDMA-Based Multi-User Rate Optimisation . . . 134
5.5 Simulation Results and Discussion . . . 135
5.5.1 Simulation Setup . . . 136
5.5.2 Localisation Performance . . . 138
5.5.3 Spectral Efficiency Performance . . . 139
5.5.4 Obstacle-Aware Communication Performance . . . 141
5.5.5 Multi-User Fairness Performance . . . 143
5.6 Summary . . . 143
Appendix A: Levenberg–Marquardt Method for VCSEL-Based Localisation . 146

6 Conclusion and Future Work 148

6.1 Concluding Remarks 148
6.2 Future Work 150

References **153**

List of Tables

3.1 Simulation parameters for the delay-aware ORIS-assisted VLC system. . . . 70

4.1 Simulation parameters for the ORIS-assisted NOMA-VLC system. 102

5.1 Simulation parameters for VCSEL-based localisation and sensing. 137

5.2 Simulation parameters for mmWave communication. 137

List of Figures

1.1 Growth of global Internet users from 2026 to 2031 [3]. 2

1.2 Growth of connected IoT devices worldwide from 2026 to 2031 [4]. 3

2.1 Overall concept of the proposed indoor OWC and sensing framework. . . . 13

2.2 Basic indoor OWC system based on IM/DD. 14

2.3 Lambertian radiation profiles for different emission orders. 17

2.4 Normalised far-field Gaussian-like intensity profiles of VCSEL beams with different divergence angles. 19

2.5 Illustration of a typical indoor VLC system consisting of an optical transmitter, optical channel, receiver concentrator, and photodetector. 21

2.6 Propagation model of diffuse link. 23

2.7 Illustration of Gaussian beam radius variation with propagation distance, showing the beam waist w_0 and Rayleigh range z_{R}. 25

2.8 ORIS-assisted VLC system with controllable specular reflection. 29

2.9 Indoor PWE with VCSEL-based LeRIS panels for localisation, obstacle mapping, and mmWave communication. 32

2.10 ORIS-assisted VLC PLS model with a legitimate receiver and an eavesdropper. 34

2.11 Uniform and non-uniform angular codebooks and their corresponding spatial mapping on the receiver plane. 37

3.1 Indoor ORIS-assisted VLC system with one legitimate receiver and multiple passive eavesdroppers. 50

3.2 Illustration of the effect of path-delay difference on the normalised channel gain. 53

3.3 Convergence behaviour of the GA-based ORIS element allocation for different ORIS sizes. 71
3.4 Secrecy-rate difference for the single-eavesdropper worst-case scenario, where Eve is closer to the LED than Bob. 72
3.5 PPO training convergence for colluding and non-colluding eavesdroppers with different ORIS sizes. 74
3.6 Achievable rates versus transmit optical power for the multiple-eavesdropper worst-case geometry under the colluding eavesdropping case. 75
3.7 Achievable rates versus transmit optical power for the multiple-eavesdropper worst-case geometry under the non-colluding eavesdropping case. 76
3.8 Validation of the approximate analytical rate expression against exact numerical integration. 77

4.1 Indoor ORIS-assisted VLC system with a ceiling LED, wall-mounted ORIS, and multiple users on the receiver plane. 83
4.2 Specular reflection geometry of one ORIS mirror element, showing the incident direction, mirror normal, reflected direction, and the corresponding beam-hit point on the receiver plane. 88
4.3 Illustration of the tilt-angle effect on the reflected beam-hit position. For a fixed sweep angle, different tilt states produce different beam-hit distances on the receiver plane. 89
4.4 Illustration of the sweep-angle effect on the reflected beam-hit position. For a fixed tilt angle, changing the sweep angle moves the beam-hit point along the same receiver-plane ring. 90
4.5 Spatial mapping comparison between uniform and non-uniform codebooks on the receiver plane. 103
4.6 Frobenius norm error versus tilt step for different sweep-step values. 105
4.7 Frobenius norm error versus sweep step for different tilt-step values. 106
4.8 Number of candidate beams versus coverage radius for different tilt-step values. 107
4.9 Sum rate versus number of ORIS elements for $K = 3$ users. 108

4.10 Jain fairness index versus number of ORIS elements for $K = 3$ users. 109
4.11 Sum rate versus maximum transmit power for $K = 3$, 5, and 7 users. 110
4.12 Jain fairness index versus maximum transmit power for $K = 3$, 5, and 7 users. 110
4.13 Sum rate versus number of users. 111

5.1 Indoor PWE with VCSEL-based LeRIS panels for localisation, mapping, and mmWave communication. 117
5.2 VCSEL coverage from multiple LeRIS panels. 130
5.3 Reference geometry for UE azimuth orientation with respect to the four LeRIS panels. 138
5.4 Localisation error versus UE azimuth orientation for different numbers of active LeRIS panels. 139
5.5 Spectral efficiency versus transmit SNR for different numbers of participating LeRIS panels. 140
5.6 Spectral efficiency versus number of reflecting elements for different numbers of LeRIS panels. 141
5.7 Spectral efficiency versus transmit SNR for different numbers of obstacles: (a) one active LeRIS panel and (b) four active LeRIS panels. 142
5.8 CDF of the minimum user rate for different numbers of participating LeRIS panels: (a) single-user case and (b) multi-user case. 144

List of Publications

Journal Papers

1. R. Iqbal, M. Biagi, A. Zoha, M. A. Imran, and H. Abumarshoud, "Leveraging IRS-Induced Time Delay for Enhanced Physical Layer Security in VLC Systems," *IEEE Wireless Commun. Lett.*, vol. 13, no. 11, pp. 3147–3151, 2024.
2. R. Iqbal, A. Zoha, S. Ikki, M. A. Imran, and H. Abumarshoud, "Enhancing PLS of Indoor IRS-VLC Systems for Colluding and Non-Colluding Eavesdroppers," *IEEE Open J. Commun. Soc.*, 2026.
3. R. Iqbal, D. Bozanis, D. Tyrovolas, C. K. Liaskos, M. A. Imran, G. K. Karagiannidis, and H. Abumarshoud, "Integrated Localisation, Mapping, and Communication Through VCSEL-Based Light-Emitting RIS (LeRIS)," submitted to *IEEE Internet Things J.*
4. R. Iqbal, D. Bozanis, D. Tyrovolas, C. K. Liaskos, M. A. Imran, G. K. Karagiannidis, and H. Abumarshoud, "Non-Uniform Codebook Design for Uniform Spatial Mapping with NOMA-Based OIRS-Assisted VLC," submitted to *IEEE Trans. Netw. Sci. Eng.*

Conference Papers

1. R. Iqbal, D. Bozanis, D. Tyrovolas, C. K. Liaskos, M. A. Imran, G. K. Karagiannidis, and H. Abumarshoud, "Enabling mmWave Communications with VCSEL-Based Light-Emitting Reconfigurable Intelligent Surfaces," in *Proc. IEEE Int. Conf. Commun. (ICC)*, 2026.

2. R. Iqbal, D. Bozanis, D. Tyrovolas, C. K. Liaskos, M. A. Imran, G. K. Karagiannidis, and H. Abumarshoud, "Non-Uniform Codebook Design for Optical IRS-Assisted VLC Systems," in *Proc. IEEE Int. Balkan Conf. Commun. Netw. (BalkanCom)*, 2026.

Acknowledgements

First and foremost, I am deeply grateful to Almighty God for giving me the strength, patience, and guidance to complete this PhD journey.

I would like to express my sincere gratitude to my supervisor, Dr. Hanaa Abumarshoud, for her continuous support, guidance, and encouragement throughout my research. I am also thankful to my co-supervisors, Dr. Ahmed Zoha and Professor Muhammad Imran, for their valuable advice, feedback, and support during this work.

I would also like to sincerely thank Professor George K. Karagiannidis, Dimitris Tyrovolas, and Dimitris Bozanis for their valuable collaboration, insightful discussions, and support during my three-month research visit in Greece as a visiting PhD researcher. Their guidance and collaboration contributed significantly to the development of part of the research presented in this thesis.

I would like to thank my family for their love, prayers, and constant encouragement. Their support has been a great source of strength throughout this journey.

Finally, I am grateful to my friends and colleagues for their kindness, motivation, and support during my PhD studies.

Dedication

To my beloved late mother, Bibi Robina. Your love, prayers, and sacrifices continue to guide me at every step of my life. This thesis is dedicated to your memory, with the deepest love, respect, and gratitude.

Declaration

I declare that, except where explicit reference is made to the contribution of others, this dissertation is the result of my own work and has not been submitted for any other degree at the University of Glasgow or any other institution.

Rashid Iqbal

Abbreviations

3D	three-dimensional
5G	fifth generation
6G	sixth generation
AoA	angle of arrival
AP	access point
APD	avalanche photodiode
AWGN	additive white Gaussian noise
CDF	cumulative distribution function
DC	direct current
DCO-OFDM	direct current-biased optical orthogonal frequency division multiplexing
FDMA	frequency division multiple access
FoV	field-of-view
FSO	free-space optical communication
GA	genetic algorithm
GAE	generalised advantage estimation
GO	geometric optics
GRPA	gain ratio power allocation
IEEE	Institute of Electrical and Electronics Engineers
IM/DD	intensity modulation/direct detection
IoT	Internet of Things
ISAC	integrated sensing and communication
ISI	inter-symbol interference

LED	light-emitting diode
LeRIS	light-emitting reconfigurable intelligent surface
LiDAR	light detection and ranging
LiFi	light fidelity
LoS	line-of-sight
MIMO	multiple-input multiple-output
mmWave	millimetre wave
NLoS	non-line-of-sight
NOMA	non-orthogonal multiple access
OCC	optical camera communication
OFDM	orthogonal frequency division multiplexing
OFDMA	orthogonal frequency division multiple access
ORIS	optical reconfigurable intelligent surface
WCL	Wireless Communications Letters
OJCOM	Open Journal of the Communications Society
OWC	optical wireless communication
PD	photodiode
PLS	physical layer security
PPO	proximal policy optimisation
PWE	programmable wireless environment
QoS	quality of service
RF	radio frequency
RIN	relative intensity noise
RL	reinforcement learning
RSS	received signal strength
SIC	successive interference cancellation
SINR	signal-to-interference-plus-noise ratio
SNR	signal-to-noise ratio
SSA	sparrow search algorithm

TDMA	time division multiple access
TDoA	time difference of arrival
THz	terahertz
ToA	time of arrival
UE	user equipment
UWB	ultra-wideband
VCSEL	vertical-cavity surface-emitting laser
VLC	visible light communication
VLP	visible light positioning

List of Symbols

P_{t} Transmit power

P_{r} Received optical power

$x(t)$ Transmitted signal

$y(t)$ Received signal

$n(t)$ Additive noise

h Optical wireless channel gain

h_{LoS} Line-of-sight channel gain

h_{NLoS} Non-line-of-sight channel gain

d Distance between the transmitter and receiver

ϕ Irradiance angle

ψ Incidence angle

$\Phi_{1/2}$ Semi-angle at half optical power

Ψ_{c} Receiver field-of-view

m Lambertian emission order

A_{PD} Active area of the photodetector

R_{PD} Photodetector responsivity

$T_{\mathrm{s}}(\psi)$ Optical filter gain

$g(\psi)$ Optical concentrator gain

n_{r} Refractive index of the optical concentrator

B System bandwidth

N_0 Noise power spectral density

σ^2 Noise variance

I_{bg} Background light-induced current

q Electron charge

k_{B} Boltzmann constant

T_{k} Absolute temperature

C Channel capacity

R Achievable data rate

R_{s} Secrecy rate

γ Signal-to-noise ratio

N Number of reflecting elements

ρ Reflection coefficient

α Reflection angle

$\mathscr{C}$ Codebook

$\mathbf{c}_i$ The ith codeword in the codebook

K Number of users

λ Wavelength or Lagrange multiplier, depending on context

η Optical or electrical conversion efficiency

ϑ_n Tilt angle of the nth ORIS element

φ_n Sweep angle of the nth ORIS element

$\hat{\mathbf{N}}_n$ Unit normal vector of the nth reflecting element

$\mathbf{d}_{\mathrm{in},n}$ Incident unit direction at the nth reflecting element

$\mathbf{d}_{\mathrm{out},n}$ Reflected unit direction from the nth reflecting element

$\mathbf{P}_{\mathrm{hit},n}$ Hit point of the reflected beam from the nth reflecting element

$H_{\mathrm{LoS}}(0)$ Direct current line-of-sight channel gain

$H_{\mathrm{NLoS}}(0)$ Direct current non-line-of-sight channel gain

$\mathbf{p}_{\mathrm{t}}$ Position vector of the optical transmitter

$\mathbf{p}_{\mathrm{r}}$ Position vector of the optical receiver

$\mathbf{u}_{\mathrm{r}}$ Unit orientation vector of the receiver

w_0 Beam waist of the VCSEL beam

$w(d)$ Beam radius at distance d

z_{R} Rayleigh range

$H_{\mathrm{ORIS}}(0)$ Direct current ORIS-assisted reflected channel gain

$H_{\mathrm{ORIS},n}(0)$ Reflected channel gain through the nth ORIS element

A_n Area of the nth ORIS reflecting element

$d_{\mathrm{t},n}$ Distance from the transmitter to the nth ORIS element

$\phi_{\mathrm{t},n}$ Irradiance angle from the transmitter to the nth ORIS element

$\psi_{\mathrm{s},n}$ Incidence angle on the nth ORIS reflecting surface

$A_{\mathrm{spot},n}$ Beam spot area produced by the nth reflected beam at the receiver plane

$\psi_{\mathrm{r},n}$ Incidence angle of the nth reflected beam at the receiver

χ_n Visibility and alignment indicator of the nth ORIS element

$\mathscr{A}_{\mathrm{r}}$ Receiver detection region

R_{B} Achievable rate of the legitimate receiver

R_{E} Achievable rate of the eavesdropper

C_{s} Secrecy capacity

γ_{B} Signal-to-noise ratio at the legitimate receiver

γ_{E} Signal-to-noise ratio at the eavesdropper

τ_n Propagation delay introduced by the nth reflected path

$\mathbf{p}_i$ Position vector of the ith optical anchor

$\mathbf{p}_{\mathrm{u}}$ Position vector of the user

$\hat{\mathbf{p}}_{\mathrm{u}}$ Estimated position vector of the user

d_i Distance between the ith optical anchor and the user

$P_{\mathrm{r},i}$ Received optical power from the ith optical anchor

τ_i Time of arrival from the ith optical anchor

$\mathscr{O}$ Set of detected obstacles

$\mathbf{p}_{\mathrm{o}}$ Position vector of an obstacle

$\mathscr{C}_n$ Codebook of the nth ORIS element

L_n Number of codewords for the nth ORIS element

$\mathbf{c}_{n,\ell}$ The ℓth codeword of the nth ORIS element

$\vartheta_{n,\ell}$ Tilt angle in the ℓth codeword of the nth ORIS element

$\varphi_{n,\ell}$ Sweep angle in the ℓth codeword of the nth ORIS element

$\mathbf{q}_{n,\ell}$ Desired spatial target point associated with the ℓth codeword

$e_{n,\ell}$ Spatial mapping error of the ℓth codeword of the nth ORIS element

a_k NOMA power allocation coefficient of the kth user

s_k Information-bearing signal of the kth user

M Number of eavesdroppers

k Generic receiver index

$\mathbf{p}_{\mathrm{B}}$ Position vector of the legitimate receiver

$\mathbf{p}_{\mathrm{E},m}$ Position vector of the mth eavesdropper

D Separation distance between adjacent reflecting elements

$\mathbf{s}$ ORIS element allocation vector

s_n Allocation state of the nth ORIS element

$\mathbf{s}^{\star}$ Optimal ORIS element allocation vector

$\mathbf{s}^{\star}_{\mathrm{NC}}$ Optimal ORIS allocation vector for the non-colluding case

$\mathbf{s}^{\star}_{\mathrm{C}}$ Optimal ORIS allocation vector for the colluding case

$\mathbf{s}^{\star}_{\mathrm{GA}}$ ORIS allocation vector obtained by the genetic algorithm

$h_{k,n}$ Reflected channel gain from the nth ORIS element to receiver k

$d_{k,\mathrm{LED}}$ Distance between Alice and receiver k

$d_{\mathrm{LED},n}$ Distance between Alice and the nth ORIS element

$d_{k,n}$ Distance between the nth ORIS element and receiver k

$\tau_{k,\mathrm{LED}}$ Propagation delay of the direct LoS path to receiver k

$\tau_{k,n,\mathrm{LED}}$ Propagation delay of the nth ORIS element to receiver k

$\Delta\tau_{k,n}$ Delay difference between the direct and reflected paths for receiver k

$q_k(t)$ Channel impulse response of receiver k

$Q_k(f)$ Channel frequency response of receiver k

$\gamma_k(f)$ Frequency-dependent signal-to-noise ratio of receiver k

$\gamma_{\mathrm{E},m}(f)$ Frequency-dependent signal-to-noise ratio at the mth eavesdropper

$\gamma^{\mathrm{C}}_{\mathrm{E}}(f)$ Effective signal-to-noise ratio of the colluding eavesdropping group

R_k Achievable rate of receiver k

$R_{\mathrm{E},m}$ Achievable rate of the mth eavesdropper

$R_{\mathrm{E}}^{\mathrm{C}}$ Achievable rate of the colluding eavesdropping group

$C_{\mathrm{s}}^{\mathrm{NC}}$ Secrecy capacity under non-colluding eavesdroppers

$C_{\mathrm{s}}^{\mathrm{C}}$ Secrecy capacity under colluding eavesdroppers

T_{sym} Symbol period

$E(f)$ Power distribution over frequency

Γ Gap between theoretical and practical system performance

κ Modulation scaling factor

$G_{\mathrm{LoS},k}$ Direct LoS gain of receiver k

$G_{i,k}$ Reflected gain through the ith ORIS element to receiver k

$\tau_{\mathrm{LoS},k}$ LoS delay of receiver k

$\tau_{i,k}$ Reflected-path delay through the ith ORIS element to receiver k

Λ Frequency-independent SNR coefficient

D_k Frequency-independent rate term of receiver k

$N_k(f)$ Frequency-dependent delay term of receiver k

R_k^{approx} Approximate achievable rate of receiver k

$C_{\mathrm{s,approx}}^{\mathrm{NC}}$ Approximate secrecy capacity under non-colluding eavesdroppers

$C_{\mathrm{s,approx}}^{\mathrm{C}}$ Approximate secrecy capacity under colluding eavesdroppers

$F(\mathbf{s})$ Fitness function of the ORIS allocation vector

$\mathscr{P}$ Population of candidate ORIS allocation vectors

$\mathbf{o}_t$ Observation at time step t

a_t Action selected at time step t

r_t Reward at time step t

r_t^{NC} Reward for the non-colluding eavesdropping case

r_t^{C} Reward for the colluding eavesdropping case

$\pi_\theta(a_t|\mathbf{o}_t)$ Allocation policy parameterised by θ

$J(\theta)$ Expected cumulative discounted reward

ζ Discount factor

T_{ep} Episode length

$r_t(\theta)$ PPO probability ratio

θ Policy parameters

θ_{old} Policy parameters before the PPO update

$L^{\text{CLIP}}(\theta)$ Clipped PPO objective function

$\hat{A}_t$ Estimated advantage function at time step t

ε PPO clipping parameter

i VCSEL index

ℓ Route-segment index

$P_{\text{t},i}$ Optical transmit power of the ith VCSEL

N_{V} Number of received VCSEL signals

$I_{i,k}(r_0, d_0)$ Gaussian intensity profile from the ith VCSEL to the kth UE

r_0 Radial distance from the VCSEL beam centre

d_0 Axial distance from the VCSEL source

$d_{i,k}$ Distance between the ith VCSEL and the kth UE

λ_{o} Optical wavelength of the VCSEL channel

θ_{div} Divergence angle of the VCSEL beam

$P_{\text{LoS},i,k}$ LoS optical power received from the ith VCSEL at the kth UE

$P_{\text{r},i,k}$ Total received optical power from the ith VCSEL at the kth UE

$P_{\text{n},i,k}$ Optical noise power from the ith VCSEL to the kth UE

B_{o} Effective optical bandwidth

$S_{i,k}$ Single-sided noise power spectral density for the ith VCSEL to the kth UE

A_{K} Thermal noise coefficient

RIN Relative intensity noise

F_{n} Preamplifier noise figure

R_{L} Load resistance

Ψ Half-angle field-of-view of the UE receiver

M_{x} Number of reflecting elements along the horizontal dimension of the LeRIS panel

N_{y} Number of reflecting elements along the vertical dimension of the LeRIS panel

η_{eff} Aperture efficiency of the LeRIS panel

$G(\theta, \varphi)$ Directional gain of the LeRIS panel

$F(\theta, \varphi)$ Far-field radiation pattern of the LeRIS array

k_0 mmWave wavenumber

λ_{m} Wavelength of the mmWave channel

$\zeta_{mn}(\theta, \varphi)$ Geometry-dependent phase term of the (m,n)th LeRIS element

ω_{mn} Propagation phase offset of the (m,n)th LeRIS element

Φ_{mn} Phase shift applied by the (m,n)th LeRIS element

$(x_{\mathrm{T}}, y_{\mathrm{T}}, z_{\mathrm{T}})$ Position of the transmitting or reflecting node

$(x_{\mathrm{R}}, y_{\mathrm{R}}, z_{\mathrm{R}})$ Position of the receiving node centre

$(\hat{\theta}_{\mathrm{r},k}, \hat{\varphi}_{\mathrm{r},k})$ Estimated direction of the kth UE

$(\theta_{\mathrm{u},k}, \varphi_{\mathrm{u},k})$ True direction of the kth UE

$G_{\max}$ Maximum LeRIS directional gain under perfect beam alignment

G_{cas} Cascaded gain of the first $L-1$ LeRIS panels

A_{eff} Effective aperture of the LeRIS panel

$G_L(\theta_{\mathrm{u},k}, \varphi_{\mathrm{u},k})$ Directional gain of the final LeRIS panel towards the true UE direction

$G_{\mathrm{r},k}$ Total directional route gain for the kth UE

G_{t} Transmit antenna gain

G_{r} Receive antenna gain

L Number of participating LeRIS panels

y_k Baseband signal received by the kth UE

x Transmitted symbol with unit energy

w_k Additive white Gaussian noise at the kth UE

σ_k^2 Noise variance at the kth UE

l_{p} Total path loss of the selected cascaded route

$d_{\mathrm{r},\ell}$ Distance of the ℓth route segment

$d_{\mathrm{r},0}$ Reference distance

n_ℓ Path loss exponent of the ℓth route segment

C_0 Free-space path loss at the reference distance

γ_{t} Transmit signal-to-noise ratio

$\mathbf{r}$ UE position vector

$\hat{\mathbf{r}}$ Estimated UE position vector

$\mathbf{s}_i$ Position vector of the ith VCSEL

$\mathbf{n}$ UE orientation vector

$\hat{\mathbf{n}}(\mathbf{r})$ Estimated orientation vector for position $\mathbf{r}$

$\mathbf{u}_i$ Unit direction vector from the UE to the ith VCSEL

$\mathbf{p}$ Vector of measured received optical powers

$\mathbf{V}(\mathbf{r})$ Localisation measurement matrix

$\beta_i(d_i)$ Distance-dependent optical power scaling of the ith VCSEL

$J(\mathbf{r})$ Variable-projection localisation cost function

$\mathbf{I}_3$ Three-dimensional identity matrix

$\mathbf{e}(\mathbf{r})$ Residual vector for VCSEL-based localisation

$f_i(\mathbf{r}, \mathbf{n})$ Residual term for the ith VCSEL measurement

$\mathbf{J}$ Jacobian matrix of the residual vector

μ Levenberg–Marquardt damping parameter

$\Delta\mathbf{r}$ Position update vector

$\varepsilon_{\mathrm{LM}}$ Position-update convergence threshold

ε_{J} Cost-function convergence threshold

π Candidate LeRIS-assisted communication route

$\mathscr{S}(\pi)$ Set of individual segments forming route π

s Individual segment of a candidate route

χ_s Binary availability indicator of segment s

$\chi_{\pi,k}$ Binary availability indicator of route π for the kth UE

$R_{\pi,k}$ Spectral efficiency of the kth UE through route π

$l_{\mathrm{p}}(\pi)$ Total path loss of route π

$G_{\mathrm{r},k}(\pi)$ Cascaded directional gain of route π for the kth UE

τ_k TDMA time-allocation factor for the kth UE

$R_{\min}$ Minimum achievable user rate

$\mathscr{K}$ Set of UEs

x_{u} Horizontal x-coordinate of a UE

y_{u} Horizontal y-coordinate of a UE

z_{u} Height coordinate of a UE

φ_{UE} Azimuth orientation angle of a UE

θ_{UE} Elevation orientation angle of a UE

O_{b} Number of blocking objects

$\Delta d_{i,k}$ Localisation distance error for the ith VCSEL and the kth UE

L_x, L_y, L_z Room dimensions along the x-, y- and z-axes

$\mathbf{L}$ Position vector of the ceiling LED transmitter

$\mathbf{U}_k$ Position vector of the kth user

$\mathbf{R}_n$ Position vector of the nth ORIS reflecting element

a Side length of each square ORIS reflecting element

δ Mirror reflectivity of the ORIS element

$h_{\mathrm{LoS},k}$ Direct LoS channel gain of the kth user

$h_n(\mathbf{R}_n, \mathbf{U}_k)$ Reflected channel gain from the nth ORIS element to user k

$h_{\mathrm{ORIS},k}$ Total ORIS-assisted reflected channel gain of user k

$h_{\mathrm{total},k}$ Total optical channel gain of user k

$d_{\mathrm{LoS},k}$ Distance between the LED and user k

$d_{1,n}$ Distance between the LED and the nth ORIS element

$d_{2,n,k}$ Distance between the nth ORIS element and user k

$\phi_{\mathrm{LoS},k}$ Irradiance angle of the direct LoS path to user k

$\psi_{\mathrm{LoS},k}$ Incidence angle of the direct LoS path at user k

ϕ_n Irradiance angle from the LED towards the nth ORIS element

$\psi_{n,k}$ Incidence angle at user k for the reflected path from element n

$\mathbf{Q}_{n,k}$ Backward-ray intersection point from element n to user k

$\mathscr{L}$ Valid LED aperture region

$\mathbb{I}(\cdot)$ Indicator function

$\mathbf{P}_n(\mathbf{c})$ Beam-hit point produced by the nth ORIS element under codeword $\mathbf{c}$

$\mathbf{c}^{\star}_{n,k}$ Selected codeword of the nth ORIS element for user k

$\mathbf{G}$ Codebook-based ORIS gain matrix

$g_{n,k}$ Best channel gain from ORIS element n to user k using the selected codeword

$\hat{\mathbf{N}}(\vartheta, \varphi)$ Unit normal vector of an ORIS mirror for tilt angle ϑ and sweep angle φ

t Ray-tracing parameter for finding the reflected beam-hit point

$d_{\text{out},n,z}$ Vertical component of the reflected direction from the nth ORIS element

r_i Radius of the ith reflected ring on the receiver plane

β_n Angle between the vertical axis and the incident direction at element n

$\mathbf{e}_1, \mathbf{e}_2, \mathbf{e}_3$ Unit vectors along the x-, y- and z-axes

φ_n^{c} Reference sweep angle of the nth ORIS element

$\Delta\vartheta$ Tilt-step design parameter for the non-uniform codebook

$\Delta\varphi$ Sweep-step design parameter for the non-uniform codebook

$\|\Delta\mathbf{H}\|_{\text{F}}$ Frobenius norm of the codebook channel error matrix

$h_{\text{ideal},n}(\mathbf{U}_k)$ Reflected gain of element n under ideal continuous steering

$h_{\text{cb},n}(\mathbf{U}_k)$ Reflected gain of element n under codebook-based steering

$s_{n,k}$ Binary assignment variable of ORIS element n to user k

$\mathbf{S}$ ORIS element assignment matrix

$\tilde{h}_k$ Effective channel gain of user k after ORIS element assignment

p_k NOMA transmit power allocated to user k

σ_w^2 Additive white Gaussian noise variance in the NOMA-VLC system

$J(\mathbf{R})$ Jain fairness index

$\mathbf{R}$ Vector of achievable user rates

$P_{\max}$ Maximum transmit power

C_{p} VLC peak-intensity limit

$\mathscr{U}$ Set of unassigned ORIS elements

$R_j^{(n,k)}$ Rate of user j after the trial assignment of element n to user k

ξ_k Unnormalised GRPA power coefficient of user k

p_k^{GRPA} GRPA power allocated to user k

$\mathbf{x}_i$ Candidate power vector represented by the ith sparrow

$\mathscr{F}$ Feasible set of NOMA power vectors

$\mathbf{p}_{\text{SSA}}^{\star}$ SSA-optimised NOMA power vector

Chapter 1

Introduction

1.1 Motivation

The rapid growth of wireless connectivity is placing increasing pressure on conventional radio frequency (RF) communication systems [1], [2]. As shown in Figure 1.1, the number of global Internet users is projected to increase steadily from 2026 to 2031 [3]. At the same time, the number of connected Internet of Things (IoT) devices is expected to grow rapidly over the same period, as illustrated in Figure 1.2 [4]. This growth is driven by data-intensive and latency-sensitive services, including video streaming, cloud computing, remote working, online education, smart healthcare, industrial automation, intelligent transportation, environmental monitoring, and smart-city infrastructure [5]. Consequently, future wireless networks are expected to support increasingly demanding service requirements, including higher data rates, lower latency, enhanced reliability, improved energy efficiency, accurate localisation, and stronger security [2], [6], [7]. These requirements are central to the vision of sixth generation (6G) networks, in which communication systems are expected to support not only data transmission, but also sensing, intelligence, and adaptation to the surrounding environment [2], [6], [7].

This increasing demand places particular pressure on the RF spectrum, which has enabled modern wireless networks but is becoming increasingly congested and fragmented. The continuous growth in mobile users, connected devices, and data-intensive applications makes it difficult for conventional RF-based systems to satisfy future capacity

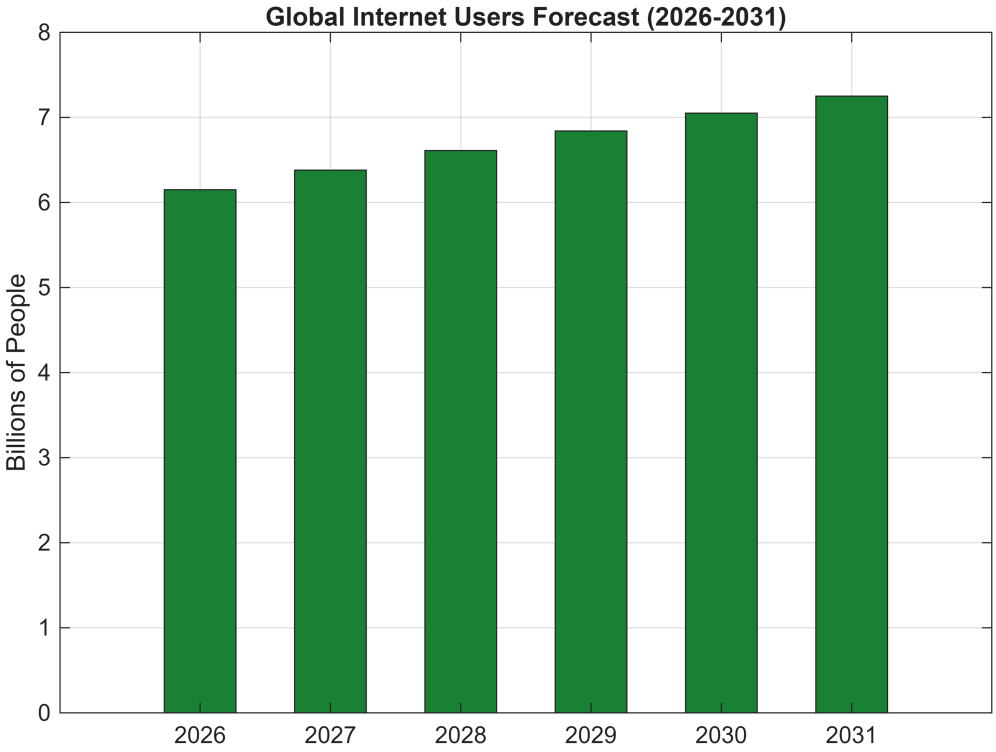


Figure 1.1: Growth of global Internet users from 2026 to 2031 [3].

and reliability requirements using spectrum resources alone [8]. In response, different technologies have been developed for different purposes. Massive multiple-input multiple-output (MIMO) and advanced beamforming can improve spectral efficiency by exploiting spatial multiplexing and directional transmission, whereas millimetre wave (mmWave) and terahertz (THz) communication provide access to wider frequency bands and can therefore increase the available network capacity [1], [9]. However, these technologies also introduce challenges related to hardware complexity, blockage sensitivity, interference management, energy consumption, and regulatory constraints [1], [9]. These limitations motivate the investigation of complementary physical-layer technologies that can support dense indoor communication environments in a secure, energy-efficient, and scalable manner [10], [11].

One promising complementary direction is optical wireless communication (OWC), which uses optical carriers to transmit information wirelessly through free space rather than through guided optical fibres. OWC operates over the optical spectrum, covering ultraviolet, visible, and infrared wavelength bands (approximately from 100 nm to

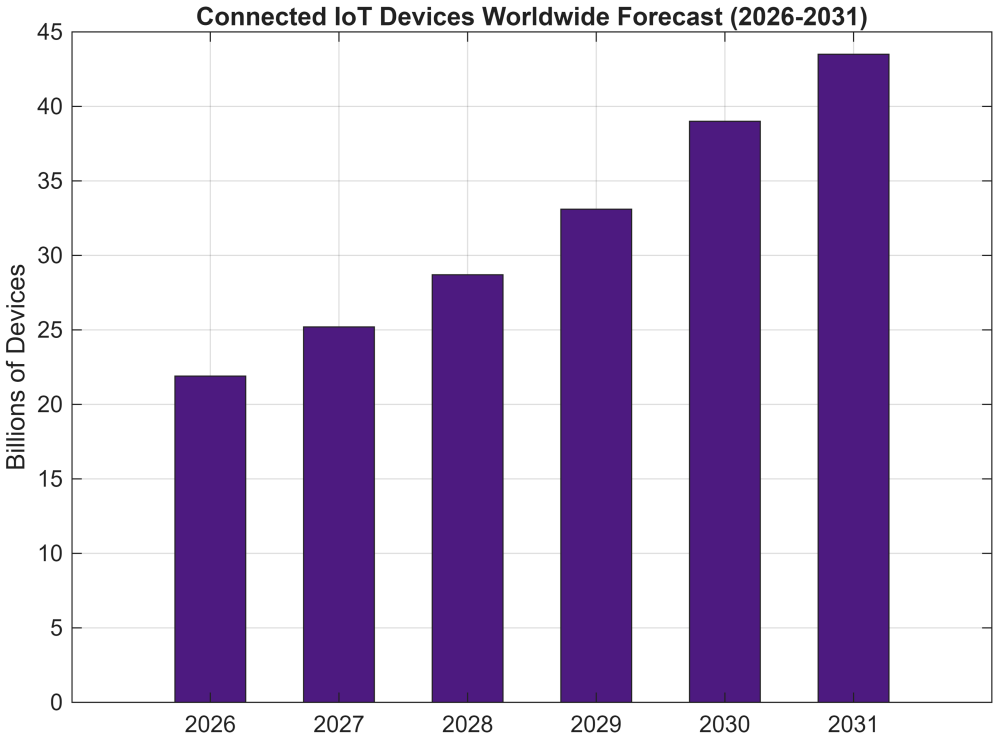


Figure 1.2: Growth of connected IoT devices worldwide from 2026 to 2031 [4].

1 mm), and therefore provides an additional wireless transmission medium beyond conventional RF systems [10], [11]. Optical signals also offer useful physical properties for indoor networks, including low electromagnetic interference, strong spatial confinement, and suitability for short-range communication. These characteristics make OWC attractive for dense indoor environments where RF systems may experience interference, spectrum congestion, or security limitations [10], [11].

Within this broader optical wireless family, different technologies serve different communication and sensing purposes, including free-space optical communication (FSO), optical camera communication (OCC), and visible light communication (VLC). FSO mainly targets high-speed point-to-point links using highly directional optical beams, whereas OCC exploits image sensors for communication and positioning applications [10], [12]. Among these technologies, VLC is particularly relevant to indoor wireless systems because it uses visible light for both illumination and data transmission [13], [14], [15], [16], [17]. In a typical VLC system, information is conveyed by rapidly varying the optical intensity of a light-emitting diode (LED) at a rate that is imperceptible to

the human eye. The received light is then detected by a photodetector and converted into an electrical signal. Since LEDs are already widely deployed for indoor illumination, VLC can reuse existing lighting infrastructure to support wireless communication without requiring additional RF spectrum [13], [15], [16]. This dual use of lighting and communication makes VLC attractive for indoor environments such as offices, hospitals, factories, aircraft cabins, museums, shopping centres, and smart homes, where high-speed local connectivity, accurate positioning, and reliable short-range communication are increasingly required [16], [17].

In addition to this practical reuse of lighting infrastructure, VLC offers several inherent advantages for indoor wireless networks. Visible light signals are naturally confined by walls and opaque objects, which reduces inter-cell interference and limits signal leakage outside the intended physical space [14], [18], [19]. This spatial confinement enables aggressive frequency reuse and provides an additional degree of physical layer security (PLS) compared with conventional RF systems [18], [19]. Furthermore, VLC can support high-resolution positioning and sensing because the received optical power is strongly dependent on distance, incidence angle, irradiance angle, receiver orientation, and the geometry of the indoor environment [14], [20], [21]. Small changes in user position or orientation can therefore produce measurable changes in the received optical signal. This makes VLC suitable not only for communication, but also for localisation, mapping, and sensing. These characteristics align closely with the emerging 6G vision of integrated sensing and communication (ISAC), in which wireless infrastructure is expected to communicate with users while simultaneously perceiving and interacting with the surrounding environment [22].

Despite these advantages, practical VLC systems face several important challenges that limit their reliability in realistic indoor environments. Their performance is strongly affected by line-of-sight (LoS) availability, user orientation, limitations related to the receiver field-of-view (FoV), blockage, shadowing, and channel asymmetry [14], [23], [24], [25]. In realistic indoor environments, users may move, rotate their devices, or

experience partial blockage caused by furniture, walls, or human bodies [26], [27]. These effects can significantly degrade the received optical power and reduce link reliability [24], [25]. Moreover, although the spatial confinement of light can improve security, indoor VLC systems may still be vulnerable to eavesdropping when unintended receivers are located within the illuminated region or close to reflected optical paths [18], [19], [28], [29]. Therefore, intelligent and adaptive techniques are required to control the optical propagation environment, enhance coverage, improve secrecy performance, and support robust communication under practical deployment conditions [19], [27].

To address these challenges, this thesis first considers the use of an optical reconfigurable intelligent surface (ORIS) for controllable optical reflection in indoor VLC systems. By adjusting the orientation of its reflecting elements, an ORIS can redirect, shape, or enhance light propagation towards desired locations [27], [30], [31]. This capability creates opportunities to overcome blockage, improve received signal strength (RSS), extend coverage, and enhance PLS [32], [33], [34]. In this thesis, ORIS-assisted VLC is therefore used in two connected ways: first, to protect indoor communication from eavesdropping through delay-aware optical path control, and second, to improve optical beam control and coverage through geometry-aware codebook design. The security study exploits ORIS-induced time delay and extends the analysis from a single eavesdropper to colluding and non-colluding eavesdroppers [35], [36]. In parallel, the beam-management study develops a non-uniform codebook that adapts the available reflection states to the nonlinear spatial mapping between mirror angles and beam-hit points [37].

While ORIS provides a way to control reflected optical paths, the choice of optical source is also important for localisation and sensing. LEDs are well suited to illumination-based VLC because they provide broad coverage, low cost, and compatibility with existing lighting infrastructure. However, their broad Lambertian emission can limit spatial selectivity when accurate localisation, obstacle detection, or narrow-beam sensing is required [13], [14], [20]. In contrast, vertical-cavity surface-emitting lasers (VCSELs) can

provide narrow beam divergence, high directionality, fast modulation, compact device size, and array-level integration, making them suitable for spatially controlled optical sensing and localisation [38], [39], [40]. These properties motivate the use of VCSELs in this thesis for user localisation, obstacle detection, and environmental sensing.

Moreover, building on the need for narrow-beam optical sensing, this thesis also investigates a light-emitting reconfigurable intelligent surface (LeRIS) architecture for indoor mmWave communication. In this architecture, integrated VCSELs are used to provide user localisation and environmental sensing, while the reconfigurable surface assists adaptive mmWave communication. The sensed environmental information is then used to support blockage-aware LeRIS configuration and route selection for the mmWave communication link [41], [42], [43].

Overall, the challenges discussed above motivate a connected research framework for secure, reliable, and environment-aware indoor wireless communication. The three research directions are connected by a common progression: ORIS-induced time delay is used to protect communication from eavesdropping, non-uniform ORIS codebook design is used to improve optical beam control and coverage, and VCSEL-enabled LeRIS sensing is used to locate users and detect obstacles for adaptive mmWave communication. Together, these directions address security, coverage, and environmental awareness, which are key requirements for robust indoor 6G networks.

The key research objectives of this thesis are as follows:

1. To enhance and analyse the PLS of indoor ORIS-assisted VLC systems by exploiting ORIS-induced time delay under single, colluding, and non-colluding eavesdropping scenarios.
2. To design and evaluate non-uniform codebooks for ORIS-assisted VLC systems by accounting for indoor geometry, nonlinear spatial beam mapping, and non-uniform user distributions.

3. To employ VCSELs for user localisation, obstacle detection, and environmental sensing, and to use this environmental awareness to support adaptive LeRIS-assisted mmWave communication.

1.2 Contributions

This thesis develops intelligent and adaptive OWC, sensing, and hybrid communication techniques for secure and environment-aware indoor 6G networks. The work is organised around the three research objectives introduced in Section 1.1. The first contribution protects indoor VLC communication from eavesdropping using delay-aware ORIS path control. The second contribution improves optical coverage and beam management using geometry-aware non-uniform ORIS codebooks. The third contribution enables user localisation and obstacle-aware communication using VCSEL-enabled LeRIS sensing for adaptive mmWave communication.

The first contribution, presented in Chapter 3, develops a delay-aware security framework for indoor ORIS-assisted VLC. In this framework, ORIS-induced time delay is introduced as an additional physical-layer design dimension. The ORIS is exploited not only to control the received optical power, but also to shape the temporal structure of the received signal. This allows the reflected optical paths to support the legitimate receiver while reducing the useful information that can be recovered by the eavesdropper. The analysis is first developed for a single-eavesdropper case and is then extended to multiple-eavesdropper scenarios, where both colluding and non-colluding eavesdroppers are considered. This provides a more comprehensive security analysis under practical adversarial conditions.

The second contribution, presented in Chapter 4, develops a non-uniform codebook design framework for ORIS-assisted VLC. In practical ORIS deployment, continuous mirror-angle optimisation is difficult, and therefore each reflecting element must select its steering state from a finite codebook. However, a conventional uniform angular

codebook does not necessarily provide uniform spatial coverage on the receiver plane, because the mapping from mirror tilt and sweep angles to the reflected beam-hit point is nonlinear and depends on the position of each ORIS element. To address this limitation, this thesis develops an element-wise non-uniform codebook that adapts the available steering states to the indoor geometry and produces more effective spatial beam mapping. This codebook design is then connected to a multi-user ORIS-assisted VLC system, where the selected reflected beams determine the effective user channels. Based on these channels, non-orthogonal multiple access (NOMA)-based element assignment and power allocation are developed to improve the trade-off between sum-rate and user fairness.

The third contribution, presented in Chapter 5, integrates VCSEL-based optical sensing with LeRIS-assisted mmWave communication. Narrow and spatially controllable VCSEL beams are used to estimate user position and orientation and to detect obstacles in the indoor environment. The obtained sensing information is then used to guide blockage-aware LeRIS configuration and route selection for mmWave communication. In this way, optical sensing provides environmental awareness, while the LeRIS-assisted mmWave link supports adaptive high-capacity communication. This contribution shows how sensing information can be used directly to improve communication reliability in blockage-prone indoor environments.

1.3 Thesis Outline

The remainder of this thesis is organised as follows. Chapter 2 presents the background and fundamental concepts required for the work developed in this thesis. It introduces the principles of OWC and VLC, discusses the characteristics of indoor optical wireless channels, and reviews the roles of ORIS and LeRIS technologies. The chapter also provides the necessary background on PLS, codebook-based beam management, VCSELs-enabled localisation, sensing, and mmWave communication.

Chapter 3 focuses on PLS enhancement in ORIS-assisted VLC systems. In this chapter, ORIS-induced time delay is investigated as a physical-layer mechanism for improving secrecy performance against passive eavesdropping. The analysis is then extended to practical scenarios involving colluding and non-colluding eavesdroppers. This chapter therefore establishes the first technical direction of the thesis, in which delay-aware ORIS element allocation is used to improve the security of indoor VLC networks.

Chapter 4 studies non-uniform codebook design for ORIS-assisted VLC systems. In this chapter, the nonlinear relationship between mirror orientation and the reflected beam-hit point is examined, element-wise non-uniform codebooks are developed for improved spatial mapping, and the resulting codebook is integrated with NOMA-based element assignment and power optimisation.

Chapter 5 investigates the integration of VCSEL-based optical sensing with LeRIS-assisted mmWave communication. In this chapter, VCSELs are used for user localisation, obstacle detection, and environmental sensing, while the LeRIS supports adaptive and blockage-aware mmWave communication. The chapter thereby demonstrates how optical sensing can provide the environmental awareness required to configure resilient LeRIS-assisted links.

Finally, Chapter 6 concludes the thesis by summarising the main findings and contributions. It also discusses the limitations of the proposed approaches and identifies directions for future research in intelligent and adaptive OWC, sensing, and communication for 6G networks.

Chapter 2

Background and Related Work

2.1 Introduction

OWC refers to the transmission of information using optical carriers through unguided free-space propagation, including visible light, infrared, and ultraviolet radiation, rather than through guided optical fibres [10], [44], [45]. The idea of using light for wireless information transfer is not new; one of the earliest demonstrations was the photophone, proposed by Alexander Graham Bell in 1880, in which sound was transmitted over a free-space optical beam by modulating sunlight [46].

During the twentieth century, optical wireless links were mainly investigated in the form of infrared communication and free-space optical transmission [47], [48]. Infrared systems became attractive for short-range indoor links because they provided unlicensed operation, spatial confinement, and low electromagnetic interference [44], [47]. However, early optical wireless systems were limited by the available optical devices, receiver sensitivity, alignment requirements, and the lack of mature solid-state lighting infrastructure. As a result, RF systems became dominant for most wireless applications, while optical wireless technologies remained more specialised.

The development of efficient solid-state light sources, especially LEDs, renewed interest in indoor OWC [13], [15], [49]. Since LEDs can be switched at high speed while still providing illumination, they enabled simultaneous lighting and data transmission. This led to the emergence of VLC, in which the intensity of visible light is modulated to carry

information and a photodetector is used to recover the transmitted signal. Fundamental analysis of LED-based VLC showed that indoor lighting infrastructure could be used for data communication while satisfying illumination requirements [13]. This made VLC attractive for indoor environments, where lighting is already widely deployed, and high-speed local connectivity is increasingly required.

The broader concept of light fidelity (LiFi) builds upon VLC by incorporating bi-directional, multi-user, and networked OWC capabilities [15]. LiFi combines illumination, communication, and networking functions, allowing light sources to act as access points (APs) for indoor wireless connectivity [15]. Compared with conventional RF systems, VLC / LiFi offer several useful properties, including access to a large unlicensed optical spectrum, low electromagnetic interference, high spatial reuse, and inherent confinement by walls and opaque objects [14], [15], [50]. These characteristics make optical wireless technologies suitable for dense indoor scenarios such as offices, hospitals, aircraft cabins, factories, and smart homes.

Despite these advantages, practical VLC / LiFi systems face several limitations. Since optical signals are highly directional and do not penetrate opaque objects, the quality of the link strongly depends on the availability of a reliable LoS path, the receiver FoV, the user position, the device orientation, and the presence of blockers [14], [15], [50]. In addition, the requirement of intensity modulation/direct detection (IM/DD) imposes specific constraints on the transmitted waveform, since the optical intensity must be real and non-negative [45], [51]. These characteristics make the design of optical wireless systems different from conventional RF systems and require dedicated channel models, modulation schemes, receiver designs, and resource allocation methods.

More recently, OWC has been considered an important complementary technology for beyond-fifth generation (5G) and 6G networks [6], [10], [11]. The 6G vision is expected to integrate communication, localisation, sensing, security, and intelligence within the same wireless infrastructure [2], [7], [22]. In this context, OWC is attractive not only because it provides additional spectrum, but also because optical signals can offer high

spatial resolution and strong geometric dependence, which are useful for positioning and environmental awareness [14], [20], [21]. Therefore, modern optical wireless systems are no longer limited to data transmission, but are increasingly being studied for integrated communication, localisation, mapping, and sensing.

At the same time, controllable wireless environments have gained significant attention for future wireless systems. In indoor VLC systems, an ORIS redirects optical beams towards desired locations by adjusting the orientation of its reflecting elements [27], [30], [31]. More broadly, the integration of reconfigurable surfaces with LiFi has been identified as a promising direction for future 6G networks, particularly for mitigating LoS blockage, improving link reliability, and creating controllable optical propagation environments [52]. From a modelling perspective, an ORIS operates mainly according to geometric optics (GO), where optical propagation is represented by rays following the laws of reflection. Within this framework, each reflecting element acts as a controllable optical mirror that adjusts the direction of the incident beam, making the reflected beam strongly dependent on the room geometry, transmitter position, receiver location, and mirror orientation. In addition to optical beam control, the hybrid optical-mmWave system considered in this thesis uses the large available mmWave bandwidth to support high-capacity wireless communication. However, limited diffraction makes mmWave signals particularly susceptible to blockage, while propagation losses further constrain link reliability. To address these challenges, a LeRIS combines optical localisation and sensing with programmable mmWave reflection to support environment-aware communication.

In parallel, different optical sources provide complementary capabilities for optical wireless systems. LEDs are well suited to broad-area illumination and VLC coverage, whereas VCSELs provide narrower beams, high directionality, fast modulation, and compact integration [13], [38], [39], [40]. However, VCSELs also introduce practical challenges, including higher fabrication cost, increased system complexity, and eye-safety considerations due to their narrow and high-intensity optical emission [53]. The latter

characteristics are useful for spatially selective communication, localisation, mapping, and sensing [38], [40], [43]. When integrated into LeRIS, VCSELs can provide spatial awareness that helps configure communication links, especially in blockage-sensitive mmWave systems [41], [42], [54].

The connection between these technologies is illustrated in Figure 2.1. The figure summarises how the background topics discussed in this chapter support the three main directions of the thesis: ORIS-assisted PLS, non-uniform ORIS codebook design, and VCSEL-enabled LeRIS communication.

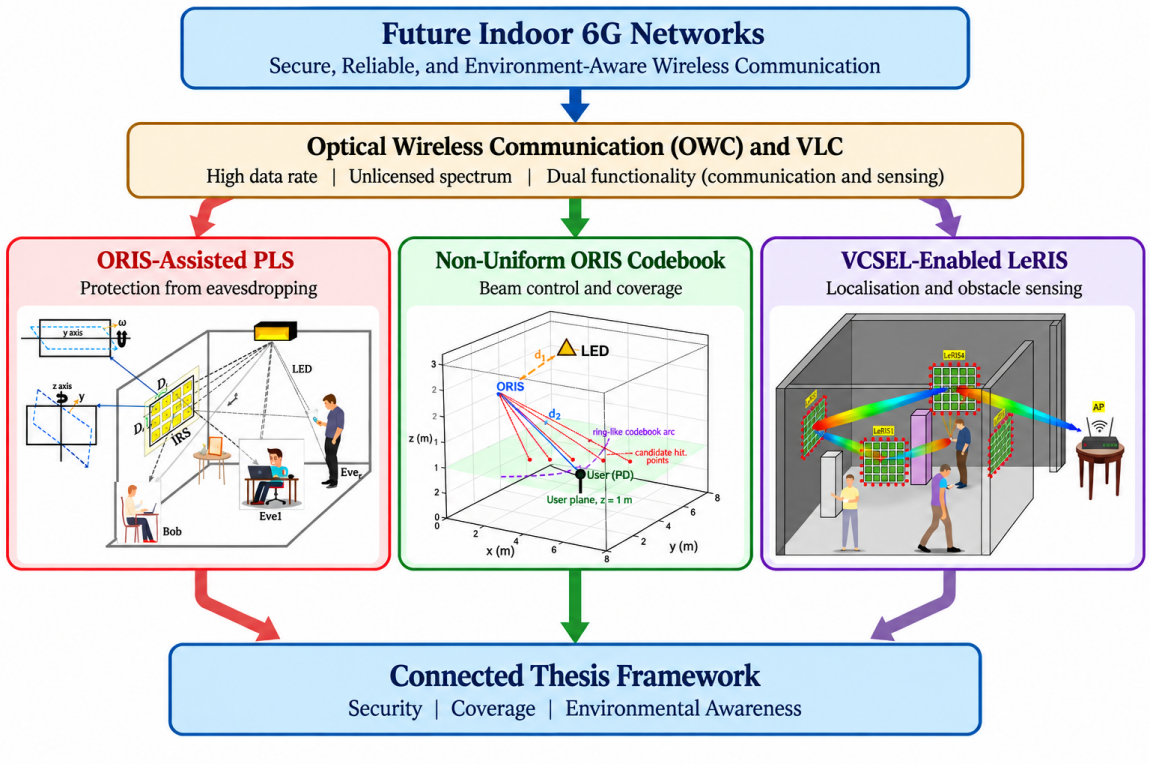


Figure 2.1: Overall concept of the proposed indoor OWC and sensing framework.

Therefore, OWC has developed into several complementary branches, including FSO, infrared links, VLC, and LiFi, each addressing different communication scenarios and application requirements. In this thesis, intelligent and adaptive optical wireless systems are investigated through VLC, ORIS-assisted optical beam management, and LeRIS-enabled sensing and communication to support secure, adaptive, and environment-aware wireless networks for future 6G systems.

2.2 Optical Wireless System Structure

2.2.1 Basic Structure

A typical indoor optical wireless system consists of an optical transmitter, an optical wireless channel, and an optical receiver [45], [51]. Depending on the application, the transmitter may be an LED luminaire for illumination-based VLC or a directional source such as a VCSEL for narrow-beam communication, localisation, or sensing. In each case, the information signal is imposed on the instantaneous optical intensity of the light source, while the receiver, commonly a photodiode (PD) or avalanche photodiode (APD), converts the received optical power into an electrical signal. This transmission principle is usually referred to as IM/DD, in which optical intensity is modulated at the transmitter and direct detection is performed at the receiver [38], [45], [51].

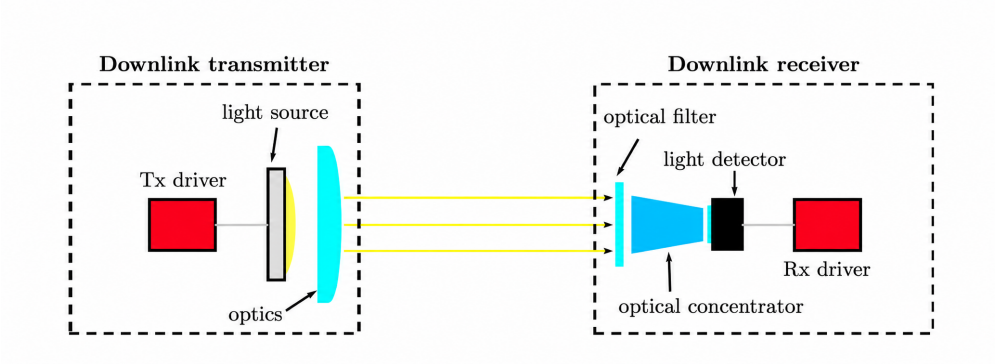


Figure 2.2: Basic indoor OWC system based on IM/DD.

As illustrated in Figure 2.2, the input data are converted into an electrical driving signal, which modulates the optical intensity of the transmitter. The emitted optical signal then propagates through the indoor optical wireless channel before being detected by the receiver. The received signal is finally decoded to recover the transmitted data. The transmitted optical signal may reach the receiver through a direct LoS path or through reflected non-line-of-sight (NLoS) components from walls, ceilings, floors, or other indoor objects [23], [44], [48]. In many indoor OWC systems, the LoS component

is dominant because optical propagation is highly directional and optical signals do not penetrate opaque objects. The RSS therefore depends strongly on the transmitter position, receiver location, incidence angle, irradiance angle, receiver FoV, and the presence of blockers [13], [23], [25].

In an IM/DD-based optical wireless link, the optical channel is commonly described by its channel impulse response. When both direct and reflected propagation components are considered, the overall channel impulse response can be written as

$$h(t) = h_{\mathrm{LoS}}(t) + h_{\mathrm{NLoS}}(t) \tag{2.1}$$

where $h_{\mathrm{LoS}}(t)$ and $h_{\mathrm{NLoS}}(t)$ represent the LoS and reflected NLoS components, respectively. Therefore, a general baseband received electrical signal can be expressed as

$$y(t) = R_{\mathrm{PD}}\left[x(t) * h(t)\right] + n(t) \tag{2.2}$$

where $x(t)$ is the transmitted optical intensity signal, $*$ denotes convolution, R_{PD} is the photodetector responsivity, and $n(t)$ denotes the receiver noise. Since information is carried by optical intensity, the transmitted signal must satisfy the non-negativity constraint

$$x(t) \geq 0. \tag{2.3}$$

This constraint is one of the main differences between optical wireless and conventional RF communication, in which the transmitted waveform can usually take positive and negative values around zero [51], [55].

For narrowband or direct current (DC) channel-gain analysis, the time-domain channel response can be represented by an equivalent scalar channel gain h. In this simplified case, the received optical power is written as

$$P_{\mathrm{r}} = hP_{\mathrm{t}}, \tag{2.4}$$

where P_t is the transmitted optical power and P_r is the received optical power. The corresponding electrical signal-to-noise ratio (SNR) can then be expressed as

$$\gamma = \frac{(R_{PD}P_r)^2}{\sigma^2} = \frac{(R_{PD}hP_t)^2}{\sigma^2}, \tag{2.5}$$

where σ^2 is the receiver noise variance, including the noise contributions discussed in Section 2.2.5.

2.2.2 Optical Transmitters

The optical transmitter is a central component of an optical wireless system, and its characteristics are selected according to the intended application. In conventional indoor VLC systems, LEDs are widely used because they are energy efficient, low cost, long-lasting, and already deployed for indoor illumination [13], [14], [15]. By rapidly varying the driving current of an LED, the emitted optical intensity can be modulated at a speed that is not perceptible to the human eye, thereby enabling simultaneous illumination and data transmission [13], [15].

The radiation pattern of an LED is commonly modelled using a Lambertian emission profile [13], [23]. In this model, the emitted optical intensity decreases as the irradiance angle increases from the transmitter boresight. The Lambertian emission order is given by

$$m = \frac{-\ln(2)}{\ln(\cos(\Phi_{1/2}))},$$

where $\Phi_{1/2}$ is the semi-angle at half optical power. A smaller value of $\Phi_{1/2}$ corresponds to a narrower beam and a larger Lambertian order, while a larger value of $\Phi_{1/2}$ corresponds to a wider illumination pattern. This model is widely used in indoor VLC analysis because it provides a simple description of the broad-area emission produced by LEDs [13], [23].

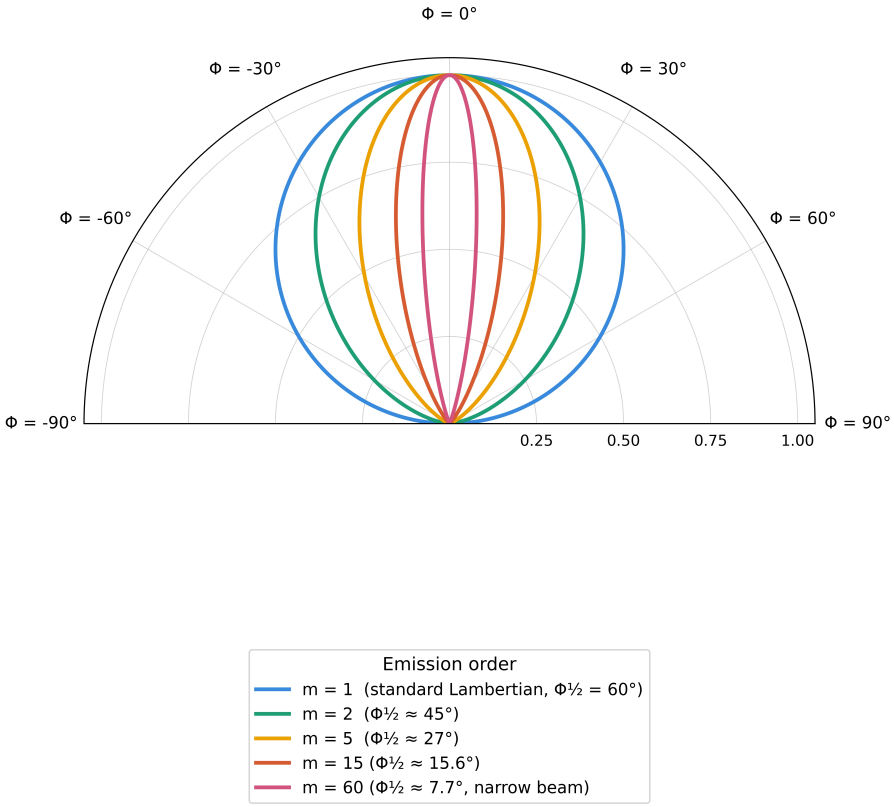


Figure 2.3: Lambertian radiation profiles for different emission orders.

Figure 2.3 illustrates Lambertian radiation profiles for different emission orders. As the Lambertian order increases, the emitted optical power becomes more concentrated around the transmitter boresight, resulting in a narrower optical beam. This relationship highlights the trade-off between wide-area illumination and directional optical transmission.

In addition to LEDs, semiconductor lasers provide an alternative optical transmitter technology with higher directionality and faster modulation capability. Among different semiconductor laser technologies, VCSELs have attracted increasing attention for optical wireless systems because they provide narrow beam divergence, high modulation bandwidth, compact integration, and low power consumption [38], [39], [40]. These characteristics make VCSELs suitable for applications requiring spatially selective transmission, localisation, mapping, and sensing.

Unlike broad-area LED emission, the optical output of a VCSEL is characterised by a highly directional Gaussian-like beam profile, where the optical intensity is concentrated around the optical axis and gradually decreases away from the beam centre [38], [39]. The Gaussian beam radius at propagation distance d can be expressed as

$$w(d) = w_0 \sqrt{1 + \left(\frac{d}{z_R}\right)^2},$$

where w_0 is the beam waist and z_R is the Rayleigh range. The corresponding Gaussian intensity distribution can be written as

$$I(r,d) = I_0 \left(\frac{w_0}{w(d)}\right)^2 \exp\left(-\frac{2r^2}{w^2(d)}\right),$$

where r represents the radial distance from the beam centre and I_0 is the peak optical intensity.

The divergence angle determines the far-field angular spread of the emitted optical power. For illustration, the normalised far-field angular intensity profile of a VCSEL beam can be represented as

$$\frac{I(\phi)}{I_0} = \exp\left(-2\left(\frac{\phi}{\phi_0}\right)^2\right),$$

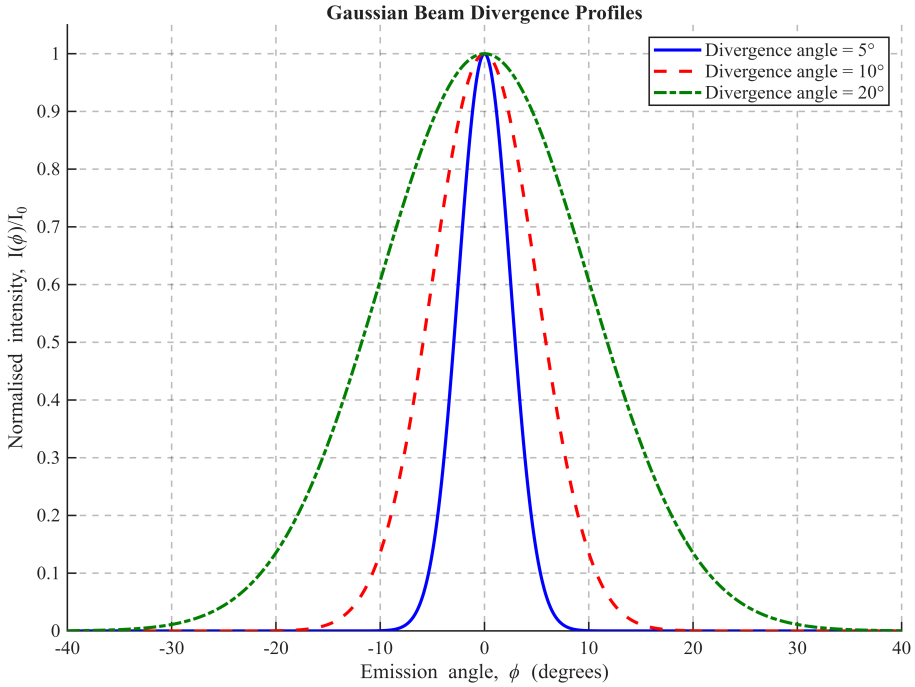


Figure 2.4: Normalised far-field Gaussian-like intensity profiles of VCSEL beams with different divergence angles.

where ϕ represents the angular deviation from the optical axis and ϕ_0 denotes the divergence parameter. A smaller divergence angle corresponds to a more concentrated beam around the optical axis, whereas a larger divergence angle produces a wider emission profile. Figure 2.4 illustrates the normalised far-field Gaussian-like intensity distribution of VCSEL beams for different divergence angles. Compared with LEDs, the directional Gaussian beam characteristics of VCSELs enable improved spatial selectivity, which is beneficial for integrated communication, localisation, and sensing applications [38], [40].

2.2.3 Optical Receivers

The optical receiver converts the incident optical power into an electrical current [56], [57]. In most VLC systems, this operation is performed using a PD [13], [51]. The generated photocurrent is proportional to the received optical power and the photodetector responsivity, as expressed by

$$i_{\mathrm{p}}(t) = R_{\mathrm{PD}} P_{\mathrm{r}}(t), \tag{2.6}$$

where $i_{\mathrm{p}}(t)$ is the photocurrent and $P_{\mathrm{r}}(t)$ is the received optical power. The responsivity R_{PD} depends on the photodetector material and the optical wavelength.

The receiver performance is affected by several physical parameters, including the active detection area A_{PD}, the receiver FoV, the optical filter gain $T_{\mathrm{s}}(\psi)$, and the optical concentrator gain $g(\psi)$ [13], [45], [51]. A larger photodetector area can collect more optical power, but it may also increase capacitance and reduce receiver bandwidth [56], [58]. Similarly, a wider FoV can improve coverage and reduce link blockage, but it may also increase the amount of collected background light and reflected interference [14], [23], [25]. Therefore, receiver design involves a trade-off between coverage, bandwidth, noise, and sensitivity.

In a typical indoor VLC system, the transmitted optical signal propagates through the optical wireless channel and is collected by the receiver front-end. The receiver front-end generally consists of optical components, including an optical concentrator, optical filter, and photodetector, as illustrated in Figure 2.5.

The optical concentrator improves the received optical power by collecting incident signals within the receiver acceptance angle. Its gain is commonly written as [13], [51]

$$g(\psi) = \begin{cases} \dfrac{n_{\mathrm{r}}^2}{\sin^2(\Psi_{\mathrm{c}})}, & 0 \le \psi \le \Psi_{\mathrm{c}}, \\ 0, & \psi > \Psi_{\mathrm{c}}, \end{cases} \tag{2.7}$$

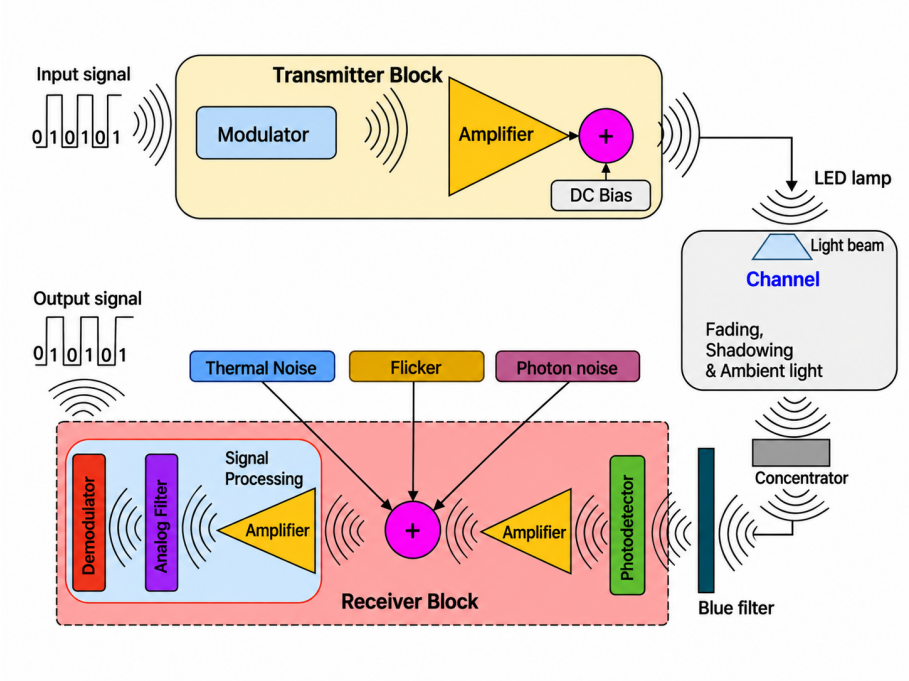


Figure 2.5: Illustration of a typical indoor VLC system consisting of an optical transmitter, optical channel, receiver concentrator, and photodetector.

where n_r is the refractive index of the concentrator, ψ is the incidence angle, and Ψ_c is the receiver FoV. This expression shows that the receiver only collects optical signals that arrive within its angular acceptance range. As a result, user orientation and device rotation can significantly affect the received signal quality in practical indoor optical wireless systems [24], [25].

2.2.4 Optical Channel Model

The indoor optical wireless channel is strongly determined by geometry [23], [45], [48]. Unlike RF propagation, visible light does not penetrate opaque objects, and the received optical power depends mainly on the relative position and orientation of the transmitter and receiver [14], [23]. Following the system-level representation in Section 2.2.1, this subsection focuses on the DC channel-gain models used to describe indoor OWC/VLC links.

In general, an optical wireless channel can be represented by its time-domain impulse response $h(t)$, which characterises the temporal response of the propagation environment. The corresponding frequency-domain channel response is obtained as $H(f) = \mathscr{F}\{h(t)\}$. For conventional indoor VLC link-budget analysis, where the main objective is to evaluate the received optical power, the channel is often simplified using the DC channel gain, represented by $H(0)$. However, when different propagation paths introduce significant delay differences, the frequency-selective characteristics described by $H(f)$ become important and are considered in the delay-aware ORIS-assisted studies presented later in this thesis.

The received signal may contain a direct LoS component and reflected NLoS components produced by walls, ceilings, floors, and indoor objects [23], [48]. The LoS component is usually dominant, while reflected components may provide additional received power but can also introduce delay spread and inter-symbol interference (ISI) [23].

For a Lambertian LED transmitter, the DC LoS channel gain can be derived from the Lambertian emission model and is commonly expressed as [13], [44], [45], [51].

$$H_{\mathrm{LoS}}(0) = \begin{cases} \dfrac{(m+1)A_{\mathrm{PD}}}{2\pi d^2}\cos^m(\phi)T_{\mathrm{s}}(\psi)g(\psi)\cos(\psi), & 0 \le \psi \le \Psi_{\mathrm{c}}, \\ 0, & \psi > \Psi_{\mathrm{c}}, \end{cases} \tag{2.8}$$

where the Lambertian order m, distance d, irradiance angle ϕ, incidence angle ψ, optical filter gain $T_{\mathrm{s}}(\psi)$, concentrator gain $g(\psi)$, receiver area A_{PD}, and receiver FoV Ψ_{c} follow the transmitter and receiver definitions given in Sections 2.2.2 and 2.2.3. This expression is specific to Lambertian optical sources, where the emitted power follows a cosine-based radiation pattern. For other optical transmitters with different beam profiles, such as VCSEL-based systems, alternative channel models are required.

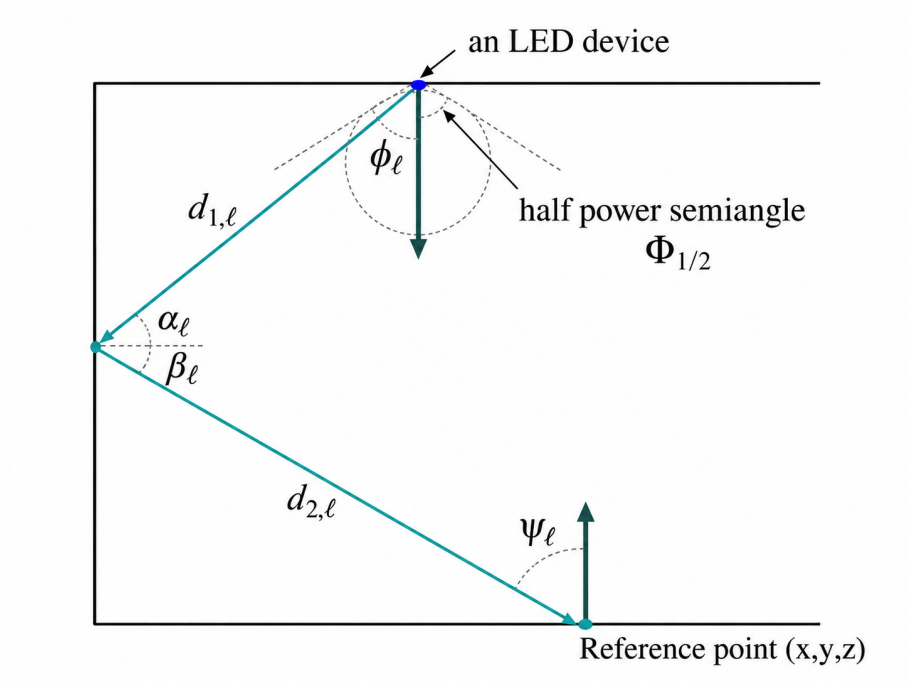


Figure 2.6: Propagation model of diffuse link.

The NLoS channel gain is usually obtained by considering first-order or higher-order reflections from indoor surfaces. For a first-order diffuse reflection from the ℓth reflecting surface element, the DC NLoS channel gain can be written as [13], [44], [45], [51]

$$H_{\mathrm{NLoS},\ell}(0) = \begin{cases} \dfrac{(m+1)A_{\mathrm{PD}}A_\ell\rho_\ell}{2\pi^2 d_{1,\ell}^2 d_{2,\ell}^2}\cos^m(\phi_\ell)\cos(\alpha_\ell)\cos(\beta_\ell)T_{\mathrm{s}}(\psi_\ell)g(\psi_\ell)\cos(\psi_\ell), & 0 \le \psi_\ell \le \Psi_{\mathrm{c}}, \\ 0, & \psi_\ell > \Psi_{\mathrm{c}}, \end{cases} \tag{2.9}$$

The geometry of a first-order reflected optical path is illustrated in Figure 2.6. The propagation distances and angular parameters shown in the figure correspond to the terms used in the NLoS channel gain expression in (2.9).

where A_ℓ and ρ_ℓ are the area and reflection coefficient of the reflecting element, while $d_{1,\ell}$ and $d_{2,\ell}$ are the transmitter–surface and surface–receiver distances, respectively. The remaining angular and receiver terms follow the same definitions used in the LoS channel model. The aggregate reflected channel is obtained by summing the contributions of the considered reflected paths.

Moreover, while the Lambertian model is commonly used for broad-area LED emission, VCSEL-based systems are typically described by narrower and more directional Gaussian beams [38], [39], [40]. A Gaussian beam approximation can be used to describe this behaviour [38], [40]. The beam radius at distance d can be written as

$$w(d) = w_0 \sqrt{1 + \left(\frac{d}{z_{\mathrm{R}}}\right)^2}, \tag{2.10}$$

where w_0 is the beam waist and z_{R} is the Rayleigh range. As illustrated in Figure 2.7, the Gaussian beam has its minimum radius at the beam waist and gradually expands as the propagation distance increases. The Rayleigh range is given by

$$z_{\mathrm{R}} = \frac{\pi w_0^2}{\lambda}, \tag{2.11}$$

where λ is the optical wavelength.

The optical intensity of a Gaussian beam decreases with the radial distance from the beam centre. A simplified Gaussian intensity distribution can be expressed as

$$I(r,d) = I_0 \left(\frac{w_0}{w(d)}\right)^2 \exp\left(-\frac{2r^2}{w^2(d)}\right), \tag{2.12}$$

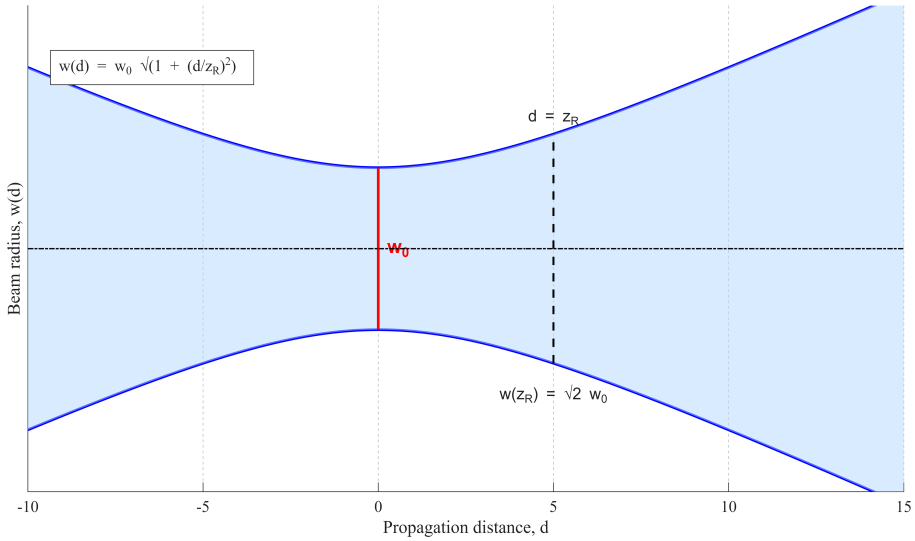


Figure 2.7: Illustration of Gaussian beam radius variation with propagation distance, showing the beam waist w_0 and Rayleigh range z_{R}.

where I_0 is the peak intensity at the beam waist and r is the radial displacement from the beam axis. This model is useful for VCSEL-based localisation and sensing, because small changes in user position or orientation can produce measurable changes in received optical power [38], [40].

The receiver FoV and user orientation also affect the optical channel [13], [24], [25]. If the incidence angle is larger than the receiver acceptance angle, the corresponding optical path is not detected. Therefore, even when a geometric path exists between the transmitter and receiver, the link may fail if the signal arrives outside the receiver angular range [24], [25].

2.2.5 Noise Modelling in Optical Wireless Systems

Noise is an important impairment in indoor OWC and VLC systems because it directly affects the received electrical signal and the achievable SNR. The main receiver-noise components are shot noise and thermal noise [45], [51], [59]. Shot noise is associated with the discrete nature of photodetection and is influenced by the received optical power and background light. Its variance can be expressed as

$$\sigma_{\text{shot}}^2 = 2qR_{\text{PD}}\left(P_{\text{r}} + P_{\text{bg}}\right)B, \tag{2.13}$$

where q is the electron charge, P_{bg} is the received background optical power, and B is the system bandwidth. Thermal noise is generated by the receiver electronics and can be represented in simplified form as

$$\sigma_{\text{thermal}}^2 = \frac{4k_{\text{B}}T_{\text{k}}B}{R_{\text{L}}}, \tag{2.14}$$

where k_{B} is Boltzmann's constant, T_{k} is the absolute temperature, and R_{L} is the receiver load resistance. The total receiver-noise variance is therefore

$$\sigma^2 = \sigma_{\text{shot}}^2 + \sigma_{\text{thermal}}^2. \tag{2.15}$$

2.2.6 Achievable Data Rate

The total noise variance in (2.15) is used in the electrical SNR expression defined previously in (2.5). Therefore, the achievable communication rate is directly related to the received optical power, channel gain, and receiver-noise level through the resulting SNR. For communication analysis, the achievable data rate can be written in a Shannon-like form as [45], [51]

$$R = B\log_2(1+\gamma), \tag{2.16}$$

where R is the achievable data rate, B is the system bandwidth, and γ is the electrical SNR defined in (2.5). In multi-user or interference-limited systems, the signal-to-interference-plus-noise ratio (SINR) may be used instead of the SNR [59], [60]. The exact rate expression may vary depending on the signalling constraint, receiver model, and modulation format.

2.2.7 Blockage and Mobility

Blockage and mobility are major practical challenges in indoor optical wireless systems [14], [24], [25]. Since visible light does not pass through opaque objects, human bodies, furniture, walls, and other obstacles can interrupt the direct LoS path [14], [23]. As the user moves, the link geometry and receiver orientation may also change continuously [24], [25]. These effects motivate the use of intelligent and controllable propagation techniques, such as an ORIS for redirecting optical beams and VCSEL-based sensing for providing spatial information about users and obstacles [27], [31], [38].

2.3 ORIS and LeRIS

2.3.1 Basic Concept

This thesis considers two specific technologies for creating controllable indoor wireless environments: ORIS technology for optical links and LeRIS technology for hybrid optical sensing and mmWave communication. Both technologies support the broader concept of a programmable wireless environment (PWE), in which dedicated panels become controllable parts of the communication system rather than passive elements of the room [2], [6], [61].

An ORIS controls the optical propagation path by changing the orientation of its reflecting elements. This allows incident light to be redirected towards desired receiver locations, which can improve coverage, create an alternative path when the direct LoS link is weak or blocked, and support secure optical transmission [27], [30], [31]. Because the reflected beam follows GO, the performance of an ORIS depends directly on the transmitter position, mirror orientation, receiver position, and receiver FoV.

A LeRIS serves a different role in this thesis. It combines programmable mmWave reflecting elements with integrated optical sources, particularly VCSELs, for user localisation and environmental sensing [43], [62]. The optical measurements provide information about user positions and obstacles, while the LeRIS uses this information to configure blockage-resilient mmWave communication paths. Therefore, ORIS is used for the VLC contributions, whereas LeRIS panels are used for the integrated localisation, mapping, and communication contribution.

2.3.2 ORIS

An ORIS consists of controllable reflecting elements that redirect incident optical signals towards desired receiver locations [27], [31]. In VLC, an ORIS can be placed on indoor surfaces such as walls or ceilings to create additional reflected paths between an optical transmitter and a receiver [27], [30], [31]. These reflected paths can improve the received optical power, reduce coverage holes, and support communication when the direct LoS link is weak or blocked [27], [31].

As shown in Figure 2.8, the reflected optical path is determined by the transmitter position, reflecting-element orientation, and receiver location. Unlike diffuse reflection, where light is scattered in many directions, an ORIS mainly relies on controlled specular reflection [27], [31], [37]. In this case, the direction of the reflected beam depends on the incident direction and on the orientation of the reflecting element.

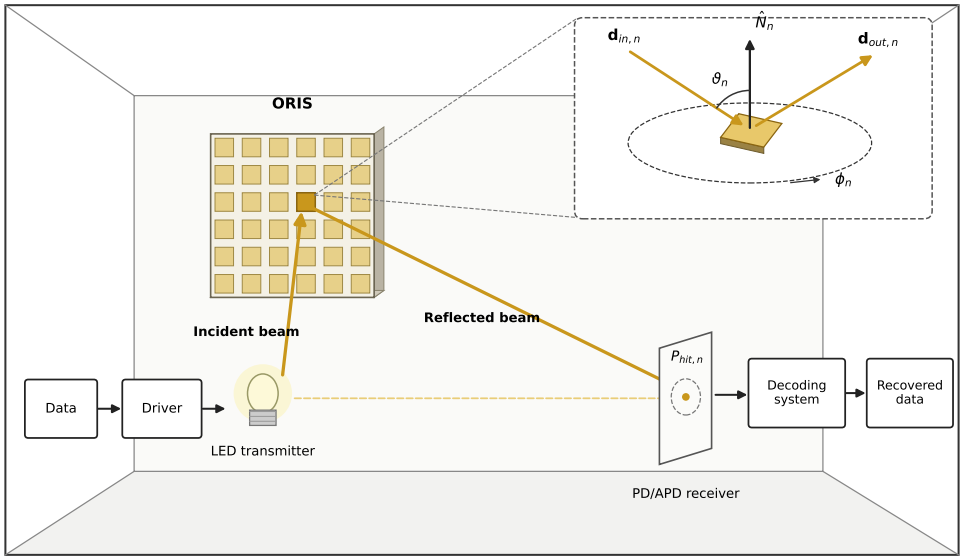


Figure 2.8: ORIS-assisted VLC system with controllable specular reflection.

For the nth reflecting element, the incident direction can be represented by the unit vector $\mathbf{d}_{\text{in},n}$, while the reflected direction can be represented by $\mathbf{d}_{\text{out},n}$. If $\hat{\mathbf{N}}_n$ denotes the unit normal vector of the reflecting element, the reflected direction can be written using the law of reflection as [27], [31], [37]

$$\mathbf{d}_{\text{out},n} = \mathbf{d}_{\text{in},n} - 2\left(\mathbf{d}_{\text{in},n}^T \hat{\mathbf{N}}_n\right)\hat{\mathbf{N}}_n. \tag{2.17}$$

This expression shows that the reflected beam is controlled by the normal vector of the reflecting element. In a practical ORIS, this normal vector can be adjusted through mechanical or micro-electromechanical control of the mirror orientation [31], [37].

For ORIS-assisted VLC, the reflected link is modelled as a controllable specular path through each reflecting element. For the nth ORIS element, the DC reflected channel gain can be written as

$$H_{\text{ORIS},n}(0) = \begin{cases} \dfrac{\rho_n (m+1) A_n}{2\pi (d_{t,n} + d_{r,n})^2} \cos^m(\phi_{t,n}) \cos(\psi_{s,n}) T_s(\psi_{r,n}) g(\psi_{r,n}) \cos(\psi_{r,n}), & 0 \le \psi_{r,n} \le \Psi_c, \\ 0, & \psi_{r,n} > \Psi_c, \end{cases} \tag{2.18}$$

where ρ_n is the reflection coefficient of the nth ORIS element, A_n is the area of the reflecting element, $d_{t,n}$ is the distance from the transmitter to the nth ORIS element, and $d_{r,n}$ is the distance from the nth ORIS element to the receiver. The angle $\phi_{t,n}$ is the irradiance angle from the transmitter to the ORIS element, $\psi_{s,n}$ is the incidence angle on the reflecting surface, and $\psi_{r,n}$ is the incidence angle of the reflected beam at the receiver. The reflected contribution is zero when the reflected beam arrives outside the receiver FoV.

Moreover, the orientation of an optical reflecting element is often described using two angles, namely the tilt angle and the sweep angle. In this thesis, the tilt angle of the nth reflecting element is denoted by ϑ_n, while the sweep angle is denoted by φ_n. These angles determine the normal vector $\hat{\mathbf{N}}_n$, and therefore determine the outgoing direction $\mathbf{d}_{\text{out},n}$. The point where the reflected beam reaches the receiver plane is denoted by $\mathbf{P}_{\text{hit},n}$.

The sensitivity of the reflected hit point to a small change in mirror orientation can be quantified from this geometric mapping. For an ORIS element located at $\mathbf{r}_n$, the intersection of the reflected ray with a receiver plane at height z_{u} can be written as

$$\mathbf{P}_{\text{hit},n} = \mathbf{r}_n + \frac{z_{\text{u}} - z_n}{[\mathbf{d}_{\text{out},n}]_z}\mathbf{d}_{\text{out},n}. \tag{2.19}$$

Therefore, for small changes $\Delta\vartheta_n$ and $\Delta\varphi_n$, the corresponding displacement of the reflected hit point can be approximated by

$$\Delta\mathbf{P}_{\text{hit},n} \approx \mathbf{J}_n \begin{bmatrix} \Delta\vartheta_n \\ \Delta\varphi_n \end{bmatrix}, \qquad \mathbf{J}_n = \frac{\partial \mathbf{P}_{\text{hit},n}}{\partial(\vartheta_n, \varphi_n)}, \tag{2.20}$$

where $\mathbf{J}_n$ represents the local angular-to-spatial sensitivity. Hence, the same angular change can produce substantially different spatial displacements depending on the ORIS element position and link geometry. This geometry-dependent behaviour motivates the non-uniform codebook design developed and evaluated in Chapter 4.

The received optical power through an ORIS-assisted path depends on the transmitter power, reflection coefficient, path distances, receiver FoV, and alignment between the reflected beam and the receiver. Therefore, ORIS design is not only a question of increasing reflected power, but also of ensuring that the reflected beam reaches the intended location with a suitable angle and sufficient optical intensity.

2.3.3 LeRIS

A LeRIS combines optical sensing with programmable mmWave reflection. In this thesis, the optical part provides user-localisation and obstacle-awareness information, while the reconfigurable surface uses that information to support adaptive mmWave communication [43], [54], [62]. This role is different from an ORIS-assisted VLC system, where the reflecting surface redirects optical communication beams.

The reflecting elements in the two architectures therefore serve different physical functions. In the ORIS considered in this thesis, the elements are controllable optical mirrors that redirect incident VLC beams by changing their orientation. In contrast, the reflecting elements of a LeRIS are programmable mmWave reflecting elements that control the propagation of the RF/mmWave signal, while the optical sources integrated around the surface are used separately for localisation and sensing. Thus, the ORIS performs optical reflection, whereas the LeRIS combines optical sensing with programmable mmWave reflection.

The optical source used in a LeRIS architecture can be selected according to the sensing requirement. LEDs are suitable for broad coverage, whereas VCSELs are more suitable for spatially selective measurements because of their narrow and directional beams [38], [39], [40]. Chapter 5 considers the VCSEL-based LeRIS configuration, in which optical sensing provides user and obstacle awareness for adaptive LeRIS-assisted mmWave communication.

The functional architecture is illustrated in Figure 2.9, where the LeRIS panels provide optical localisation and obstacle-awareness information that is used to support adaptive route selection for the mmWave communication link.

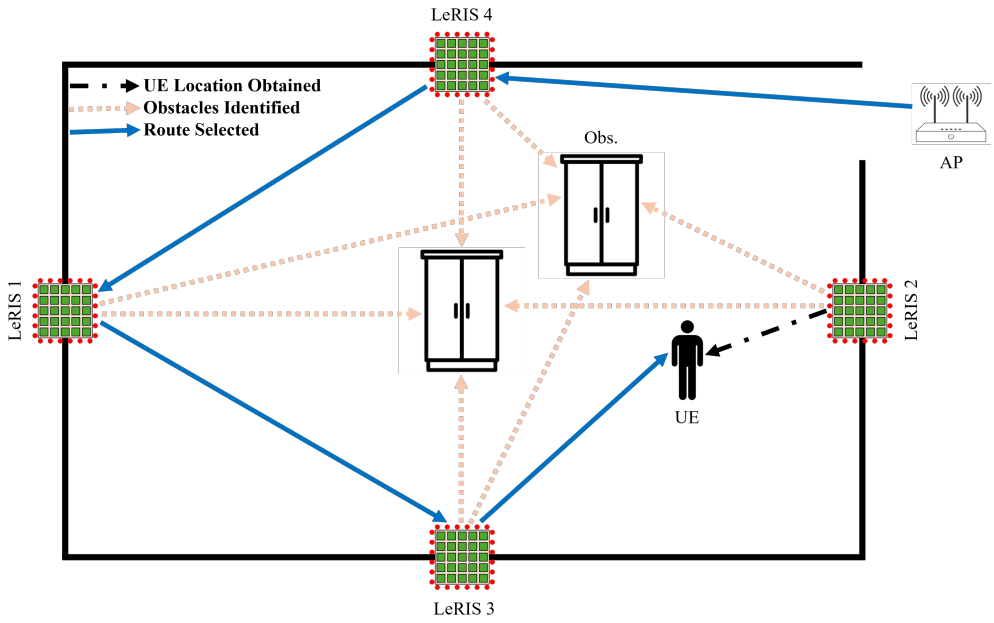


Figure 2.9: Indoor PWE with VCSEL-based LeRIS panels for localisation, obstacle mapping, and mmWave communication.

2.3.4 Practical Design Considerations

Although ORIS and LeRIS both create controllable indoor wireless environments, their practical design requirements are different. In an ORIS-assisted VLC system, optical reflection is governed by room geometry, mirror orientation, and the nonlinear relationship between the selected angles and the resulting beam-hit point [27], [31], [37]. Ideal continuous-angle steering is useful as an analytical reference, but a practical controller requires a finite set of implementable mirror states. These states are commonly organised as a codebook, and their spatial distribution is important because uniformly spaced angular states do not necessarily provide uniform coverage on the receiver plane [37], [63], [64].

For a LeRIS-assisted mmWave system, the principal design considerations are accurate user localisation, obstacle awareness, and reliable route configuration [41], [42]. Since a selected direct or reflected mmWave path may be blocked, the LeRIS controller requires current spatial information before configuring a suitable single-hop or multi-hop route. The VCSEL-based sensing architecture considered in this thesis provides this information through optical localisation and mapping.

These distinct considerations show that ORIS and LeRIS should be analysed according to their physical functions rather than through a single generic surface model. Accordingly, the following sections first review the security concepts required for Chapter 3, then introduce codebook design and multiple access for Chapter 4, and finally discuss optical localisation, sensing, and environment-aware communication for Chapter 5.

2.4 Physical Layer Security

2.4.1 Security in VLC

PLS uses the physical characteristics of a communication channel to protect confidential information from unauthorised receivers [65], [66]. Unlike conventional cryptographic methods, which operate mainly at higher network layers, PLS exploits differences between the legitimate and eavesdropping channels. A positive secrecy rate is achieved when the legitimate receiver can obtain a higher achievable rate than the eavesdropper.

Indoor VLC offers several natural security advantages. Visible light is confined by walls and opaque objects, and the directionality of optical beams and the limited receiver FoV restrict the region in which a signal can be detected [18], [19]. Nevertheless, an eavesdropper located inside the illuminated area may still intercept the direct or reflected optical signal. This risk is particularly relevant in shared indoor environments, such as offices, hospitals, shopping centres, and aircraft cabins [18], [19], [32]. Therefore, the spatial confinement of light should be complemented by dedicated PLS mechanisms.

2.4.2 ORIS-Assisted PLS

An ORIS can improve secrecy by creating controllable reflected paths that favour the legitimate receiver and limit the useful signal available to an eavesdropper [32], [33], [34]. Depending on the mirror configuration, the reflected optical components can increase the legitimate receiver's channel gain, reduce the power directed towards unintended locations, or alter the temporal structure of the eavesdropper's received signal.

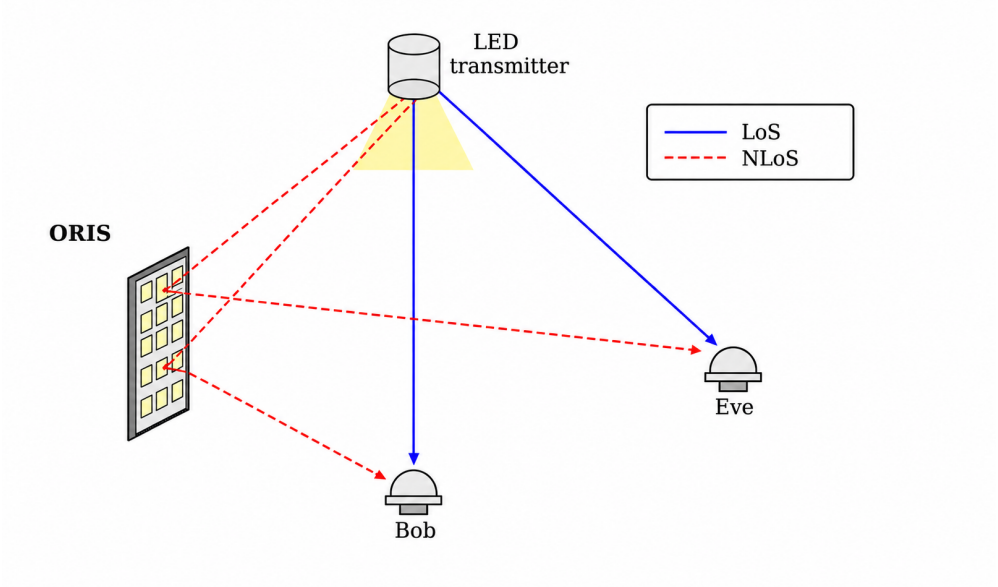


Figure 2.10: ORIS-assisted VLC PLS model with a legitimate receiver and an eavesdropper.

As illustrated in Figure 2.10, the secrecy performance depends on the different direct and reflected channels experienced by Bob and Eve. Conventional ORIS-assisted security designs mainly optimise reflected power or mirror allocation. However, an optical reflected path is longer than the direct LoS path and therefore also introduces propagation delay [35]. This observation motivates the delay-aware security framework developed in Chapter 3.

2.4.3 Delay-Aware Security

In a wideband VLC system, the direct and reflected components may arrive at different times and combine differently at spatially separated receivers. A delay that produces constructive combining at Bob may provide a smaller benefit, or even cause destructive combining, at Eve. Therefore, ORIS-induced delay can be treated as a controllable security resource rather than only as a source of ISI [35].

The usefulness of this mechanism depends on room geometry, receiver position, mirror allocation, and the delay difference between the direct and reflected paths. It also depends on the eavesdropping model. Non-colluding eavesdroppers act independently, whereas colluding eavesdroppers can combine their observations and create a stronger effective adversary. Chapter 3 develops the complete mathematical model for the single-, non-colluding-, and colluding-eavesdropper cases and formulates the corresponding delay-aware ORIS allocation problems [35], [36].

2.5 Codebook Design and Multiple Access

2.5.1 Codebook-Based Beam Steering

In an ideal ORIS, the tilt and sweep angles of each reflecting element could be selected continuously for every user position. Such continuous real-time optimisation is difficult in practice because it requires frequent geometric calculations, accurate position information, and sufficiently precise mirror control. A finite codebook offers a more practical alternative by storing a predefined set of feasible mirror orientations [37], [63], [64].

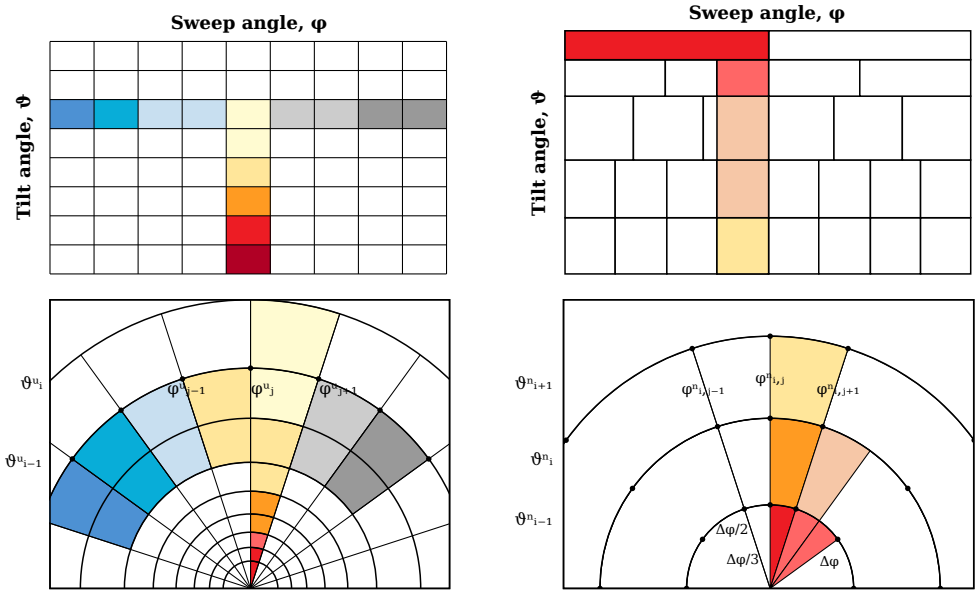
Each codeword represents one tilt–sweep configuration and therefore one reflected beam direction. When the user position is known, an ORIS element selects the codeword whose beam-hit point is closest to the intended receiver location. The quality of the codebook consequently depends on the spatial coverage produced by its available steering states, not only on their separation in the angular domain.

2.5.2 Non-Uniform Codebook Design

A uniform angular codebook uses fixed steps for the tilt and sweep angles. The physical meaning of these two steering angles follows the ORIS geometry introduced earlier in Figure 2.8, where the orientation of each reflecting element determines its surface normal and hence the direction of the reflected optical beam. In the notation used in this thesis, the tilt angle ϑ mainly controls how far the reflected beam reaches from the reference point on the receiver plane, whereas the sweep angle φ controls the angular direction of the reflected beam around that reference point. Each pair (ϑ, φ) therefore represents one codeword and produces a corresponding reflected beam-hit location on the receiver plane.

Although a uniform angular codebook is simple, the mapping from mirror orientation to the beam-hit location is nonlinear. Uniformly spaced angular states can therefore produce densely clustered hit points in some regions and sparse coverage in others [31], [37].

Figure 2.11 illustrates how the tilt and sweep angles are mapped to spatial regions on the receiver plane. The upper panels show the angular codebook using two orthogonal axes, with the sweep angle φ on the horizontal axis and the tilt angle ϑ on the vertical axis. Each coloured cell represents one tilt–sweep codeword. The same colour identifies the corresponding region in the lower panels. When the tilt angle is fixed and the sweep angle is varied, the reflected beam moves through adjacent regions along the same ring. Changing the tilt angle generates rings with different radii. Thus, the upper panels represent the codebook in the angular domain, whereas the lower panels use a ring-and-sector, polar-style representation to illustrate the corresponding spatial distribution of codewords on the receiver plane.



(a) Uniform ORIS codebook (b) Non-uniform ORIS codebook

Figure 2.11: Uniform and non-uniform angular codebooks and their corresponding spatial mapping on the receiver plane.

For the uniform codebook, fixed angular increments can lead to unequal radial and arc-length spacing on the receiver plane. In contrast, the non-uniform codebook adapts the tilt and sweep increments so that the resulting reflected beam locations are distributed more evenly across the intended receiver region. The complete geometric construction, codeword-selection rule, and spatial-error analysis are developed in Chapter 4 [37], [67].

2.5.3 Resource Allocation in NOMA

Multiple-access methods are required when several users share the same optical infrastructure. Orthogonal approaches, including time division multiple access (TDMA), frequency division multiple access (FDMA), and orthogonal frequency division multiple access (OFDMA), assign separate resources to different users. By contrast, power-domain NOMA allows users to share the same time and frequency resources by assigning different power levels and applying successive interference cancellation (SIC) at the receivers [51], [60], [68], [69].

In an ORIS-assisted system, mirror assignment and power allocation are coupled because the selected reflected paths determine the effective user channels. A practical design must therefore decide how the reflecting elements are assigned, how the users are ordered for SIC, and how the available optical power is distributed while satisfying rate, fairness, and optical-intensity constraints. Chapter 4 develops this joint framework using the non-uniform codebook, a quality of service (QoS)-oriented element-allocation method, a gain ratio power allocation (GRPA) benchmark, and sparrow search algorithm (SSA)-based power optimisation.

2.6 Optical Localisation and Sensing

2.6.1 Optical Wireless Positioning

Optical wireless signals are useful not only for communication, but also for localisation and sensing [14], [20], [21]. This is because optical propagation is highly geometry-dependent. The received optical power, incidence angle, delay, and beam footprint are all affected by the relative positions and orientations of the transmitter, receiver, and surrounding objects. Therefore, optical wireless systems can provide spatial information about users and indoor environments while supporting data transmission.

Several methods can be used for optical wireless positioning, including RSS, angle of arrival (AoA), time of arrival (ToA), and time difference of arrival (TDoA). In RSS-based positioning, the received optical power is used to infer the distance or position of the receiver [20], [21]. If the ith optical anchor is located at $\mathbf{p}_i$ and the user is located at $\mathbf{p}_{\mathrm{u}}$, the distance between them can be written as

$$d_i = \|\mathbf{p}_{\mathrm{u}} - \mathbf{p}_i\| . \tag{2.21}$$

The received optical power from the ith anchor is then related to the channel gain by

$$P_{\mathrm{r},i} = h_i(\mathbf{p}_{\mathrm{u}}) P_{\mathrm{t},i}, \tag{2.22}$$

where $P_{\mathrm{t},i}$ is the transmitted optical power of the ith anchor, $P_{\mathrm{r},i}$ is the received optical power from that anchor, and $h_i(\mathbf{p}_{\mathrm{u}})$ is the position-dependent optical channel gain between the ith anchor and the user. Since the channel gain depends on distance, incidence angle, irradiance angle, and receiver orientation, the received power can be used to estimate the user position [20], [70].

When multiple optical anchors are available, the user position can be estimated by solving a geometric fitting problem [20], [70], [71]. A general RSS-based localisation problem can be written as

$$\hat{\mathbf{p}}_{\mathrm{u}} = \arg\min_{\mathbf{p}_{\mathrm{u}}} \sum_{i=1}^{M} \left(P_{\mathrm{r},i} - P_{\mathrm{t},i} h_i(\mathbf{p}_{\mathrm{u}})\right)^2, \tag{2.23}$$

where M is the number of optical anchors and $\hat{\mathbf{p}}_{\mathrm{u}}$ is the estimated user position. This formulation shows that localisation accuracy depends on the number of anchors, anchor geometry, receiver orientation, channel model, and measurement noise.

In ToA-based positioning, the propagation time of the optical signal is used to estimate distance [20], [21]. For the ith anchor, the distance can be approximated as

$$d_i = c\tau_i, \tag{2.24}$$

where c is the speed of light and τ_i is the measured ToA. In TDoA-based positioning, the difference between arrival times from different anchors is used instead of the absolute time. In AoA-based positioning, the arrival direction of the optical signal is used to infer the receiver position. Each method has different requirements in terms of synchronisation, receiver complexity, angular resolution, and measurement accuracy.

Compared with RF-based positioning, optical wireless positioning can provide high spatial resolution because optical signals have strong directionality and short wavelengths [14], [20], [21]. However, it is also more sensitive to blockage, receiver FoV, user orientation, and shadowing [14], [24], [25]. Therefore, robust optical localisation often requires careful anchor placement, suitable receiver design, and accurate channel modelling.

2.6.2 VCSEL-Based Localisation and Sensing

Optical localisation can use different source characteristics according to the required coverage and spatial resolution. LED-based localisation benefits from existing lighting infrastructure and broad Lambertian illumination, making it suitable for coverage-oriented positioning [13], [20], [43]. By comparison, VCSELs provide narrow, directional, and spatially controllable beams, making them suitable for scanning-based localisation, mapping, and sensing [38], [40].

Moreover, VCSELs can be integrated around or within a LeRIS panel to provide optical reference beams for localisation and environmental sensing [62]. A receiver can estimate its position by observing the received optical power from multiple optical anchors. Since the beam footprint is narrow, the received power changes sharply with position and orientation, which can provide useful spatial information.

The VCSEL-based localisation considered in this thesis does not rely on continuously flooding the room with a fixed array of optical beams. Instead, the narrow VCSEL beams are scanned over predefined angular regions. Each LeRIS panel scans approximately 120° in azimuth and 60° in elevation, allowing different spatial directions to be examined sequentially. Localisation outage may occur when a user lies outside the scanning coverage of the available LeRIS panels or when the received beam falls outside the receiver FoV. The use of multiple LeRIS panels provides overlapping spatial coverage and reduces such uncovered regions. The variation of the Gaussian beam footprint with propagation distance is accounted for through the beam-propagation and received-power model rather than by assuming uniform optical illumination.

The received power of a VCSEL beam follows the Gaussian intensity model introduced in Section 2.2.4. In sensing applications, reflected optical signals can also indicate the presence of obstacles. By combining received power, beam direction, and delay information, the system can infer the approximate location of blocking objects in the indoor environment.

Other established technologies, including structured-light systems, ultra-wideband (UWB), light detection and ranging (LiDAR), and specialised laser-based three-dimensional (3D) sensing, can also provide indoor localisation and environmental information. These approaches offer different trade-offs in positioning accuracy, coverage, hardware complexity, and sensing capability. The objective of the VCSEL-based approach in this thesis is not to replace these established localisation technologies, but to integrate optical localisation and sensing directly with the LeRIS architecture. The resulting user- and obstacle-location information can therefore be used to configure the programmable mmWave communication path within the same system framework.

In this thesis, VCSEL-based sensing is used to support the LeRIS concept. The main role of the VCSELs is to provide spatial awareness, including user location, receiver orientation, and obstacle presence. This information can then be used to configure the LeRIS-assisted mmWave communication link. Therefore, VCSELs act as compact optical sensing anchors that support intelligent and adaptive wireless operation.

2.6.3 Environment-Aware mmWave Communication

mmWave communication is an important candidate for high-capacity indoor wireless systems because it can provide substantially wider channel bandwidths than conventional microwave systems. For example, bandwidths exceeding 1 GHz have been considered at 28 and 38 GHz [41], while 60 GHz systems such as Institute of Electrical and Electronics Engineers (IEEE) 802.11ad use channel bandwidths of approximately 2.16 GHz and can support physical-layer data rates of up to approximately 6.8 Gb/s. These representative values illustrate the multi-gigahertz bandwidth and multi-gigabit-per-second data-rate capability of mmWave communication. However, mmWave links are highly sensitive to blockage, path loss, and beam misalignment [41], [42], [72]. In indoor environments, objects such as walls, furniture, and human bodies can obstruct the direct path between the transmitter and receiver, so reliable operation often requires accurate beam alignment and alternative reflected paths.

LeRIS can support mmWave communication by creating controllable reflected paths between an AP and a user. The selection of a suitable path depends on the positions of the AP, LeRIS panels, user, and obstacles. This creates a direct link between optical sensing and mmWave communication: the VCSELs provide user and obstacle information, and the LeRIS uses this information to configure a suitable communication route.

This background supports Chapter 5, in which VCSEL-based localisation and mapping are used to assist LeRIS-based mmWave communication. The chapter investigates how optical spatial awareness can improve beam routing, blockage avoidance, and communication performance in programmable indoor environments.

2.7 Summary

This chapter presented the background and related work required for the technical developments in this thesis. It first introduced the historical evolution of OWC, from early optical wireless demonstrations to modern VLC, LiFi, ORIS, and intelligent optical wireless systems. The basic optical wireless system structure was then discussed, including optical transmitters, optical receivers, IM/DD transmission, and the indoor optical channel model. Particular attention was given to LoS and NLoS propagation, receiver FoV, optical beam models, noise, blockage, and mobility, because these factors strongly affect the performance of indoor optical wireless systems.

The chapter then reviewed ORIS and LeRIS technologies and their distinct roles in this thesis. For ORIS systems, optical reflection is governed mainly by GO, mirror orientation, and the spatial hit point of the reflected beam. For LeRIS systems, optical localisation and sensing provide the environmental awareness required to configure adaptive mmWave communication. These concepts provide the foundation for the ORIS-assisted VLC contributions and the integrated LeRIS framework developed in the following chapters.

Building on this technological background, the chapter also discussed PLS in indoor VLC, in which the spatial confinement of light provides useful security advantages, but does not fully prevent eavesdropping by receivers located inside the illuminated region. The use of ORIS technology to improve the legitimate channel and degrade the eavesdropping channel was introduced, together with the role of ORIS-induced time delay as a potential security-enhancing mechanism. This provides the foundation for Chapter 3, in which delay-aware ORIS-assisted VLC security is investigated.

Following the security discussion, the chapter then introduced codebook-based beam steering and multiple access for ORIS-assisted VLC. It was shown that finite codebooks are needed for practical ORIS deployment, because continuous real-time mirror optimisation is difficult. However, uniform angular codebooks may not provide uniform spatial coverage due to the nonlinear mapping between mirror orientation and receiver-plane hit points. This motivates the non-uniform codebook design and NOMA-based resource allocation framework developed in Chapter 4.

Finally, optical localisation and sensing were reviewed, with emphasis on RSS, AoA, ToA, and TDoA-based positioning methods. The discussion showed that LEDs provide broad illumination that is suitable for coverage-oriented localisation, while VCSELs provide narrow and directional beams that are suitable for spatially selective localisation and mapping. The concept of LeRIS was also introduced, in which optical sources such as VCSELs can be integrated with or placed around a reflecting surface to provide localisation, mapping, and environmental awareness. This motivates the VCSEL-based LeRIS framework studied in Chapter 5, in which optical sensing is used to support environment-aware LeRIS-assisted mmWave communication.

Overall, this chapter established the technical foundation for the three main contributions of the thesis, namely delay-aware PLS in ORIS-assisted VLC, practical non-uniform codebook design for ORIS-assisted VLC, and VCSEL-based localisation and mapping for environment-aware LeRIS-assisted mmWave communication. The following chapter begins with the first of these contributions by investigating ORIS-induced time delay for enhanced PLS in indoor VLC systems.

Chapter 3

Delay-Aware Physical Layer Security in ORIS-Assisted VLC Systems

3.1 Introduction

This chapter focuses on delay-aware security in indoor VLC. The increasing demand for high-speed indoor wireless connectivity has motivated the development of VLC as a complementary technology to conventional RF communication. By using the visible light spectrum for simultaneous illumination and data transmission, VLC can provide high data rates, licence-free bandwidth, and reduced electromagnetic interference [13], [14]. In addition, due to the directional nature of optical beams and the inability of light to penetrate opaque walls, VLC can offer a higher level of inherent security compared with RF systems [44], [45].

However, the security of indoor VLC systems cannot be guaranteed by the physical confinement of light alone. In practical indoor environments, an eavesdropper may be located inside the illuminated region and can receive the confidential optical signal through the direct LoS link or through reflected links [73], [74]. These limitations have

motivated the use of PLS techniques in indoor VLC systems, in which secrecy performance can be improved by exploiting the spatial confinement of optical beams, beamforming, receiver geometry, and channel differences between the legitimate receiver and eavesdroppers [28], [29], [75].

More recently, ORIS-assisted VLC has been investigated as a promising approach for improving coverage and enhancing secrecy by creating additional controllable reflected paths [33], [34], [76]. In such systems, the ORIS can redirect part of the incident optical signal towards the legitimate receiver, usually referred to as Bob, while reducing information leakage to eavesdroppers. This makes the ORIS a useful tool for improving indoor VLC security without significantly changing the transmitter or receiver hardware.

However, most existing studies on ORIS-assisted VLC secrecy focus on improving the channel gain or received optical power, while the delay introduced by the reflected optical path is often neglected [35]. In indoor VLC, the reflected signal travels through a longer path than the direct LoS signal. Therefore, the ORIS-reflected component reaches the receiver with an additional propagation delay. This delay is usually considered an impairment because it may cause signal distortion and ISI. However, from a security perspective, the same delay can also be exploited as an additional design resource.

The key observation is that Bob and the eavesdropper are usually located at different positions in the room. As a result, the delayed ORIS-reflected components do not affect them in the same way. A reflected path that improves the received signal quality at Bob may not provide the same benefit to the eavesdropper. In some cases, the delayed component may even degrade the eavesdropper's received signal. This creates a new opportunity for delay-aware PLS in ORIS-assisted VLC systems.

Motivated by this observation, this chapter investigates delay-aware PLS in ORIS-assisted VLC systems. The chapter builds on the delay-aware secrecy framework first introduced in [35], in which ORIS-induced time delay is exploited to improve secrecy in the presence of a single eavesdropper. The analysis is then extended to a more practical

multiple-eavesdropper scenario, including both non-colluding and colluding eavesdroppers, as developed in [36]. In this way, the chapter presents a connected secrecy framework that moves from a single-eavesdropper case to a more general indoor eavesdropping model.

The main contributions of this chapter are summarised as follows:

- The secrecy performance is analysed for a single-eavesdropper scenario, in which the ORIS element allocation is designed to enhance the legitimate receiver while limiting the eavesdropper.
- The analysis is extended to multiple eavesdroppers, including non-colluding and colluding cases, to provide a more practical indoor secrecy model.
- Delay-aware ORIS element allocation is formulated as an optimisation problem and solved using the genetic algorithm (GA) and proximal policy optimisation (PPO) methods.

The remainder of this chapter is organised as follows. Section 3.2 presents the ORIS-assisted indoor VLC system model and the delay-aware channel representation. Section 3.3 introduces the secrecy performance analysis for single- and multiple-eavesdropper scenarios. Section 3.4 presents the delay-aware ORIS element allocation problem and the corresponding optimisation methods. Section 3.5 discusses the simulation results. Finally, Section 3.6 summarises the chapter.

3.2 System and Channel Model

3.2.1 ORIS-Assisted Indoor VLC Network

To analyse the proposed delay-aware security framework, this section considers a downlink indoor ORIS-assisted VLC network, as shown in Figure 3.1, in which a ceiling-mounted optical transmitter, referred to as Alice, communicates with a legitimate receiver, referred to as Bob. Bob is located at position $\mathbf{p}_{\mathrm{B}}$ on the receiver plane. In addition, M passive eavesdroppers may exist inside the illuminated region. The mth eavesdropper is denoted by E_m and is located at position $\mathbf{p}_{\mathrm{E},m}$, where $m = 1, 2, \ldots, M$.

An ORIS is installed on one side of the room to create additional controllable reflected optical paths. The ORIS consists of N reflecting elements, and the separation distance between adjacent reflecting elements is denoted by D. The ORIS redirects the incident light by changing the physical orientation of its reflecting elements. Therefore, each reflecting element can steer the incident optical beam towards a selected direction.

The transmitted optical signal can reach Bob and the eavesdroppers through two types of links. The first is the direct LoS link from Alice to the receiver. The second is the ORIS-assisted reflected link, in which the signal first travels from Alice to an ORIS element and is then reflected towards the receiver. Since the reflected path is longer than the direct path, it introduces an additional propagation delay. This delay may cause ISI; however, in this chapter, it is exploited as a useful feature for enhancing PLS.

To control the contribution of the ORIS elements, an allocation vector is defined as

$$\mathbf{s} = [s_1, s_2, \ldots, s_N], \tag{3.1}$$

where s_n denotes the allocation state of the nth ORIS element. The allocation vector is designed to improve secrecy by selecting the reflected paths that enhance Bob's received signal while reducing the useful signal received by the eavesdroppers.

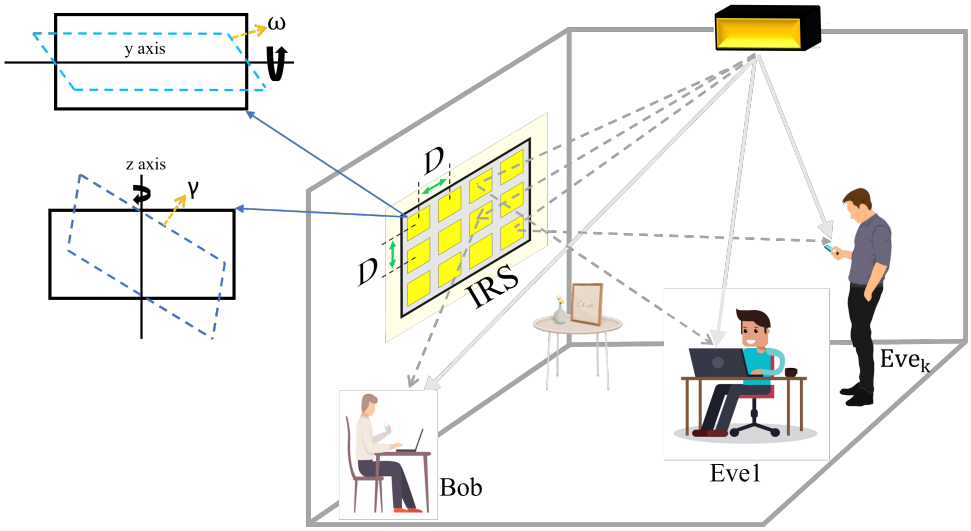


Figure 3.1: Indoor ORIS-assisted VLC system with one legitimate receiver and multiple passive eavesdroppers.

3.2.2 Channel Model and ORIS-Induced Time Delay

The optical channel between Alice and any receiver consists of a direct LoS component and multiple ORIS-reflected components. Let k denote a generic receiver, where $k = \mathrm{B}$ represents Bob and $k = \mathrm{E}_m$ represents the mth eavesdropper. The direct LoS component reaches the receiver through the shortest optical path, while the reflected components travel from Alice to the ORIS and then from the ORIS to the receiver. Therefore, the reflected components introduce additional propagation delays compared with the direct link.

Moreover, the channel model used in this chapter follows the indoor VLC channel definitions introduced in Chapter 2. To avoid repeating the LoS and ORIS-assisted channel-gain expressions, this chapter uses compact notation for the direct and reflected links. Let k denote a generic receiver, where $k = \mathrm{B}$ represents Bob and $k = \mathrm{E}_m$ represents the mth eavesdropper. The direct LoS channel gain between Alice and receiver k is denoted

by $h_{k,\mathrm{LoS}}$, while the reflected channel gain from Alice to receiver k through the nth ORIS element is denoted by $h_{k,n}$. These gains are real-valued optical channel gains determined by the link geometry, optical front-end parameters, receiver FoV, and the orientation of the corresponding ORIS element.

Importantly, the effect of different propagation delays on an optical wireless channel is a general multipath phenomenon and is not specific to the security scenario considered in this chapter. Previous indoor optical channel studies have shown that delayed direct and reflected components form the time-domain channel impulse response, whose Fourier transform produces a frequency-dependent response with peaks and notches due to constructive and destructive combining [77], [78]. Similar path-length-dependent frequency notches have also been observed in practical orthogonal frequency division multiplexing (OFDM)-based LiFi systems using multiple optical transmitters [79]. In this thesis, the same physical principle is exploited using controllable ORIS-reflected paths for PLS.

The propagation delay of the direct LoS path is given by

$$\tau_{k,\mathrm{LED}} = \frac{d_{k,\mathrm{LED}}}{c}, \tag{3.2}$$

while the propagation delay of the reflected path through the nth ORIS element is given by

$$\tau_{k,n,\mathrm{LED}} = \frac{d_{\mathrm{LED},n} + d_{k,n}}{c}, \tag{3.3}$$

where c is the speed of light. Since the reflected path is longer than the direct path, the reflected signal arrives later than the corresponding LoS component.

Using the path gains and delays, the channel impulse response of receiver k can be expressed as

$$q_k(t) = h_{k,\mathrm{LoS}}\delta(t - \tau_{k,\mathrm{LED}}) + \sum_{n=1}^{N} a_{k,n}h_{k,n}\delta(t - \tau_{k,n,\mathrm{LED}}), \tag{3.4}$$

where $a_{k,n} \in \{0,1\}$ indicates whether the reflected path from the nth ORIS element contributes to receiver k. The first term represents the direct LoS path, while the summation represents the multiple delayed ORIS-reflected paths.

In this formulation, Equation (3.4) is not restricted to a two-ray channel, since the summation includes the reflected paths generated by all active ORIS elements. The finite physical area of the photodetector is already included in the channel gains $h_{k,\mathrm{LoS}}$ and $h_{k,n}$ through the receiver-area term defined in Chapter 2. In this chapter, uncontrolled diffuse reflections from walls, ceiling, floor, and furniture are neglected so that the effect of the deliberately controlled ORIS-induced delays can be evaluated separately.

Accordingly, the corresponding channel frequency response is obtained directly by taking the Fourier transform of the channel impulse response,

$$Q_k(f) = \mathscr{F}\{q_k(t)\} = h_{k,\mathrm{LoS}} e^{-j2\pi f \tau_{k,\mathrm{LED}}} + \sum_{n=1}^{N} a_{k,n} h_{k,n} e^{-j2\pi f \tau_{k,n,\mathrm{LED}}}, \tag{3.5}$$

As a result, the different propagation delays cause the direct and reflected signal components to combine differently across frequency. At some frequencies, the received components combine constructively and increase the channel response, while at other frequencies they combine destructively and reduce it, producing peaks and notches in the frequency response. Therefore, the delay differences between the propagation paths directly determine the frequency-dependent behaviour of the ORIS-assisted channel.

The corresponding real-valued channel power gain is $\mathscr{G}_k(f) = |Q_k(f)|^2$, which can be expressed as

$$\begin{aligned} \mathscr{G}_k(f) =& h_{k,\mathrm{LoS}}^2 + \sum_{n=1}^{N} a_{k,n} h_{k,n}^2 + 2h_{k,\mathrm{LoS}} \sum_{n=1}^{N} a_{k,n} h_{k,n} \cos\left(2\pi f \Delta\tau_{k,n}\right) \\ &+ \sum_{n=1}^{N} \sum_{u<n} 2a_{k,n} a_{k,u} h_{k,n} h_{k,u} \cos\left(2\pi f \Delta\tau_{k,u,n}\right), \end{aligned} \tag{3.6}$$

where $\Delta\tau_{k,n} = \tau_{k,n,\mathrm{LED}} - \tau_{k,\mathrm{LED}}$ is the delay difference between the nth reflected path and the direct path, and $\Delta\tau_{k,u,n} = \tau_{k,u,\mathrm{LED}} - \tau_{k,n,\mathrm{LED}}$ is the delay difference between two reflected paths.

In particular, the cosine terms in (3.6) show how the path-delay differences affect the received power across frequency. In the time domain, sufficiently large delay differences can spread the received signal and contribute to ISI. In the frequency domain, these same delay differences cause the received components to combine constructively at some frequencies and destructively at others, producing peaks and notches in the channel response.

To illustrate this behaviour, Figure 3.2 shows the normalised channel gain for representative delay differences using a simplified direct-plus-reflected-path example. Increasing the delay difference changes the spacing and locations of the frequency-domain notches, illustrating how the relative propagation delay influences the channel response. The full multi-element ORIS model in (3.6) extends this principle to multiple reflected paths.

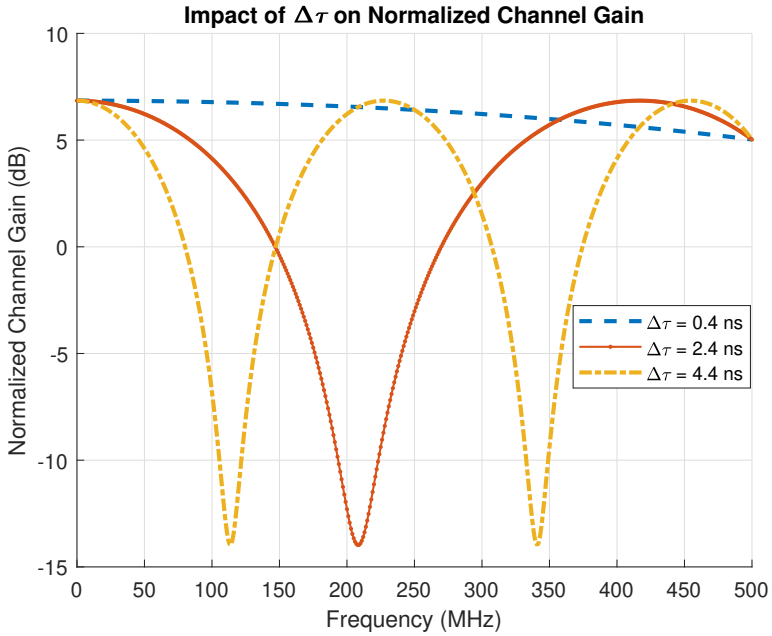


Figure 3.2: Illustration of the effect of path-delay difference on the normalised channel gain.

The frequency-dependent SNR at receiver k is then expressed as [35], [36]

$$\gamma_k(f) = \frac{2T_{\text{sym}}E(f)P_{\text{t}}^2R_{\text{PD}}^2\mathscr{G}_k(f)}{\Gamma\kappa^2N_0}, \tag{3.7}$$

where T_{sym} is the symbol period, $E(f)$ is the power distribution over frequency, Γ is the gap between theoretical and practical system performance, and N_0 is the noise power spectral density.

For the considered direct current-biased optical orthogonal frequency division multiplexing (DCO-OFDM) transmission, κ is a dimensionless modulation scaling factor that relates the peak amplitude of the OFDM waveform to its root-mean-square amplitude. It accounts for the signal scaling required to limit clipping in the optical transmitter.

Finally, the delay-induced peaks and notches themselves are an established multipath optical-channel effect. The contribution of this chapter is to exploit this effect through controllable ORIS paths for security. Since Bob and the eavesdroppers occupy different positions, their path gains and relative delays are different. An ORIS allocation can therefore produce favourable constructive combining over parts of Bob's signal bandwidth while producing less favourable or destructive combining at an eavesdropper. The resulting difference in their achievable rates is then exploited to enhance PLS.

3.3 Secrecy Performance Analysis

This section presents the secrecy performance analysis of the delay-aware ORIS-assisted VLC system. The analysis is based on the achievable rate of Bob and the achievable rate of the eavesdroppers. Since the ORIS-reflected paths introduce propagation delay, the received signal quality is frequency dependent. Therefore, the achievable rate is calculated over the signal bandwidth rather than using only a single channel gain value.

Following the delay-aware DCO-OFDM rate formulation used in the related ORIS-assisted VLC studies [35], [36], [78], [80], for a generic receiver k, where $k = \mathrm{B}$ represents Bob and $k = \mathrm{E}_m$ represents the mth eavesdropper, the achievable rate is given by

$$R_k = \int_0^{\frac{1}{2T_{\mathrm{sym}}}} \log_2\left(1+\gamma_k(f)\right) \mathrm{d}f. \tag{3.8}$$

Following the notation adopted in [78], T_{sym} denotes the communication symbol period. The considered modulation bandwidth is $B = 1/(2T_{\mathrm{sym}})$, and therefore $1/(2T_{\mathrm{sym}})$ forms the upper integration limit in (3.8).

For Bob, the achievable rate is written as

$$R_{\mathrm{B}} = \int_0^{\frac{1}{2T_{\mathrm{sym}}}} \log_2\left(1+\gamma_{\mathrm{B}}(f)\right) \mathrm{d}f. \tag{3.9}$$

Similarly, the achievable rate of the mth eavesdropper is given by

$$R_{\mathrm{E},m} = \int_0^{\frac{1}{2T_{\mathrm{sym}}}} \log_2\left(1+\gamma_{\mathrm{E},m}(f)\right) \mathrm{d}f, \tag{3.10}$$

where $m = 1, 2, \ldots, M$.

3.3.1 Single-Eavesdropper Scenario

The single-eavesdropper scenario represents the basic delay-aware PLS model. In this case, one passive eavesdropper is located inside the illuminated area and attempts to decode the confidential signal intended for Bob. For a given ORIS allocation vector $\mathbf{s}$, the secrecy capacity is defined as the positive difference between Bob's achievable rate and Eve's achievable rate, and is given by

$$C_{\mathrm{s}} = \left[R_{\mathrm{B}} - R_{\mathrm{E}}\right]^{+}, \tag{3.11}$$

where $[x]^+ = \max(x, 0)$. A positive secrecy capacity is achieved when Bob obtains a higher achievable rate than Eve. If Eve achieves an equal or higher rate than Bob, the secrecy capacity becomes zero.

In the single-eavesdropper case, the binary allocation vector controls whether each ORIS element assists Bob or Eve. When $s_n = 1$, the nth ORIS element is allocated to Bob; when $s_n = 0$, it is allocated to Eve. Hence, the contribution indicator in (3.4) is set as $a_{\mathrm{B},n} = s_n$ for Bob and $a_{\mathrm{E},n} = 1 - s_n$ for Eve. The corresponding rates are then obtained from (3.8) using the frequency-dependent SNR in (3.7). The allocation is designed so that the selected reflected paths create constructive ISI at Bob and destructive ISI at Eve [35].

3.3.2 Single-Eavesdropper Scenario

The single-eavesdropper scenario represents the basic delay-aware PLS model. In this case, one passive eavesdropper is located inside the illuminated area and attempts to decode the confidential signal intended for Bob. For a given ORIS allocation vector $\mathbf{s}$, the secrecy capacity is defined as the positive difference between Bob's achievable rate and Eve's achievable rate, and is given by

$$C_{\mathrm{s}} = [R_{\mathrm{B}} - R_{\mathrm{E}}]^+, \tag{3.12}$$

where $[x]^+ = \max(x, 0)$. A positive secrecy capacity is achieved when Bob obtains a higher achievable rate than Eve. If Eve achieves an equal or higher rate than Bob, the secrecy capacity becomes zero.

In the single-eavesdropper case, the binary allocation vector controls whether each ORIS element assists Bob or Eve. When $s_n = 1$, the nth ORIS element is allocated to Bob; when $s_n = 0$, it is allocated to Eve. Hence, the contribution indicator in (3.4) is set as $a_{\mathrm{B},n} = s_n$ for Bob and $a_{\mathrm{E},n} = 1 - s_n$ for Eve. The corresponding rates are then obtained from (3.8) using the frequency-dependent SNR in (3.7). The allocation is designed so that the selected reflected paths create constructive ISI at Bob and destructive ISI at Eve [35].

3.3.3 Multiple-Eavesdropper Scenario

The single-eavesdropper model is then extended to a more practical scenario with M passive eavesdroppers. The eavesdroppers may be located at different positions in the room and may experience different direct and reflected channels. Two eavesdropping models are considered, namely non-colluding and colluding eavesdroppers.

In the non-colluding case, the eavesdroppers act independently and do not share their received signals. Therefore, the secrecy performance is limited by the strongest eavesdropper, which has the highest achievable rate. The secrecy capacity for the non-colluding case is expressed as

$$C_{\mathrm{s}}^{\mathrm{NC}} = \left[R_{\mathrm{B}} - \max_{m \in \{1,\ldots,M\}} \left\{ R_{\mathrm{E},m} \right\} \right]^{+}. \tag{3.13}$$

This expression shows that even if most eavesdroppers have weak channels, the eavesdropper with the largest achievable rate determines the secrecy capacity.

In the colluding case, the eavesdroppers cooperate and combine their received signals. This represents a stronger eavesdropping model because the eavesdroppers jointly improve their decoding capability. Following the maximum-ratio combining model, the effective SNR of the colluding eavesdropping group is given by

$$\gamma_{\mathrm{E}}^{\mathrm{C}}(f) = \sum_{m=1}^{M} \gamma_{\mathrm{E},m}(f). \tag{3.14}$$

The corresponding achievable rate of the colluding eavesdropping group is [78], [80]

$$R_{\mathrm{E}}^{\mathrm{C}} = \int_0^{\frac{1}{2T_{\mathrm{sym}}}} \log_2\left(1+\gamma_{\mathrm{E}}^{\mathrm{C}}(f)\right) \mathrm{d}f. \tag{3.15}$$

Therefore, the secrecy capacity under colluding eavesdroppers is written as

$$C_{\mathrm{s}}^{\mathrm{C}} = \left[R_{\mathrm{B}} - R_{\mathrm{E}}^{\mathrm{C}}\right]^{+}. \tag{3.16}$$

Compared with the non-colluding case, the colluding case is more challenging because the eavesdroppers combine their received signals and increase their effective eavesdropping capability [36].

3.3.4 Approximate Secrecy Analysis

Building on the exact secrecy formulation above, the rate expression in (3.8) requires numerical integration because the ORIS-assisted channel is frequency selective. To provide a more tractable expression and to show the effect of the delay terms more clearly, an approximate analytical rate expression can be derived by separating the frequency-independent and frequency-dependent parts of the channel response.

For compact notation, let

$$G_{\mathrm{LoS},k} = h_{k,\mathrm{LoS}}, \qquad G_{i,k} = h_{k,i}, \tag{3.17}$$

where $G_{\mathrm{LoS},k}$ is the direct LoS gain of receiver k, and $G_{i,k}$ is the reflected gain through the ith ORIS element. Similarly, let

$$\tau_{\mathrm{LoS},k} = \tau_{k,\mathrm{LED}}, \qquad \tau_{i,k} = \tau_{k,i,\mathrm{LED}}. \tag{3.18}$$

Assuming a flat power distribution, $E(f) = 1$, the frequency-independent SNR coefficient is defined as [78]

$$\Lambda = \frac{2T_{\text{sym}} P_{\text{t}}^2 R_{\text{PD}}^2}{\Gamma \kappa^2 N_0}. \tag{3.19}$$

Using these definitions, the achievable rate of receiver k can be written as

$$\begin{aligned} R_k = \int_0^{\frac{1}{2T_{\text{sym}}}} \log_2 \Bigg(1 + \Lambda \Bigg(& G_{\text{LoS},k}^2 + \sum_{i=1}^{N} G_{i,k}^2 \\ & + 2G_{\text{LoS},k} \sum_{i=1}^{N} G_{i,k} \cos\left(2\pi f \left(\tau_{i,k} - \tau_{\text{LoS},k}\right)\right) \\ & + \sum_{i=1}^{N} \sum_{u<i} 2G_{i,k} G_{u,k} \cos\left(2\pi f \left(\tau_{u,k} - \tau_{i,k}\right)\right) \Bigg) \Bigg) \mathrm{d}f. \end{aligned} \tag{3.20}$$

The first two terms represent the frequency-independent power contribution of the direct and reflected paths. The remaining cosine terms represent the delay-dependent interaction between the direct and reflected components, and also between different reflected components.

The frequency-independent term is collected as

$$D_k = 1 + \Lambda \left(G_{\text{LoS},k}^2 + \sum_{i=1}^{N} G_{i,k}^2 \right), \tag{3.21}$$

while the frequency-dependent term is written as

$$\begin{aligned} N_k(f) = & 2G_{\text{LoS},k} \sum_{i=1}^{N} G_{i,k} \cos\left(2\pi f \left(\tau_{i,k} - \tau_{\text{LoS},k}\right)\right) \\ & + \sum_{i=1}^{N} \sum_{u<i} 2G_{i,k} G_{u,k} \cos\left(2\pi f \left(\tau_{u,k} - \tau_{i,k}\right)\right). \end{aligned} \tag{3.22}$$

Therefore, the achievable rate can be decomposed as

$$R_k = \frac{1}{2T_{\text{sym}}} \log_2\left(D_k\right) + \int_0^{\frac{1}{2T_{\text{sym}}}} \log_2\left(1 + \frac{\Lambda N_k(f)}{D_k}\right) \mathrm{d}f. \tag{3.23}$$

The first term captures the contribution of the average received power, while the second term captures the additional effect of frequency selectivity caused by the ORIS-induced delays.

Following the approximation used in [36], the achievable rate of receiver k can be approximated as

$$\begin{aligned} R_k^{\text{approx}} \approx & \frac{1}{2T_{\text{sym}}} \log_2 (D_k) \\ & + \frac{\Lambda}{D_k \ln(2)} \left[\frac{G_{\text{LoS},k}}{T_{\text{sym}}} \sum_{i=1}^{N} G_{i,k} \left(1 - \frac{\sin\left(\frac{\pi(\tau_{i,k} - \tau_{\text{LoS},k})}{T_{\text{sym}}} \right)}{\frac{\pi(\tau_{i,k} - \tau_{\text{LoS},k})}{T_{\text{sym}}}} \right) \right. \\ & \left. + \frac{1}{T_{\text{sym}}} \sum_{i=1}^{N} \sum_{u<i} G_{i,k} G_{u,k} \left(1 - \frac{\sin\left(\frac{\pi(\tau_{u,k} - \tau_{i,k})}{T_{\text{sym}}} \right)}{\frac{\pi(\tau_{u,k} - \tau_{i,k})}{T_{\text{sym}}}} \right) \right]. \end{aligned} \tag{3.24}$$

Equation (3.24) shows how the delay differences affect the achievable rate through multiple weighted sine-ratio terms. The first summation represents the delay differences between the LoS and ORIS-reflected paths, while the second represents the delay differences between pairs of reflected paths. Each contribution is weighted by the corresponding channel gains, and therefore different path delays and gains contribute differently to the achievable rate.

Using the approximate rate expression, the secrecy capacity for the non-colluding case can be approximated as

$$C_{\text{s,approx}}^{\text{NC}} = \left[R_{\text{B}}^{\text{approx}} - \max_{m \in \{1,\ldots,M\}} \left\{ R_{\text{E},m}^{\text{approx}} \right\} \right]^{+}. \tag{3.25}$$

Similarly, for the colluding case, the approximate secrecy capacity can be written as

$$C_{\text{s,approx}}^{\text{C}} = \left[R_{\text{B}}^{\text{approx}} - R_{\text{E,approx}}^{\text{C}} \right]^{+}. \tag{3.26}$$

The approximate analysis is useful because it highlights the role of ORIS-induced delay without requiring repeated numerical integration for every allocation pattern. It also provides a compact way to understand why the same ORIS configuration can improve Bob's rate while reducing the effective eavesdropping rate.

3.4 Delay-Aware ORIS Element Allocation and Optimisation

The secrecy analysis in the previous section shows that the secrecy capacity depends on the ORIS allocation vector **s**. Different allocation vectors produce different reflected paths, and these paths affect Bob and the eavesdroppers differently because of differences in their channel gains and propagation delays. Therefore, the main design problem is to find an ORIS element allocation that improves Bob's achievable rate while reducing the eavesdropping rate.

3.4.1 ORIS Element Allocation Problem

For the single-eavesdropper scenario, each ORIS element is assigned according to a binary allocation variable. The allocation state of the nth element is defined as

$$s_n \in \{0,1\}, \qquad n = 1,2,\ldots,N. \tag{3.27}$$

In this model, $s_n = 1$ indicates that the nth ORIS element is allocated to assist Bob, while $s_n = 0$ indicates that it is not allocated to Bob. The complete allocation vector is the vector **s** already defined in Section 3.2.1, and therefore it is not repeated here.

For a given allocation vector, the frequency-dependent channel power gains of Bob and Eve are calculated, and the corresponding secrecy capacity is obtained from (3.12).

The secrecy maximisation problem for the single-eavesdropper case can be formulated as

$$\mathbf{s}^{\star} = \arg\max_{\mathbf{s}} C_{\mathrm{s}}(\mathbf{s}), \tag{3.28}$$

subject to the binary allocation constraint in (3.27). The objective is to select the allocation vector that maximises the secrecy capacity. Since each of the N reflecting elements has two possible states, the number of possible allocation vectors is 2^N. Therefore, exhaustive search becomes computationally expensive when the number of ORIS elements increases.

For the multiple-eavesdropper case, the allocation problem is extended according to the considered eavesdropping model. In the non-colluding case, the optimisation problem is written as

$$\mathbf{s}^{\star}_{\mathrm{NC}} = \arg\max_{\mathbf{s}} C_{\mathrm{s}}^{\mathrm{NC}}(\mathbf{s}), \tag{3.29}$$

where $C_{\mathrm{s}}^{\mathrm{NC}}(\mathbf{s})$ is the secrecy capacity under non-colluding eavesdroppers. In the colluding case, the optimisation problem becomes

$$\mathbf{s}^{\star}_{\mathrm{C}} = \arg\max_{\mathbf{s}} C_{\mathrm{s}}^{\mathrm{C}}(\mathbf{s}), \tag{3.30}$$

where $C_{\mathrm{s}}^{\mathrm{C}}(\mathbf{s})$ is the secrecy capacity under colluding eavesdroppers. These problems are more challenging than the single-eavesdropper case because the allocation must account for several eavesdroppers with different locations, channel gains, and delay profiles.

3.4.2 GA-Based Allocation

The single-eavesdropper allocation problem is a binary combinatorial optimisation problem. Although exhaustive search can find the optimal solution, it requires checking all 2^N possible allocation vectors and becomes impractical as the number of ORIS elements increases. A GA is a population-based heuristic optimisation method inspired by natural selection. It starts with a set of candidate solutions and improves them over successive

generations using selection, crossover, and mutation. In this chapter, each candidate solution represents one possible ORIS allocation vector, and the fitness value is the resulting secrecy capacity. Therefore, the GA is suitable for the single-eavesdropper case because it can search the binary allocation space without testing every possible combination. Therefore, a GA is used to obtain a near-optimal allocation with lower computational complexity [35], [81].

In the GA, each candidate solution is represented by a chromosome. In this chapter, a chromosome corresponds to one possible ORIS allocation vector,

$$\mathbf{s}^{(p)} = \left[s_1^{(p)}, s_2^{(p)}, \ldots, s_N^{(p)} \right], \tag{3.31}$$

where $\mathbf{s}^{(p)}$ denotes the pth candidate allocation vector in the population. Each gene $s_n^{(p)}$ is a binary value that represents the allocation state of the nth ORIS element.

The quality of each candidate solution is measured using a fitness function. Since the objective is to maximise secrecy capacity, the fitness function is defined as

$$F\left(\mathbf{s}^{(p)}\right) = C_{\mathrm{s}}\left(\mathbf{s}^{(p)}\right). \tag{3.32}$$

A larger fitness value means that the corresponding allocation vector provides a higher secrecy capacity.

The GA starts with an initial population of random allocation vectors. For each allocation vector, the frequency-dependent channel power gains of Bob and Eve are calculated, followed by the achievable rates and secrecy capacity. Then, candidate solutions with higher fitness values are more likely to be selected for reproduction. New allocation vectors are generated through crossover and mutation operations. The crossover operation combines parts of two parent allocation vectors, while the mutation operation randomly changes some allocation states to maintain diversity in the search process.

The algorithm iteratively updates the population until a stopping condition is reached, such as the maximum number of generations or convergence of the best fitness value. The final output is the best allocation vector found by the algorithm,

$$\mathbf{s}_{\mathrm{GA}}^{\star} = \arg \max_{\mathbf{s}^{(p)} \in \mathscr{P}} F\left(\mathbf{s}^{(p)}\right), \tag{3.33}$$

where $\mathscr{P}$ denotes the final population. This allocation vector is then used to evaluate the final secrecy capacity of the single-eavesdropper scenario. The detailed steps of the GA-based delay-aware ORIS element allocation are summarised in Algorithm 1.

Algorithm 1: GA-Based Delay-Aware ORIS Element Allocation

Input: Number of ORIS elements N, population size S_{p}, maximum number of generations N_{Gen}, crossover probability P_{c}, mutation probability P_{m}

Output: Best ORIS allocation vector $\mathbf{s}_{\mathrm{GA}}^{\star}$

Initialise a population $\mathscr{P}$ with S_{p} random binary allocation vectors, where $\mathbf{s}^{(p)} = [s_1^{(p)}, s_2^{(p)}, \ldots, s_N^{(p)}]$ and $s_n^{(p)} \in \{0,1\}$;

for $g = 1$ **to** N_{Gen} **do**

  for *each candidate allocation vector* $\mathbf{s}^{(p)} \in \mathscr{P}$ **do**

    Calculate the frequency-dependent channel power gain of Bob, $\mathscr{G}_{\mathrm{B}}(f)$;

    Calculate the frequency-dependent channel power gain of Eve, $\mathscr{G}_{\mathrm{E}}(f)$;

    Compute the achievable rates R_{B} and R_{E};

    Evaluate the fitness value $F(\mathbf{s}^{(p)}) = C_{\mathrm{s}}(\mathbf{s}^{(p)})$;

  Select parent allocation vectors according to their fitness values;

  Apply crossover with probability P_{c};

  Apply mutation with probability P_{m};

  Form the new population using the generated offspring and selected candidate solutions;

Select the allocation vector with the highest fitness value,

$$\mathbf{s}_{\mathrm{GA}}^{\star} = \arg \max_{\mathbf{s}^{(p)} \in \mathscr{P}} F(\mathbf{s}^{(p)}).$$

return $\mathbf{s}_{\mathrm{GA}}^{\star}$;

3.4.3 PPO-Based Allocation

For the multiple-eavesdropper scenario, the allocation problem becomes more complex because the system must account for several eavesdroppers and two different threat models. The search space also increases with the number of ORIS elements and the number of possible allocation decisions. To address this larger decision problem, the allocation design is formulated as a reinforcement learning (RL) problem. In this formulation, the ORIS controller acts as an agent, the indoor ORIS-assisted VLC system acts as the environment, and the reward is determined by the secrecy capacity obtained after an allocation decision.

PPO is used because it updates the allocation policy in a stable manner by limiting how much the policy can change during each training update. This is useful for the proposed problem because a small change in the ORIS allocation can significantly affect the channel response and secrecy capacity. The learned policy therefore provides a scalable way to select ORIS element allocations for both non-colluding and colluding eavesdropping scenarios. At each time step, the agent observes the current system state, selects an allocation action, and receives a reward based on the resulting secrecy capacity. The learning objective is to find a policy that maximises the expected secrecy reward [36].

The state at time step t is denoted by $\mathbf{o}_t$. It contains the information required by the agent to make the allocation decision, such as the current allocation status and the receiver-related channel information. The action at time step t is denoted by a_t, and it represents the allocation decision made by the agent for the ORIS elements. The policy is denoted by

$$\pi_\theta \left(a_t | \mathbf{o}_t \right), \tag{3.34}$$

where θ represents the policy parameters.

The reward is designed according to the secrecy objective. For the non-colluding eavesdropping case, the reward can be defined as

$$r_t^{\mathrm{NC}} = C_{\mathrm{s}}^{\mathrm{NC}}(\mathbf{s}_t), \tag{3.35}$$

where $\mathbf{s}_t$ is the allocation vector at time step t. For the colluding eavesdropping case, the reward is defined as

$$r_t^{\mathrm{C}} = C_{\mathrm{s}}^{\mathrm{C}}(\mathbf{s}_t). \tag{3.36}$$

Thus, the reward directly encourages the agent to select allocation decisions that improve the secrecy capacity.

The objective of the policy is to maximise the expected cumulative discounted reward,

$$J(\theta) = \mathbb{E}_{\pi_\theta}\left[\sum_{t=0}^{T} \zeta^t r_t\right], \tag{3.37}$$

where ζ is the discount factor, r_t is the reward at time step t, and T is the episode length.

In PPO, the policy is updated using a clipped surrogate objective. The probability ratio between the new and old policies is given by

$$r_t(\theta) = \frac{\pi_\theta(a_t|\mathbf{o}_t)}{\pi_{\theta_{\mathrm{old}}}(a_t|\mathbf{o}_t)}, \tag{3.38}$$

where θ_{old} denotes the policy parameters before the update.

The clipped PPO objective is expressed as

$$L^{\mathrm{CLIP}}(\theta) = \mathbb{E}_t\left[\min\left(r_t(\theta)\hat{A}_t, \mathrm{clip}\left(r_t(\theta), 1-\varepsilon, 1+\varepsilon\right)\hat{A}_t\right)\right], \tag{3.39}$$

where $\hat{A}_t$ is the estimated advantage function and ε is the clipping parameter. The clipping operation prevents the policy from changing too much during one update, which improves training stability.

In practice, the PPO agent learns the allocation policy by repeatedly interacting with the environment. For each candidate allocation, the system calculates the frequency-dependent channel power gains, achievable rates, and secrecy capacity. The reward is then used to update the policy. After training, the learned policy can select an ORIS allocation vector that improves secrecy performance for both non-colluding and colluding eavesdropping scenarios. The detailed steps of the PPO-based delay-aware ORIS element allocation are summarised in Algorithm 2.

3.5 Simulation Results and Discussion

This section presents the simulation results for the delay-aware ORIS-assisted VLC system. The objective is to evaluate how the ORIS-induced time delay can improve PLS by creating constructive ISI at Bob and destructive ISI at the eavesdroppers. The results are discussed in two stages. First, the single-eavesdropper case is considered to demonstrate the basic principle of the proposed delay-aware allocation. Then, the analysis is extended to multiple eavesdroppers, including non-colluding and colluding cases.

3.5.1 Simulation Setup

The simulations are carried out in an indoor room of dimensions $5 \times 5 \times 3$ m^3. A single LED transmitter is mounted at the centre of the ceiling, while the ORIS is installed on one side wall. Bob and the eavesdroppers are located on the receiver plane. The transmitted optical power is varied from 1 to 10 W to evaluate the secrecy performance under different received power levels.

Algorithm 2: PPO-Based Delay-Aware ORIS Element Allocation

Input: Number of ORIS elements N, number of training episodes N_{ep}, episode length T, discount factor ζ, clipping parameter ε, actor learning rate α_π, critic learning rate α_V

Output: Learned allocation policy $\pi_\theta(a_t|\mathbf{o}_t)$

Initialise the actor network with policy parameters θ;
Initialise the critic network with value parameters;
Initialise the indoor ORIS-assisted VLC environment;
for *episode* $= 1$ **to** N_{ep} **do**
    Reset the environment and initialise the ORIS allocation vector $\mathbf{s}_0$;
    for $t = 0$ **to** T **do**
        Observe the current state $\mathbf{o}_t$;
        Select an allocation action a_t according to $\pi_\theta(a_t|\mathbf{o}_t)$;
        Update the ORIS allocation vector according to a_t;
        Set the intermediate reward $r_t = 0$;
        Store $(\mathbf{o}_t, a_t, r_t, \mathbf{o}_{t+1})$ in the trajectory buffer;
    Calculate the channel frequency responses of Bob and the eavesdroppers using Equation (3.5);
    Compute the corresponding frequency-dependent SNRs and achievable rates using Equations (3.7) and (3.8);
    if *non-colluding eavesdroppers are considered* **then**
        Set the terminal reward $r_T = C_{\text{s}}^{\text{NC}}(\mathbf{s}_T)$;
    else
        Set the terminal reward $r_T = C_{\text{s}}^{\text{C}}(\mathbf{s}_T)$;
    Update the terminal reward in the trajectory buffer;
    Estimate the advantage function $\hat{A}_t$ using the collected trajectory;
    Compute the PPO probability ratio using Equation (3.38);
    Update the actor network by maximising the clipped objective in Equation (3.39);
    Update the critic network using the value loss;
    Set $\theta_{\text{old}} \leftarrow \theta$;
return $\pi_\theta(a_t|\mathbf{o}_t)$;

The main physical and algorithmic simulation settings are summarised in Table 3.1. The analysis is divided into two parts. First, the single-eavesdropper case is evaluated using the GA-based allocation framework, where one Bob and one Eve are considered under both random receiver locations and worst-case receiver placement. Then, the study is extended to the multiple-eavesdropper case using the PPO-based allocation framework, where several eavesdroppers are considered under both non-colluding and colluding behaviours, including best-case and worst-case geometries.

Moreover, these simulation settings are selected to match the indoor VLC assumptions and delay-aware ORIS-assisted models used in the two studies considered in this chapter [35], [36]. The bandwidth used in the rate calculation follows from the symbol-period setting. Following the standard indoor optical wireless channel modelling framework in [44], the considered system is dominated by the directed LoS path and the deliberately controlled ORIS-reflected paths. Higher-order diffuse reflections from the walls, ceiling, floor, and furniture experience additional propagation and reflection losses and are therefore neglected in this study. This assumption also allows the effect of the controllable ORIS-induced propagation delay on the secrecy performance to be evaluated independently of uncontrolled diffuse multipath components.

Table 3.1: Simulation parameters for the delay-aware ORIS-assisted VLC system.

Parameter	**Symbol**	**Value**
Room dimensions	–	$5 \times 5 \times 3$ m^3
LED position	–	$(2.5, 2.5, 3.0)$ m
LED half-power semi-angle	$\Phi_{1/2}$	60°
PD responsivity	R_{PD}	0.6 A/W
PD physical area	A_{PD}	1 cm^2
PD FoV	Ψ_{c}	90°
Symbol period	T_{sym}	1 ns
Modulation bandwidth	$B = 1/(2T_{\mathrm{sym}})$	500 MHz
Noise power spectral density	N_0	10^{-21} A^2/Hz
ORIS reflectivity	ρ	1
Refractive index of PD lens	n_{r}	1.5
Modulation scaling factor	κ	3.2
Gap value	Γ	2 dB
Element separation	D	30 cm
Transmit optical power	P_{t}	1–10 W
Wireless Communications Letters (WCL) single-eavesdropper GA setup		
ORIS size	N	12×12 elements
Population size	S_{p}	50
Number of generations	N_{Gen}	30
Crossover probability	P_{c}	0.8
Mutation probability	P_{m}	$1/N$
Number of random iterations	–	300
Open Journal of the Communications Society (OJCOM) multiple-eavesdropper PPO s		
ORIS position	–	Wall at $x = 0$ m
ORIS size	N	15×15 elements
Training episodes	N_{ep}	1500
Batch size	N_{batch}	64
Clipping parameter	ε	0.2
generalised advantage estimation (GAE) parameter	λ	0.95
Discount factor	ζ	0.99
Actor learning rate	α_π	1×10^{-4}
Critic learning rate	α_V	5×10^{-4}
Hidden layer dimension	d_{h}	256

Notably, the 1 ns symbol period, corresponding to a 500 MHz modulation bandwidth, is adopted as a wideband simulation setting following [78] to evaluate the effect of ORIS-induced time delay, rather than as a requirement for a specific practical optical front-end implementation.

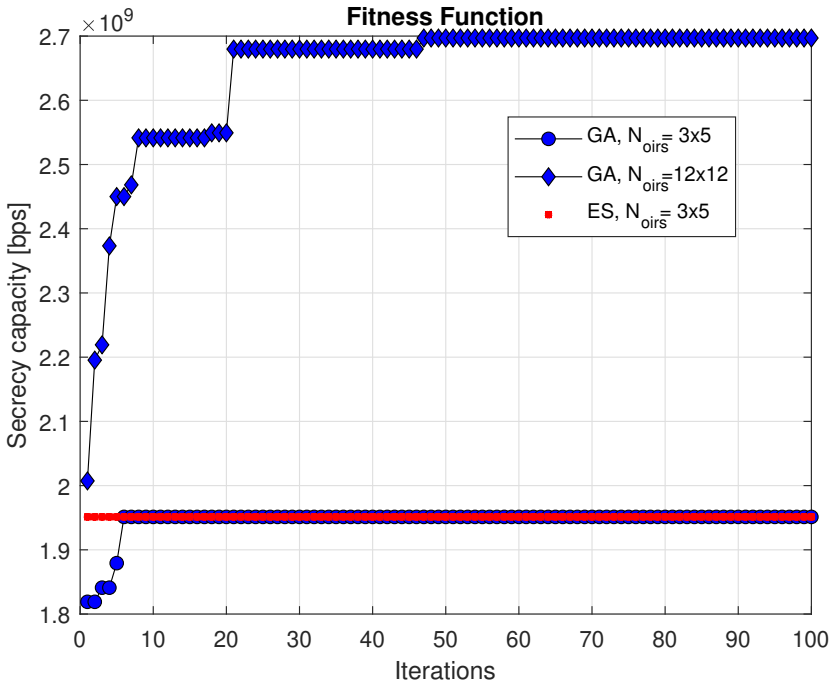


Figure 3.3: Convergence behaviour of the GA-based ORIS element allocation for different ORIS sizes.

3.5.2 Single-Eavesdropper Results

The single-eavesdropper results demonstrate the basic effect of delay-aware ORIS allocation. In this scenario, the ORIS elements are allocated using the GA described in Section 3.4.2. The objective is to identify the reflecting elements that improve Bob's channel response while degrading Eve's effective received signal through destructive ISI.

Figure 3.3 shows the convergence behaviour of the GA for different ORIS sizes. The fitness value increases rapidly during the first few iterations and then approaches a stable value. This indicates that the GA can find a good allocation vector without performing an exhaustive search over all possible ORIS element combinations. The result also shows that a larger ORIS provides a higher achievable fitness value because more reflecting elements are available for shaping the channel.

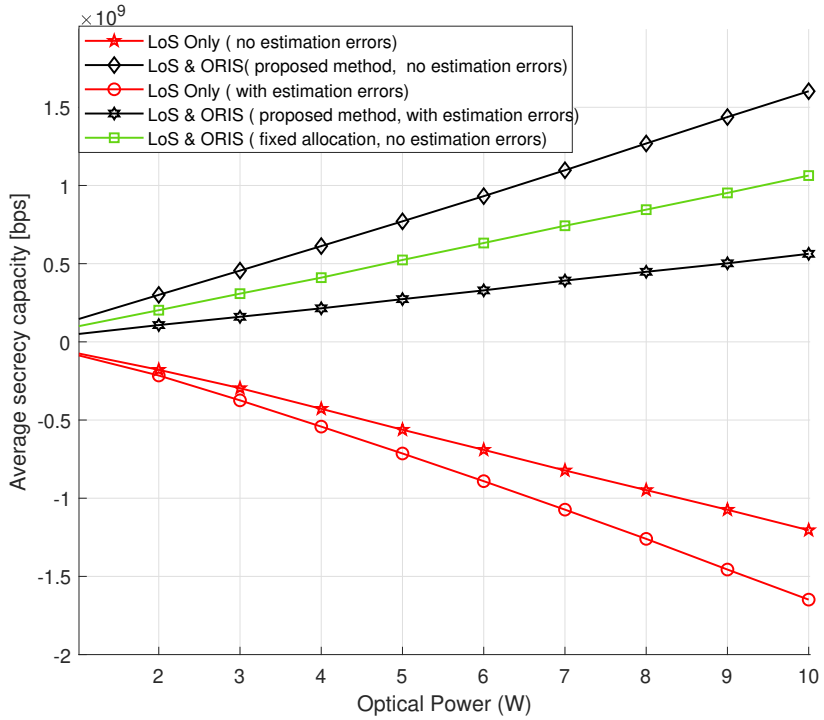


Figure 3.4: Secrecy-rate difference for the single-eavesdropper worst-case scenario, where Eve is closer to the LED than Bob.

The impact of the proposed delay-aware allocation becomes clearer in the worst-case geometry, where Eve is closer to the LED than Bob. In a conventional LoS-only system, this geometry is highly unfavourable because Eve naturally has a stronger channel. However, when the ORIS is used, selected reflected paths can increase Bob's rate while reducing Eve's effective received signal quality.

Figure 3.4 shows the secrecy capacity in this worst-case scenario. The LoS-only curve gives a negative secrecy-rate difference because Eve has a better channel than Bob. Since the achievable secrecy capacity is defined using the positive-part operator, this negative value corresponds to zero achievable secrecy capacity for the LoS-only baseline. In contrast, the LoS+ORIS case gives a positive secrecy-rate difference, showing that the proposed delay-aware allocation can overcome the unfavourable user geometry. This confirms that the ORIS-induced time delay is not merely a channel impairment but can also be used as a resource for PLS.

At an optical power of 7 W, the WCL results show that Bob's rate improves by 59.41%, while Eve's rate decreases by 12.30%. At 3 W, the plotted secrecy-rate difference changes from a negative LoS-only value to a positive value when the ORIS is used, corresponding to a 253.7% improvement. These results confirm that the proposed allocation can enhance secrecy even when the eavesdropper has a more favourable physical position than the legitimate receiver.

3.5.3 Multiple-Eavesdropper Results

The multiple-eavesdropper results evaluate the PPO-based allocation method under non-colluding and colluding eavesdropping models. In this case, the ORIS controller learns an allocation policy that maximises the secrecy reward. The results are evaluated for both best-case and worst-case geometries. The best-case geometry places Bob in a favourable location, while the worst-case geometry places the eavesdroppers closer to the LED, giving them stronger direct channels.

Figure 3.5 shows the secrecy capacity versus training episode for different ORIS sizes. The fixed all-Bob allocation gives a constant baseline because the allocation does not change during training. In contrast, the PPO-based allocation improves during training and then converges to a stable secrecy value. This behaviour shows that the PPO agent successfully learns how to allocate the ORIS elements to improve secrecy. The larger 15×15 ORIS provides better secrecy performance than the smaller 4×4 case because more reflecting elements are available for shaping the channel.

The worst-case geometry is particularly important because Bob is located near the room edge, while the eavesdroppers are closer to the LED. In this case, the eavesdroppers have stronger LoS channels than Bob, making the secrecy problem more difficult. Therefore, this scenario is useful for evaluating whether the proposed PPO-based ORIS allocation can still create a rate advantage for Bob under unfavourable receiver placement.

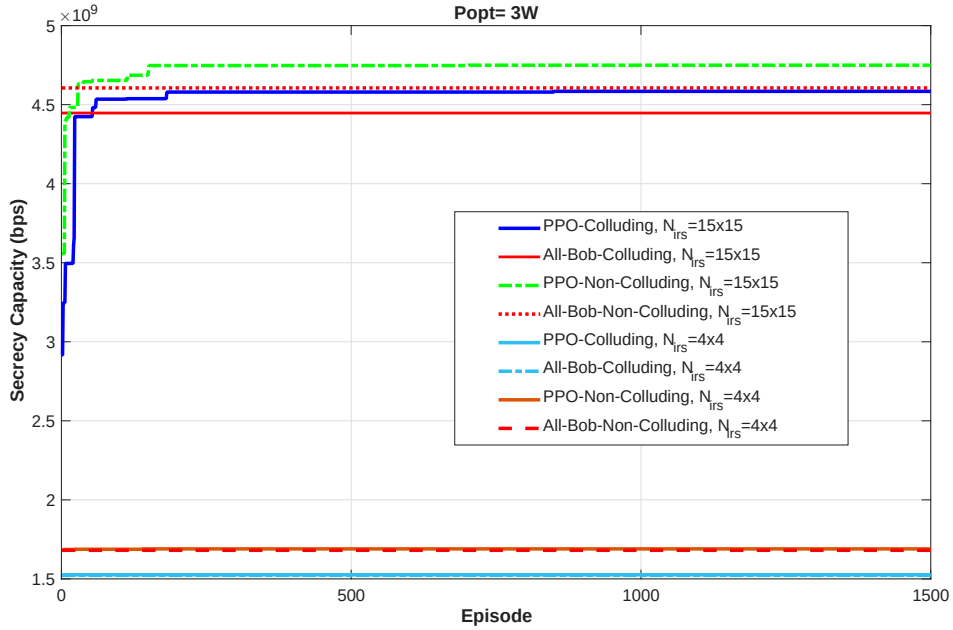


Figure 3.5: PPO training convergence for colluding and non-colluding eavesdroppers with different ORIS sizes.

Figure 3.6 shows the achievable rates in the colluding worst-case scenario. In this case, the eavesdroppers cooperate and combine their received signals, which makes the eavesdropping threat stronger than in the non-colluding case. Even under this stronger threat model, the proposed PPO-based ORIS allocation significantly improves Bob's achievable rate compared with the LoS-only case. At $P_t = 6$ W, Bob's rate increases by approximately 192.5%, while the rates of the two eavesdroppers decrease by about 4.5% and 3.0%, respectively. This shows that the learned allocation can strengthen Bob's effective channel while slightly reducing the useful received signal at the eavesdroppers.

Figure 3.7 shows the achievable rates in the non-colluding worst-case scenario. In this case, the eavesdroppers act independently, and the secrecy performance is mainly limited by the eavesdropper with the highest achievable rate. The proposed PPO-based ORIS allocation again improves Bob's rate substantially. At $P_t = 6$ W, Bob's rate increases by approximately 191%, while the rate of the dominant eavesdropper decreases by about 7%. This confirms that the delay-aware allocation remains effective even when the strongest eavesdropper has a more favourable physical location than Bob.

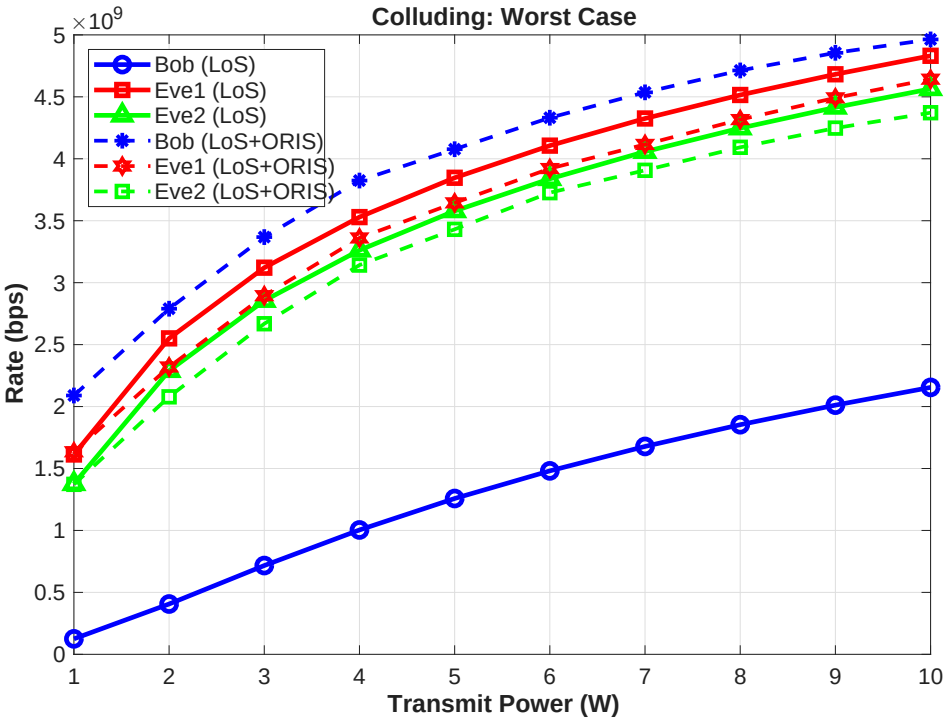


Figure 3.6: Achievable rates versus transmit optical power for the multiple-eavesdropper worst-case geometry under the colluding eavesdropping case.

Together, the colluding and non-colluding results show that the proposed PPO-based ORIS allocation can improve secrecy under different eavesdropping behaviours. The improvement is mainly achieved by exploiting the different delay profiles experienced by Bob and the eavesdroppers. In both cases, the ORIS-induced delay helps create a more favourable frequency-domain channel response for Bob, while limiting the effective received signal quality at the eavesdroppers.

Figure 3.8 validates the approximate analytical rate expression against exact numerical integration. The approximate and numerical curves closely match across the transmit power range, which confirms that the approximate expression captures the main behaviour of the delay-aware channel. This is important because it shows that the analytical approximation can explain the influence of ORIS-induced delay without requiring repeated numerical integration for every allocation pattern.

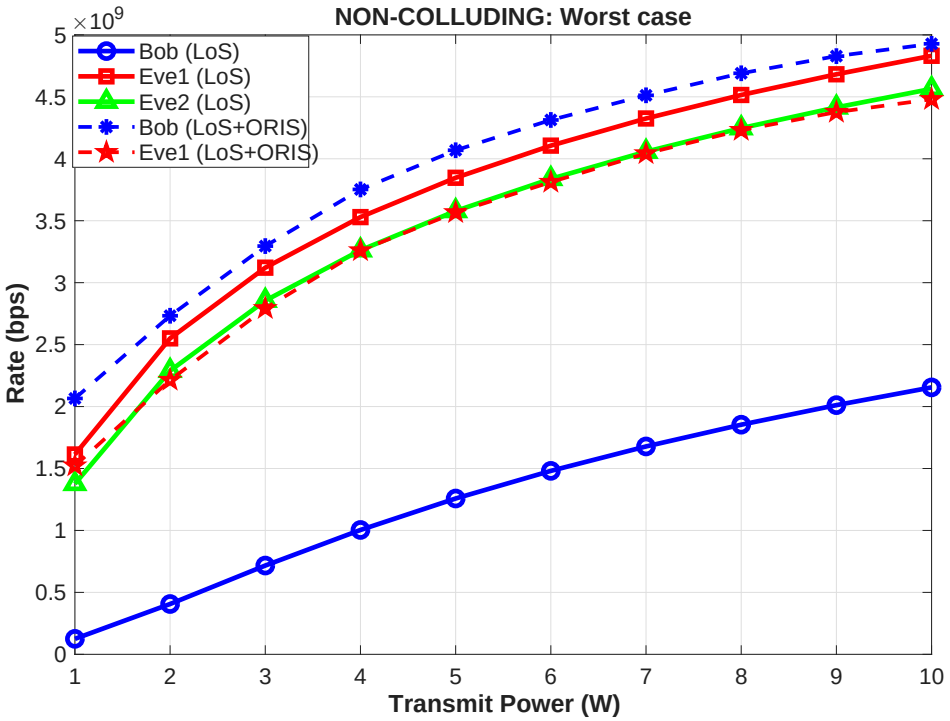


Figure 3.7: Achievable rates versus transmit optical power for the multiple-eavesdropper worst-case geometry under the non-colluding eavesdropping case.

Overall, the results demonstrate that ORIS-induced time delay can be used as a practical PLS resource in indoor VLC. In the single-eavesdropper case, GA-based allocation is sufficient to show the basic secrecy gain. In the multiple-eavesdropper case, PPO-based allocation provides a scalable solution and maintains positive secrecy capacity under both non-colluding and colluding eavesdropping models. The strongest result is observed in the worst-case geometry, where the proposed PPO-based allocation improves secrecy capacity by 107% in the colluding case and 235% in the non-colluding case compared with allocating all ORIS elements to Bob.

3.6 Summary

This chapter investigated delay-aware PLS in ORIS-assisted VLC systems. The focus was on exploiting the propagation delay introduced by ORIS-reflected optical paths, rather than considering the ORIS only as a tool for improving received optical power. A combined system and channel model was developed by considering the direct LoS link,

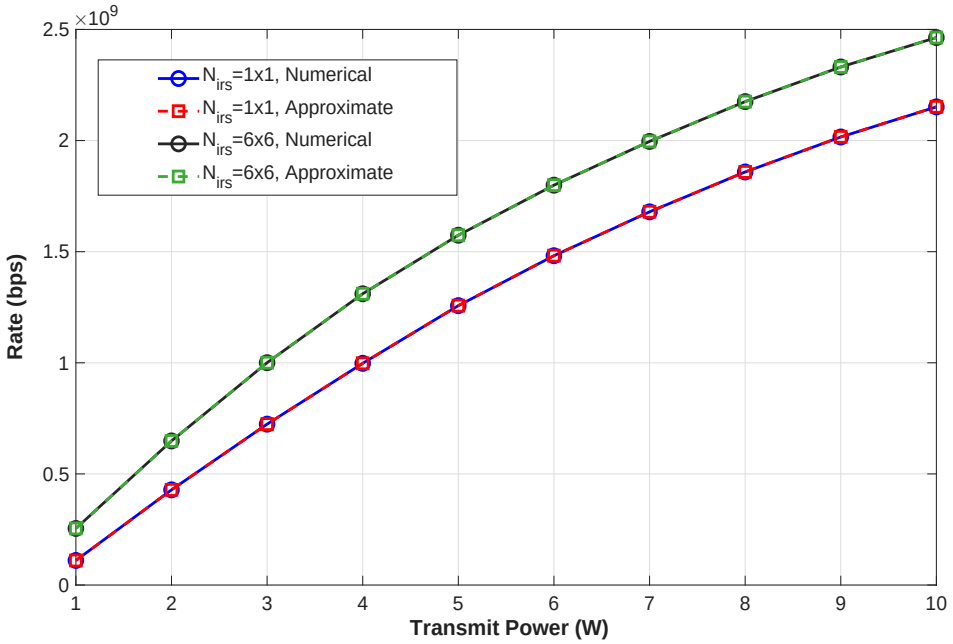


Figure 3.8: Validation of the approximate analytical rate expression against exact numerical integration.

the delayed ORIS-reflected links, and the resulting frequency-domain channel response. The secrecy performance was analysed for both single- and multiple-eavesdropper scenarios, including non-colluding and colluding cases. The delay-aware ORIS element allocation problem was then formulated and solved using GA-based allocation for the single-eavesdropper case and PPO-based allocation for the multiple-eavesdropper case. The simulation results showed that the proposed approach improves secrecy capacity even under unfavourable eavesdropper locations. Overall, this chapter demonstrated that ORIS-induced time delay can be used as an additional design resource for enhancing PLS in indoor VLC systems, and the next chapter develops non-uniform codebook design and NOMA-based resource allocation for ORIS-assisted VLC systems.

Chapter 4

Codebook Design for ORIS-Assisted VLC Systems

4.1 Introduction

This chapter moves from delay-aware secrecy analysis to practical optical beam management and multi-user resource allocation in ORIS-assisted VLC systems. Instead of revisiting the general advantages of VLC discussed in earlier chapters, the focus here is on how finite ORIS steering states can be designed and then used to support fair NOMA transmission in indoor environments.

Despite these advantages, VLC systems still face important coverage and reliability challenges. Since optical signals are highly directional and strongly dependent on the LoS path, the received optical power can decrease significantly when users move away from the main illumination region [82]. In addition, blockage, user mobility, and unfavourable receiver positions can create weak channels and uneven service quality across the receiver plane. Therefore, a single ceiling-mounted LED may not always provide reliable and uniform coverage for all users.

To address this limitation, ORIS technology has been investigated as a promising solution for reconfiguring the indoor optical wireless channel [83], [84]. By using controllable mirror elements, an ORIS can redirect incident optical beams towards desired user locations and create additional reflected paths without installing extra LED transmitters. This allows the optical propagation environment to be actively shaped, improving the RSS for users that experience weak direct LoS channels.

However, practical ORIS deployment requires accurate control of the mirror orientation. Each reflecting element is usually controlled by two angles: a tilt angle, which determines the displacement of the reflected beam footprint on the receiver plane, and a sweep angle, which determines its position along the corresponding coverage ring. If these angles are assumed to be continuously adjustable with perfect precision, the reflected beam can be ideally steered towards any target point. In practice, however, continuous real-time optimisation of the tilt and sweep angles for every user location is difficult and computationally expensive.

A practical solution is to use codebook-based beam steering, in which each ORIS element selects its steering state from a finite set of precomputed codewords. Each codeword represents a specific pair of tilt and sweep angles, and the selected codeword is the one whose reflected beam-hit point is closest to the target user location. This avoids continuous angle optimisation during real-time operation and provides a practical basis for ORIS-assisted VLC. Nevertheless, a simple uniform angular codebook does not provide uniform spatial coverage on the receiver plane, because the mapping from tilt and sweep angles to reflected hit points is nonlinear.

In particular, equal tilt steps do not produce equal radial spacing between reflected rings, and equal sweep steps do not produce equal arc lengths on rings with different radii. As a result, uniform angular sampling can create a dense concentration of codewords near the ORIS, while farther regions of the receiver plane remain sparsely covered. Moreover,

using the same codebook for all reflecting elements ignores the fact that each element has a different position on the ORIS panel and therefore a different angular-to-spatial mapping. These limitations motivate an element-wise non-uniform codebook that is designed according to the geometry of each reflecting element.

In addition to codebook design, multi-user resource allocation is also important in ORIS-assisted VLC. Once the discrete steering states are defined, the ORIS elements must be assigned to active users, and the transmit power must be allocated. NOMA is well suited to this problem because it allows multiple users to share the same optical bandwidth through power-domain multiplexing and SIC. However, the ORIS element assignment and NOMA power allocation are coupled through the effective user channels, making the joint optimisation problem difficult.

Motivated by these challenges, this chapter presents a unified framework for non-uniform codebook design and fairness-aware NOMA resource allocation in ORIS-assisted indoor VLC systems. An element-wise, geometric-optics-based non-uniform codebook is first developed and then connected to a two-stage NOMA resource-allocation method. The spatial-mapping concept was initially presented in [37], while the extended framework includes the complete codebook construction and multi-user resource-allocation design.

The main contributions of this chapter are summarised as follows:

- A geometric-optics-based codebook framework is introduced, in which each codeword represents a finite tilt-and-sweep steering state of an ORIS mirror element.
- An element-wise non-uniform codebook design is developed to provide more uniform spatial mapping on the receiver plane with fewer steering states than a uniform angular codebook.
- A codebook-based gain matrix is constructed and used to connect the offline codebook design with online multi-user NOMA resource allocation.

- A two-stage resource allocation method is presented, in which ORIS elements are first assigned using a QoS-oriented greedy strategy and the NOMA power vector is then optimised using the SSA.

The remainder of this chapter is organised as follows. Section 4.2 presents the ORIS-assisted VLC system model, including the direct and reflected optical channel models and the codebook-based steering formulation. Section 4.3 introduces the proposed non-uniform codebook design. Section 4.4 presents the NOMA-based ORIS resource allocation framework. Section 4.5 discusses the simulation results. Finally, Section 4.6 summarises the chapter.

4.2 System Model

To develop the proposed codebook and resource-allocation framework, this section considers an indoor VLC system deployed in a room of dimensions $L_x \times L_y \times L_z$ m^3. A single LED transmitter is mounted on the ceiling at position $\mathbf{L} = (x_\mathrm{L}, y_\mathrm{L}, z_\mathrm{L})$ and radiates downward according to a Lambertian emission pattern. The system serves K users located on a horizontal receiver plane at height z_u. The position of user k is denoted by $\mathbf{U}_k = (x_{\mathrm{U}_k}, y_{\mathrm{U}_k}, z_\mathrm{u})$, and each user is equipped with an upward-facing PD.

In a conventional indoor VLC system, the received signal is mainly determined by the direct LoS link between the LED and the user. However, users located far from the LED or close to the room boundary may experience weak received optical power. In addition, blockage or shadowing can further degrade the LoS link. To improve the coverage and provide additional controllable optical paths, an ORIS is mounted on one side wall of the room.

The ORIS consists of N independently controllable mirror elements. The centre of the nth reflecting element is denoted by $\mathbf{R}_n = (x_{\mathrm{R}_n}, y_{\mathrm{R}_n}, z_{\mathrm{R}_n})$. Each element is modelled as a square planar reflector with side length a and reflectivity δ. The orientation of each reflecting element is controlled through two angles: the tilt angle ϑ_n and the sweep angle φ_n. These angles determine the direction of the reflected optical beam and, consequently, the position where the reflected beam reaches the receiver plane.

Therefore, the received signal at each user contains two parts: the direct LoS component from the LED and the reflected contribution from the ORIS. The ORIS does not generate a new optical signal; instead, it redirects part of the incident LED light towards selected user locations. This makes the reflected channel strongly dependent on the room geometry, the position of each ORIS element, and the selected mirror orientation. This ORIS-assisted VLC model provides the basis for both codebook design and NOMA-based resource allocation.

4.2.1 LoS and ORIS-Assisted Channel

The channel model in this chapter is used to connect the geometric codebook design with the later NOMA resource-allocation problem. Since the standard indoor VLC LoS channel model has already been introduced in Chapter 2, the full Lambertian expression is not repeated here. Instead, the direct LoS gain between the LED and user k is denoted by $h_{\mathrm{LoS},k}$.

The reflected channel gain from the nth ORIS element to user k is modelled using GO. It is expressed as

$$h_n(\mathbf{R}_n, \mathbf{U}_k) = \frac{(m+1)A\delta}{2\pi \left(d_{1,n} + d_{2,n,k}\right)^2} \cos^m(\phi_n) \cos\left(\psi_{n,k}\right) \mathbb{I}\left(\mathbf{Q}_{n,k} \in \mathscr{L}\right), \tag{4.1}$$

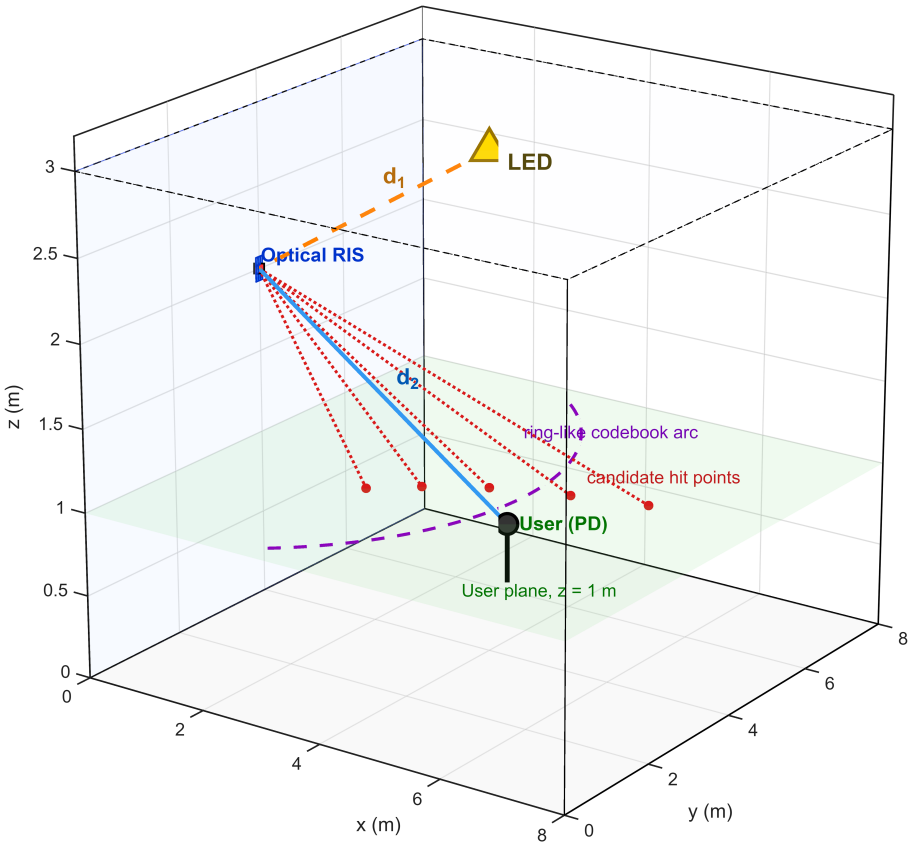


Figure 4.1: Indoor ORIS-assisted VLC system with a ceiling LED, wall-mounted ORIS, and multiple users on the receiver plane.

where $d_{1,n} = \|\mathbf{R}_n - \mathbf{L}\|_2$ is the distance from the LED to the nth ORIS element, and $d_{2,n,k} = \|\mathbf{U}_k - \mathbf{R}_n\|_2$ is the distance from the nth ORIS element to user k. The angles ϕ_n and $\psi_{n,k}$ denote the irradiance angle from the LED towards the nth element and the incidence angle at user k for the reflected path, respectively. The indicator function ensures that the reflected path is valid only when the corresponding ray geometry satisfies the required optical propagation condition.

Therefore, for the codebook-design stage, the effective optical channel gain of user k can be written as

$$h_{\text{eff},k} = h_{\text{LoS},k} + \sum_{n=1}^{N} h_n(\mathbf{R}_n, \mathbf{U}_k). \tag{4.2}$$

This compact expression shows how the direct LoS link and the ORIS-assisted reflected links jointly determine the channel available to each user. It also avoids repeating separate channel-summation equations before the resource-allocation stage. Later, when individual ORIS elements are assigned to different users, the reflected terms in (4.2) are replaced by the assignment-dependent gain matrix used for NOMA optimisation.

4.2.2 Codebook-Based ORIS Beam Steering

The reflected channel in (4.1) depends on the orientation of each ORIS mirror element. In an ideal system, the tilt and sweep angles could be continuously adjusted so that every reflected beam is perfectly aligned with the intended user location. However, continuously recomputing and configuring the exact mirror angles for every possible user position is not practical in real-time operation. Therefore, each ORIS element uses a finite offline codebook of precomputed steering states.

Let $\mathscr{C}_n$ denote the codebook of the nth ORIS element. Each codeword in $\mathscr{C}_n$ represents one feasible mirror orientation, defined by a pair of tilt and sweep angles. For a given user location, each reflecting element selects the codeword whose reflected beam-hit point is closest to the user position on the receiver plane. This converts the continuous beam-steering problem into a finite codeword selection problem.

For the nth ORIS element and user k, the selected codeword is obtained as

$$\mathbf{c}_{n,k}^{\star} = \arg\min_{\mathbf{c}\in\mathscr{C}_n} \|\mathbf{P}_n(\mathbf{c}) - \mathbf{U}_k\|_2 , \tag{4.3}$$

where $\mathbf{P}_n(\mathbf{c})$ is the beam-hit point on the receiver plane produced by element n under codeword $\mathbf{c}$. This rule selects the discrete steering state that best approximates the ideal continuous alignment towards user k.

The selected codeword determines the reflected channel gain that element n can provide to user k. Therefore, the codebook-based gain matrix is defined as

$$\mathbf{G} = \left[g_{n,k}\right]_{N\times K}, \tag{4.4}$$

where each entry is given by

$$g_{n,k} = h_n\left(\mathbf{R}_n, \mathbf{U}_k \mid \mathbf{c}^{\star}_{n,k}\right). \tag{4.5}$$

The entry $g_{n,k}$ represents the best reflected channel gain that the nth ORIS element can deliver to user k using its finite codebook.

The quality of the codebook directly affects the entries of $\mathbf{G}$. If the selected codeword places the reflected beam close to the desired user location, the reflected channel gain becomes large. If the nearest codeword is spatially far from the user, the reflected gain becomes weak. Therefore, the design of $\mathscr{C}_n$ is important because it determines how accurately the ORIS can approximate ideal beam steering with a finite number of steering states.

A simple uniform angular codebook samples the tilt and sweep angles using fixed step sizes. However, because the mapping from angular steering states to beam-hit points on the receiver plane is nonlinear, uniform angular sampling does not produce uniform spatial coverage. This limitation motivates the non-uniform element-wise codebook design introduced in the next section. This spatial-mapping concept is developed further in the following sections to support both codebook construction and NOMA-based resource allocation.

4.3 Geometric-Optics-Based Non-Uniform Codebook Design

The system model in Section 4.2 shows that the ORIS-assisted channel depends strongly on the orientation of each reflecting element. Therefore, accurate steering of the reflected optical beam is essential for improving the RSS at the users. However, continuous optimisation of the tilt and sweep angles for every user position is impractical. This section presents a geometric-optics-based non-uniform codebook design that provides practical finite steering states while maintaining uniform spatial coverage on the receiver plane.

4.3.1 Mirror Orientation and Reflected Beam Mapping

Each ORIS mirror element is controlled by two steering angles. The tilt angle ϑ controls how far the reflected beam reaches on the receiver plane, while the sweep angle φ controls the lateral direction of the reflected beam. Together, these two angles define the unit normal vector of the reflecting element as

$$\hat{\mathbf{N}}(\vartheta,\varphi) = \begin{bmatrix} \cos(\vartheta)\sin(\varphi) \\ \cos(\vartheta)\cos(\varphi) \\ -\sin(\vartheta) \end{bmatrix}. \tag{4.6}$$

Let the incident unit direction from the LED to the nth ORIS element be

$$\mathbf{d}_{\text{in},n} = \frac{\mathbf{R}_n - \mathbf{L}}{\|\mathbf{R}_n - \mathbf{L}\|_2}. \tag{4.7}$$

Using the law of specular reflection, the reflected unit direction is given by

$$\mathbf{d}_{\text{out},n} = \mathbf{d}_{\text{in},n} - 2\left(\mathbf{d}_{\text{in},n}^{\mathrm{T}}\hat{\mathbf{N}}(\vartheta,\varphi)\right)\hat{\mathbf{N}}(\vartheta,\varphi). \tag{4.8}$$

This equation shows that the reflected direction is completely determined by the incident direction and the mirror normal vector.

Once the reflected direction is obtained, the beam-hit point on the receiver plane can be found using ray tracing. For a receiver plane at height z_{u}, the hit point produced by the nth element is

$$\mathbf{P}_n(\vartheta,\varphi) = \mathbf{R}_n + t\mathbf{d}_{\mathrm{out},n}, \tag{4.9}$$

where

$$t = \frac{z_{\mathrm{u}} - z_{\mathrm{R}_n}}{d_{\mathrm{out},n,z}}. \tag{4.10}$$

Here, $d_{\mathrm{out},n,z}$ is the vertical component of $\mathbf{d}_{\mathrm{out},n}$. The condition $d_{\mathrm{out},n,z} < 0$ ensures that the reflected beam travels downward and intersects the receiver plane.

Equations (4.6)–(4.10) show that every pair of tilt and sweep angles corresponds to one spatial point on the receiver plane. Therefore, a codeword is not only an angular steering state; it also represents a physical beam-hit location. This angular-to-spatial mapping is the key principle behind the proposed codebook design. Figure 4.2 illustrates this geometric-optics relationship, showing the incident ray, the mirror normal, the reflected ray, and the resulting beam-hit point on the receiver plane.

4.3.2 Uniform Angular Codebook and Spatial Mapping Limitation

A straightforward codebook design is to sample the tilt and sweep angles uniformly using fixed step sizes. In this case, the tilt angle is sampled with a fixed step $\Delta\vartheta^{\mathrm{u}}$, while the sweep angle is sampled with a fixed step $\Delta\varphi^{\mathrm{u}}$. Although this design is simple, it does not provide uniform spatial coverage on the receiver plane.

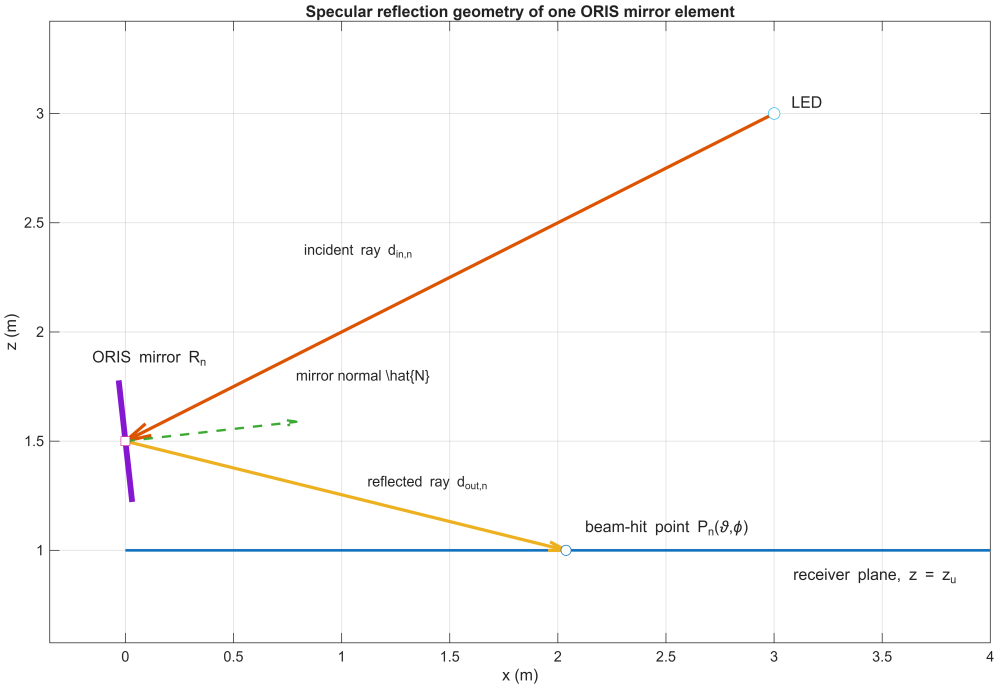


Figure 4.2: Specular reflection geometry of one ORIS mirror element, showing the incident direction, mirror normal, reflected direction, and the corresponding beam-hit point on the receiver plane.

The reason is that the mapping from the angular domain to the spatial domain is nonlinear. When the tilt angle is fixed and the sweep angle is varied continuously, the reflected beam traces a circular arc on the receiver plane. This arc is referred to as a ring. When the tilt angle changes, multiple rings with different radii are generated. Figure 4.3 illustrates that different tilt states produce different beam-hit distances on the receiver plane, whereas Figure 4.4 shows that changing the sweep angle moves the beam-hit point laterally along the same ring.

The radius of each ring is related to the tilt angle through

$$r_i \propto \tan\left(\beta_n + 2\vartheta_{n,i}\right), \tag{4.11}$$

where β_n is a geometry-dependent angle defined as

$$\beta_n = \arccos\left(\mathbf{e}_3^{\mathrm{T}}\mathbf{d}_{\mathrm{in},n}\right), \tag{4.12}$$

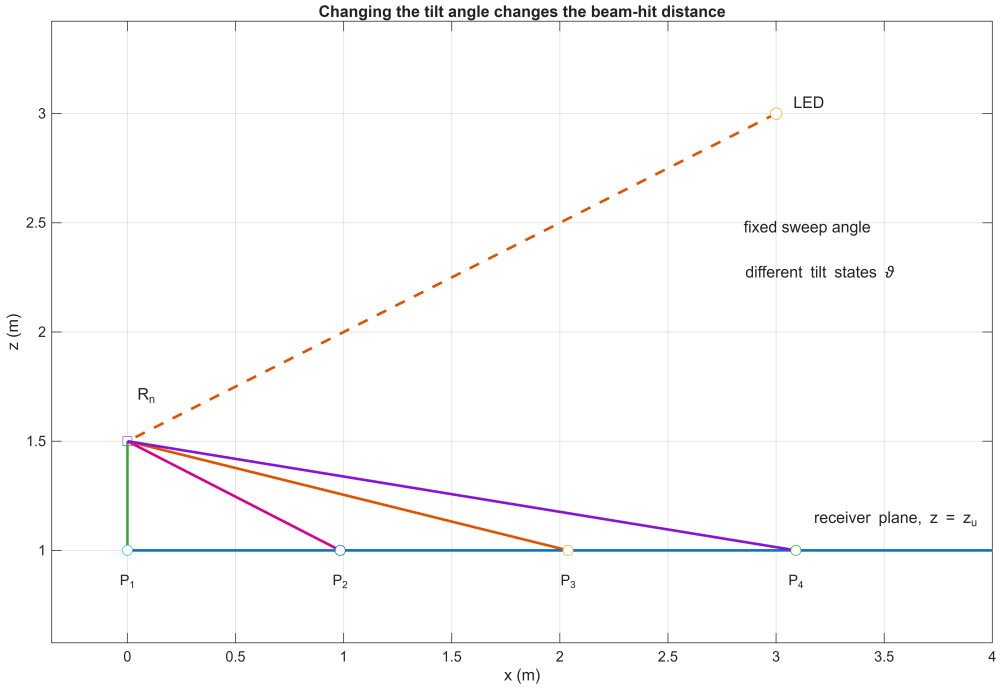


Figure 4.3: Illustration of the tilt-angle effect on the reflected beam-hit position. For a fixed sweep angle, different tilt states produce different beam-hit distances on the receiver plane.

and $\mathbf{e}_3 = (0,0,1)^{\mathrm{T}}$ is the vertical unit vector.

The factor of two in (4.11) comes from the law of reflection, because rotating the mirror by ϑ rotates the reflected beam by approximately 2ϑ. Therefore, equal tilt steps do not produce equal radial spacing between rings. Similarly, equal sweep steps do not produce equal arc lengths on all rings, because the arc length increases with the ring radius.

As a result, a uniform angular codebook can produce many redundant codewords near the ORIS, while leaving the farther region of the receiver plane sparsely covered. This means that the codebook may have many steering states but still provide poor spatial mapping in some regions. The comparison between uniform and non-uniform spatial mapping shows that uniform angular sampling creates dense points near the ORIS and sparse points farther away, whereas the proposed non-uniform design provides more balanced coverage across the receiver plane.

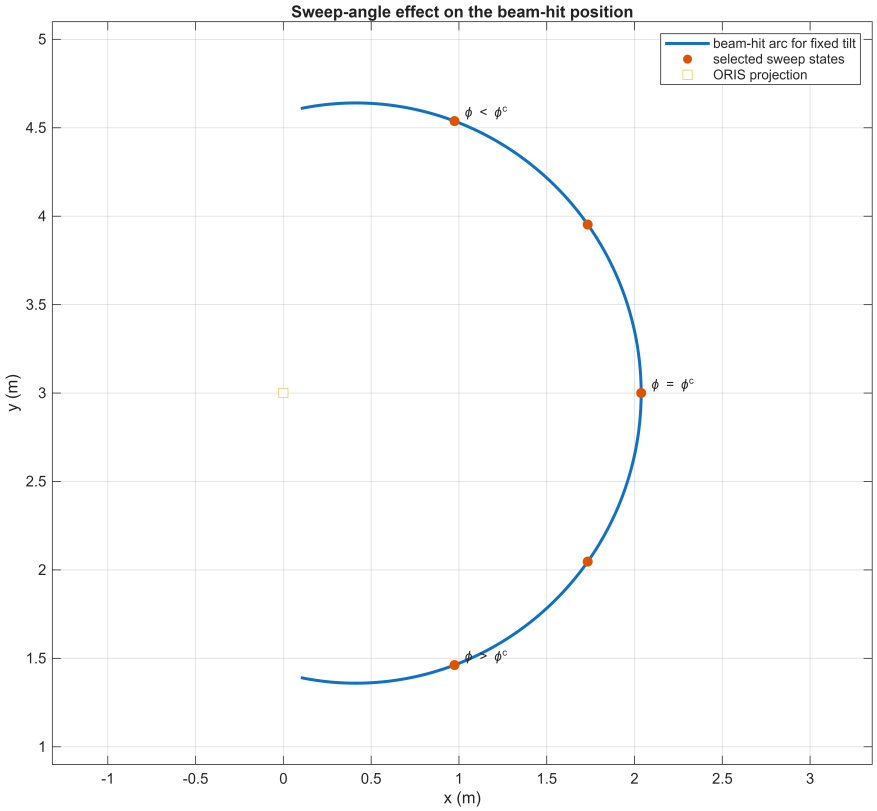


Figure 4.4: Illustration of the sweep-angle effect on the reflected beam-hit position. For a fixed tilt angle, changing the sweep angle moves the beam-hit point along the same receiver-plane ring.

4.3.3 Element-Wise Non-Uniform Codebook Design

The proposed codebook is designed separately for each ORIS element. This is important because each reflecting element has a different position on the ORIS panel. Therefore, the incident direction, reference sweep angle, and angular-to-spatial mapping are different for different elements. A single common codebook cannot accurately represent all elements, especially when the ORIS has many reflecting mirrors.

The construction begins by computing the reference sweep angle of the nth element as

$$\varphi_n^{\mathrm{c}} = \arctan 2\left(\mathbf{e}_2^{\mathrm{T}}\mathbf{d}_{\mathrm{in},n}, \mathbf{e}_1^{\mathrm{T}}\mathbf{d}_{\mathrm{in},n}\right), \tag{4.13}$$

where $\mathbf{e}_1$ and $\mathbf{e}_2$ are the unit vectors along the x- and y-axes, respectively. This reference angle identifies the central sweep direction for the nth mirror element. As illustrated earlier in Figure 4.4, the sweep angle determines the position of the reflected beam along a ring on the receiver plane.

The first tilt codeword is selected so that the reflected beam points vertically downward towards the point directly below the nth element on the receiver plane. It is given by

$$\vartheta_{n,1} = -\arccos\left(\frac{\left(\mathbf{d}_{\text{in},n}+\mathbf{e}_3\right)^{\mathrm{T}}\hat{\mathbf{N}}(0,\varphi_n^{\text{c}})}{\left\|\mathbf{d}_{\text{in},n}+\mathbf{e}_3\right\|_2}\right). \tag{4.14}$$

This first codeword anchors the codebook to the geometry of the individual element. In geometric terms, it corresponds to the first ring location directly associated with the selected mirror element, consistent with the tilt-dependent mapping shown in Figure 4.3.

The second tilt codeword is initialised as

$$\vartheta_{n,2} = \vartheta_{n,1} - \Delta\vartheta, \tag{4.15}$$

where $\Delta\vartheta$ is the initial tilt design step. The remaining tilt codewords are then generated by enforcing equal radial spacing on the receiver plane. This is achieved by requiring the transformed quantities $\tan(\beta_n + 2\vartheta_{n,i})$ to form an arithmetic progression,

$$\tan(\beta_n+2\vartheta_{n,i+1}) + \tan(\beta_n+2\vartheta_{n,i-1}) = 2\tan(\beta_n+2\vartheta_{n,i}). \tag{4.16}$$

Solving this condition gives the next tilt codeword as

$$\vartheta_{n,i+1} = \frac{1}{2}\left[\arctan\left(2\tan(\beta_n+2\vartheta_{n,i}) - \tan(\beta_n+2\vartheta_{n,i-1})\right) - \beta_n\right]. \tag{4.17}$$

Although these tilt angles are not uniformly spaced in the angular domain, their corresponding ring radii are more uniformly spaced on the receiver plane. This is the main reason for using a non-uniform tilt design.

For each ring i, the sweep codewords are generated around the reference sweep angle. To maintain approximately equal arc length between neighbouring codewords, the sweep step is reduced as the ring index increases:

$$\varphi_{n,i,\ell} = \varphi_n^{\mathrm{c}} \pm \ell \frac{\Delta\varphi}{i}, \qquad \ell = 1,2,3,\ldots. \tag{4.18}$$

The sweep generation continues until the resulting angle falls outside the feasible sweep range. Since outer rings have larger radii, they require more sweep points to preserve similar spatial spacing. The factor $1/i$ in (4.18) provides this behaviour.

Therefore, the complete codebook of the nth element is constructed as

$$\mathscr{C}_n = \left\{ \left(\vartheta_{n,i}, \varphi_{n,i,\ell} \right) \right\}, \tag{4.19}$$

where each pair defines one feasible tilt-and-sweep steering state. Because the construction is performed separately for every reflecting element, the resulting codebook captures the element-dependent geometry of the ORIS array.

The complete non-uniform codebook construction is summarised in Algorithm 3. The algorithm first computes the incident direction, the reference sweep angle, and the first tilt codeword for the selected element. It then generates the remaining tilt levels using the equal radial spacing condition and assigns sweep codewords to each ring using the equal arc-length rule.

4.3.4 Codebook Error Metric

To evaluate the accuracy of the proposed codebook, the codebook-based steering is compared with ideal continuous steering. Under ideal continuous steering, each ORIS element can perfectly align the reflected beam towards the desired user position. Under codebook-based steering, the element selects the nearest available codeword, which may produce a small spatial mismatch.

Algorithm 3: Element-Wise GO-Based Non-Uniform ORIS Codebook Generation

Input: Element position $\mathbf{R}_n$, LED position $\mathbf{L}$, design parameters $\Delta\vartheta$ and $\Delta\varphi$
Output: Codebook $\mathscr{C}_n$
Compute the incident direction $\mathbf{d}_{\text{in},n}$ using (4.7);
Compute β_n using (4.12);
Compute the reference sweep angle φ_n^{c} using (4.13);
Compute the first tilt codeword $\vartheta_{n,1}$ using (4.14);
Initialise $\vartheta_{n,2} = \vartheta_{n,1} - \Delta\vartheta$;
Initialise $\mathscr{C}_n = \emptyset$ and set $i = 1$;
while *the reflected beam-hit points remain inside the receiver plane* **do**
    Generate sweep angles $\varphi_{n,i,\ell}$ using (4.18);
    Add all valid pairs $(\vartheta_{n,i}, \varphi_{n,i,\ell})$ to $\mathscr{C}_n$;
    Compute the next tilt angle $\vartheta_{n,i+1}$ using (4.17);
    Set $i \leftarrow i+1$;
return $\mathscr{C}_n$;

The mismatch is measured using the Frobenius norm of the channel error matrix. It is defined as

$$\|\Delta\mathbf{H}\|_{\text{F}} = \sqrt{\sum_{n=1}^{N}\sum_{k}\left(h_{\text{ideal},n}(\mathbf{U}_k) - h_{\text{cb},n}(\mathbf{U}_k)\right)^2}, \tag{4.20}$$

where $h_{\text{ideal},n}(\mathbf{U}_k)$ is the reflected channel gain achieved by element n under ideal continuous steering, and $h_{\text{cb},n}(\mathbf{U}_k)$ is the channel gain achieved using the selected codeword from the finite codebook.

A smaller value of $\|\Delta\mathbf{H}\|_{\text{F}}$ means that the discrete codebook closely approximates ideal beam steering over the receiver plane. This is important because better codebook accuracy leads to stronger entries in the gain matrix $\mathbf{G}$, which directly improves the effective channels used for NOMA resource allocation. Therefore, the codebook design is not only a beam-steering problem; it also forms the foundation for the multi-user resource allocation developed in the next section.

4.4 NOMA-Based ORIS Resource Allocation

The non-uniform codebook developed in Section 4.3 provides a finite set of practical steering states for each ORIS element. After the codebook is constructed, the best reflected channel gain that each element can provide to each user is stored in the gain matrix **G**. Therefore, the online optimisation no longer needs to continuously search over mirror angles. Instead, the remaining task is to assign the available ORIS elements among users and allocate the NOMA transmit powers over the resulting effective channels.

4.4.1 Effective Channel and NOMA Signal Model

Let $s_{n,k}$ be a binary assignment variable, for which $s_{n,k} = 1$ means that the nth ORIS element is assigned to user k, and $s_{n,k} = 0$ otherwise. Since each flat mirror element can steer its reflected beam towards only one user during a transmission interval, each element can be assigned to one user only. This gives the assignment constraint

$$\sum_{k=1}^{K} s_{n,k} = 1, \qquad \forall n \in \{1,2,\ldots,N\}. \tag{4.21}$$

For a given assignment matrix **S**, the effective channel gain of user k is obtained by combining the direct LoS channel and the reflected contributions from the ORIS elements assigned to that user:

$$\tilde{h}_k = h_{\mathrm{LoS},k} + \sum_{n=1}^{N} s_{n,k} g_{n,k}. \tag{4.22}$$

This expression connects the offline codebook design with the online NOMA resource allocation. A better codebook produces larger values of $g_{n,k}$, which can improve the effective channels and increase the achievable user rates.

After the effective channels are obtained, the users are sorted from the weakest to the strongest channel as

$$\tilde{h}_1 \leq \tilde{h}_2 \leq \cdots \leq \tilde{h}_K. \tag{4.23}$$

Accordingly, the NOMA power allocation follows the reverse order,

$$p_1 \geq p_2 \geq \cdots \geq p_K \geq 0, \tag{4.24}$$

so that users with weaker effective channels receive larger transmit powers.

Under perfect SIC, user k treats the signals intended for stronger-channel users as interference when decoding its own signal. Therefore, the SINR of user k is written as

$$\gamma_k = \frac{\tilde{h}_k^2 p_k}{\tilde{h}_k^2 \sum_{\ell=k+1}^{K} p_\ell + \sigma_w^2}, \qquad k = 1,2,\ldots,K. \tag{4.25}$$

The achievable spectral efficiency of user k is then

$$R_k = \log_2(1+\gamma_k), \tag{4.26}$$

and the system sum rate is

$$R_{\text{sum}} = \sum_{k=1}^{K} R_k. \tag{4.27}$$

Since the sum rate alone does not describe how fairly the throughput is distributed among users, Jain's fairness index is also considered. It is defined as

$$J(\mathbf{R}) = \frac{\left(\sum_{k=1}^{K} R_k\right)^2}{K \sum_{k=1}^{K} R_k^2}, \tag{4.28}$$

where $\mathbf{R} = [R_1, R_2, \ldots, R_K]^{\mathrm{T}}$. A value close to one indicates that the user rates are well balanced, while a smaller value indicates a larger rate imbalance. This fairness metric is important because an ORIS-assisted system should not only increase the total throughput, but should also improve the service quality of users with weak channels.

4.4.2 Fairness-Aware Optimisation Problem

The objective of the resource allocation is to jointly assign the ORIS elements and allocate the NOMA transmit powers. A direct sum-rate maximisation may favour users with strong effective channels and leave weak users with low rates. On the other hand, maximising fairness alone may reduce the total throughput. To balance these two objectives, a logarithmic utility function is used. This utility rewards higher rates while strongly penalising small individual rates.

The joint ORIS assignment and NOMA power allocation problem is formulated as

$$
\begin{aligned}
\mathbf{P}: \quad \max_{\mathbf{S},\mathbf{p}} \quad & \sum_{k=1}^{K} \log_2 (R_k) \\
\text{s.t.} \quad & R_k \geq R_{\min}, \qquad \forall k, \\
& \sum_{k=1}^{K} s_{n,k} = 1, \qquad \forall n, \\
& s_{n,k} \in \{0,1\}, \qquad \forall n,k, \\
& \sum_{k=1}^{K} p_k \leq P_{\max}, \\
& \sum_{k=1}^{K} \sqrt{p_k} \leq C_{\mathrm{p}}, \\
& p_1 \geq p_2 \geq \cdots \geq p_K \geq 0.
\end{aligned}
\tag{4.29}
$$

Here, $R_{\min}$ is the minimum required rate for each user, $P_{\max}$ is the maximum transmit power, and C_{p} is the peak-intensity limit of the VLC signal.

The first constraint guarantees a minimum QoS for every user. The second and third constraints ensure that each ORIS element is assigned to exactly one user. The fourth constraint limits the total transmit power, while the fifth constraint represents the optical peak-intensity constraint. The last constraint enforces the NOMA power ordering according to the effective channel ordering.

Problem (4.29) is a mixed-integer non-convex optimisation problem. The binary assignment variables and the continuous power variables are coupled through the effective channels and user rates. Therefore, an exhaustive joint search becomes computationally impractical for realistic ORIS sizes. To reduce the complexity, a two-stage solution is adopted. First, the ORIS elements are assigned to users using a QoS-oriented greedy strategy. Then, after the assignment is fixed, the NOMA power vector is optimised using the SSA, while GRPA is used as a benchmark.

4.4.3 QoS-Oriented ORIS Element Allocation

The ORIS element allocation is performed before the final NOMA power optimisation. During this stage, temporary equal power allocation is used for all users to avoid favouring any specific power allocation method. The resulting effective channels and rates provide an initial view of which users need reflected assistance from the ORIS.

The allocation process has two stages. In the first stage, the algorithm checks whether any user fails to satisfy the minimum rate requirement. If such users exist, the user with the largest rate deficit is selected as

$$k^{\star} = \arg \max_{k:R_k<R_{\min}} (R_{\min} - R_k). \tag{4.30}$$

This step gives priority to the user that is farthest below the required rate.

After selecting the user with the largest deficit, the algorithm assigns to this user the unallocated ORIS element that provides the largest reflected gain:

$$n^{\star} = \arg \max_{n \in \mathscr{U}} g_{n,k^{\star}}, \tag{4.31}$$

where $\mathscr{U}$ is the set of currently unassigned ORIS elements. After each assignment, the effective channels and user rates are updated. This process continues until all users satisfy the minimum rate requirement or no unassigned elements remain.

Once the minimum rate requirement is satisfied for all users, the remaining ORIS elements are used to improve the logarithmic utility. For each remaining element and each possible user, the algorithm evaluates the resulting utility and selects the element-user pair that provides the largest improvement:

$$(n^\star, k^\star) = \arg \max_{n \in \mathscr{U}, k} \sum_{j=1}^{K} \log_2 \left(R_j^{(n,k)} \right), \tag{4.32}$$

where $R_j^{(n,k)}$ is the rate of user j after the trial assignment of element n to user k. Therefore, the first stage of allocation protects users with weak rates, while the second stage improves the overall logarithmic utility.

This QoS-oriented allocation strategy naturally concentrates reflected optical energy on users that need it most. As a result, the effective channel distribution becomes more balanced before power optimisation begins. This is important because the subsequent NOMA power allocation can perform better when the channel imbalance among users is reduced.

4.4.4 GRPA and SSA Power Allocation

After the ORIS assignment is fixed, the same effective channels are used for both the GRPA benchmark and the proposed SSA-based power allocation. This provides a fair comparison because the difference between the methods comes only from the way the NOMA power vector is selected.

The GRPA method is a low-complexity benchmark. It allocates power according to the effective channel ratios after the users are sorted as in (4.23). The unnormalised power coefficient is initialised as

$$\xi_1 = 1, \tag{4.33}$$

and for $k \geq 2$, it is updated recursively as

$$\xi_k = \left(\frac{\tilde{h}_1}{\tilde{h}_k}\right)^k \xi_{k-1}. \tag{4.34}$$

The final GRPA power allocation is then obtained by normalising the unnormalised powers:

$$p_k^{\mathrm{GRPA}} = \frac{\xi_k}{\sum_{j=1}^{K} \xi_j} P_{\max}. \tag{4.35}$$

Although GRPA is simple, it follows a fixed rule and does not directly optimise the logarithmic utility in (4.29). Therefore, it is used as a practical benchmark for comparison.

The proposed method uses the SSA to optimise the NOMA power vector after the ORIS assignment is fixed. Unlike the GA used in Chapter 3 for binary ORIS element allocation, the power-allocation stage in this chapter is a continuous constrained optimisation problem. SSA is therefore adopted because it can directly search over continuous candidate power vectors while balancing exploration and exploitation through producer, follower, and warning behaviours. This makes it suitable for improving the logarithmic utility under the NOMA power-ordering, total-power, peak-intensity, and minimum-rate constraints. In SSA, each sparrow represents one candidate power vector,

$$\mathbf{x}_i = [p_{i,1}, p_{i,2}, \ldots, p_{i,K}]. \tag{4.36}$$

For each candidate, the rates are computed using (4.25) and (4.26). The fitness value is defined as

$$F(\mathbf{x}_i) = \begin{cases} \displaystyle\sum_{k=1}^{K} \log_2\left(R_k(\mathbf{x}_i)\right), & \mathbf{x}_i \in \mathscr{F}, \\ -\infty, & \mathbf{x}_i \notin \mathscr{F}, \end{cases} \tag{4.37}$$

where $\mathscr{F}$ is the feasible set defined by the rate, power, peak-intensity, and ordering constraints in (4.29). Assigning $-\infty$ to infeasible candidates ensures that infeasible power vectors are never selected as the final solution.

During the search process, the SSA population is divided into producers, followers, and warning sparrows. Producers explore promising regions of the feasible power-allocation space, followers move towards better candidate solutions, and warning sparrows help the population avoid poor regions. After each update, candidate power vectors are repaired if needed, checked against the constraints, and then re-evaluated using the fitness function.

After the final iteration, the best feasible candidate is selected as

$$\mathbf{p}_{\mathrm{SSA}}^{\star} = \arg\max_{\mathbf{p}\in\mathscr{F}} \sum_{k=1}^{K} \log_2\left(R_k\right). \tag{4.38}$$

This SSA-based optimisation searches the feasible power space directly according to the logarithmic utility, which allows it to provide a better throughput–fairness trade-off than the fixed GRPA rule.

The complete two-stage ORIS-assisted NOMA resource allocation method is summarised in Algorithm 4. The algorithm first constructs the assignment matrix using the QoS-oriented element allocation strategy, and then computes both the GRPA benchmark power vector and the proposed SSA-optimised power vector.

4.5 Simulation Results and Discussion

This section presents the simulation results for the proposed non-uniform codebook design and the ORIS-assisted NOMA-VLC resource allocation framework. The evaluation first examines the codebook accuracy and spatial mapping behaviour, and then studies the effect of the resulting ORIS-assisted channel on multi-user NOMA performance. This order is important because the quality of the codebook directly determines the reflected gain matrix used in the resource allocation stage.

Algorithm 4: ORIS-Assisted NOMA Resource Allocation with GRPA and SSA

Input: Gain matrix $\mathbf{G}$, direct channels $\{h_{\mathrm{LoS},k}\}_{k=1}^{K}$, maximum power $P_{\max}$, minimum rate $R_{\min}$, noise variance σ_w^2
Output: Assignment matrix $\mathbf{S}$, GRPA power vector $\mathbf{p}^{\mathrm{GRPA}}$, SSA power vector $\mathbf{p}^{\star}_{\mathrm{SSA}}$
Initialise $\mathbf{S} = \mathbf{0}_{N\times K}$ and $\mathscr{U} = \{1,2,\ldots,N\}$;
Apply temporary equal power allocation and compute the initial user rates;
while $\mathscr{U} \neq \emptyset$ **do**
  if *there exists a user with* $R_k < R_{\min}$ **then**
    Select $k^{\star}$ using (4.30);
    Select $n^{\star}$ using (4.31);
  else
    Select $(n^{\star},k^{\star})$ using (4.32);
  Set $s_{n^{\star},k^{\star}} = 1$;
  Remove $n^{\star}$ from $\mathscr{U}$;
  Update $\tilde{h}_k$ and R_k for all users;
Sort users such that $\tilde{h}_1 \leq \tilde{h}_2 \leq \cdots \leq \tilde{h}_K$;
Compute $\mathbf{p}^{\mathrm{GRPA}}$ using (4.33)–(4.35);
Compute the GRPA user rates, sum rate and Jain fairness index;
Apply SSA using (4.37) to obtain $\mathbf{p}^{\star}_{\mathrm{SSA}}$;
Compute the SSA user rates, sum rate and Jain fairness index;
return $\mathbf{S}$, $\mathbf{p}^{\mathrm{GRPA}}$, $\mathbf{p}^{\star}_{\mathrm{SSA}}$;

4.5.1 Simulation Setup

The simulations consider an indoor room with a ceiling-mounted LED transmitter and a wall-mounted ORIS. Users are randomly distributed on the receiver plane, and the performance is averaged over independent user realisations. The main numerical setup uses a room of dimensions $6\times 6\times 3$ m^3, in which the ORIS is deployed on one side wall and contains up to 15×15 reflecting elements. The ORIS codebook is first evaluated using the Frobenius norm error, and then the resulting gain matrix is used in the NOMA resource allocation problem.

Four schemes are compared in the NOMA performance evaluation. The first two are LoS-only baselines with GRPA and SSA power allocation, respectively. The other two are LoS+ORIS schemes with GRPA and SSA. This comparison separates the gain achieved by the ORIS from the gain achieved by the proposed SSA-based power optimisation. The performance is evaluated using the sum rate and Jain fairness index.

Table 4.1: Simulation parameters for the ORIS-assisted NOMA-VLC system.

Parameter	**Value**
Room dimensions	$6 \times 6 \times 3$ m^3
LED position	$(3,3,3)$ m
ORIS centre position	$(0,3,1.5)$ m
Mirror spacing	0.1 m
Mirror reflectivity	$\delta = 1$
Receiver plane height	$z_{\mathrm{u}} = 1$ m
Lambertian order	$m = 1$
Half-power angle	60°
FoV	$\Psi_{\mathrm{c}} = 70^\circ$
Photodetector area	$A = 10^{-4}$ m^2
Photodetector responsivity	$R_{\mathrm{PD}} = 0.45$ A/W
Noise variance	$\sigma_w^2 = 2 \times 10^{-14}$ A^2
Maximum transmit power	$P_{\max} = 12$ mW
ORIS elements	225 elements
Minimum rate	$R_{\min} = 0.05$ bps/Hz
SSA population size	80 candidates
SSA maximum iterations	35 iterations
Monte Carlo runs	10^4 realisations

The numerical settings are chosen to match the objective of this chapter, namely the evaluation of finite ORIS codebook design and multi-user NOMA resource allocation in an indoor VLC environment. Unlike Chapter 3, where the main focus is delay-aware secrecy analysis, this chapter uses a multi-user ORIS-assisted VLC setup to compare the effect of codebook-based reflected links and power-allocation strategies. Therefore, the room geometry, receiver-plane height, ORIS aperture, optical front-end parameters, and power constraints are selected to provide a consistent indoor benchmark for comparing LoS-only, LoS+ORIS, GRPA, and SSA-based schemes.

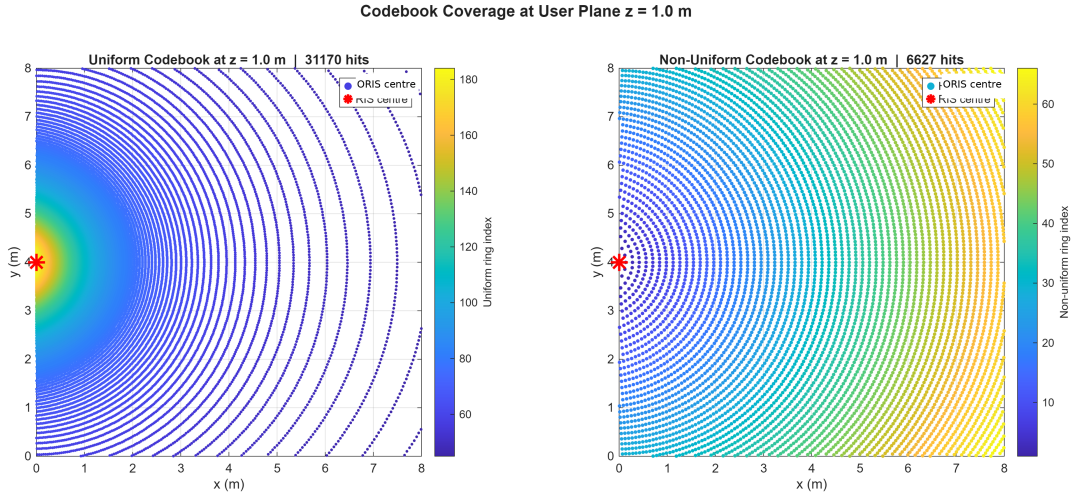


Figure 4.5: Spatial mapping comparison between uniform and non-uniform codebooks on the receiver plane.

4.5.2 Uniform and Non-Uniform Codebook Comparison

Before evaluating the NOMA performance, it is important to first examine why a non-uniform codebook is needed. A uniform angular codebook samples the tilt and sweep angles with fixed step sizes. Although this is simple, it does not produce uniform spatial coverage on the receiver plane because the angular-to-spatial mapping of the reflected beam is nonlinear. Therefore, many reflected points are concentrated near the ORIS, while far regions of the receiver plane are covered more sparsely.

Figure 4.5 compares the spatial mapping of the uniform and non-uniform codebooks on the receiver plane. The uniform codebook produces dense reflection points near the ORIS and visible gaps farther away. In contrast, the proposed non-uniform codebook adapts the angular steps to provide more balanced spatial coverage. This comparison is included at the beginning of the results section because it directly shows how the proposed codebook changes the spatial distribution of reflected beam-hit points before the resulting gain matrix is used for NOMA resource allocation.

The key observation from this comparison is that uniform angular resolution does not mean uniform spatial resolution. Since users are distributed on the receiver plane, the codebook should be designed according to spatial coverage rather than angular spacing alone. The proposed non-uniform codebook achieves this by using equal radial ring spacing and approximately equal arc length per codeword, which reduces spatial redundancy and improves coverage efficiency.

4.5.3 Codebook Error Performance

The accuracy of the proposed codebook is evaluated using the Frobenius norm error $\|\Delta\mathbf{H}\|_{\mathrm{F}}$. This metric measures the mismatch between ideal continuous steering and finite codebook-based steering. A smaller value indicates that the selected codewords approximate the ideal beam alignment more accurately.

Figure 4.6 shows the Frobenius norm error as a function of the tilt step $\Delta\vartheta$ for different sweep-step values. The error increases when $\Delta\vartheta$ becomes larger because wider tilt spacing creates larger radial gaps between neighbouring rings on the receiver plane. For a fixed tilt step, the error is also higher when the sweep step $\Delta\varphi$ increases. This shows that both tilt and sweep resolutions affect the final codebook accuracy.

Figure 4.7 shows the complementary result, in which $\|\Delta\mathbf{H}\|_{\mathrm{F}}$ is plotted against the sweep step $\Delta\varphi$ for different tilt-step values. In this case, the error increases more noticeably as $\Delta\varphi$ becomes larger. This is because the sweep angle controls the arc-wise spacing between codewords on each ring. A larger sweep step increases the separation between neighbouring hit points, especially on outer rings where the arc length is larger. Therefore, the sweep resolution has a stronger effect on the codebook error than the tilt resolution over the considered range.

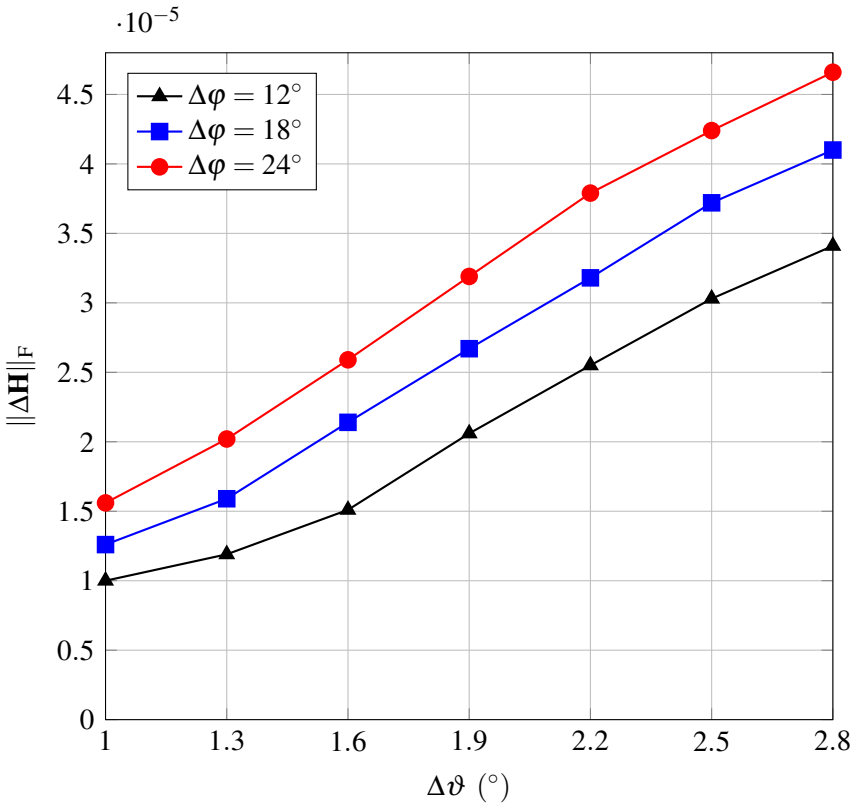


Figure 4.6: Frobenius norm error versus tilt step for different sweep-step values.

Figure 4.8 shows the number of candidate beams as a function of the coverage radius. As the receiver coverage radius increases, more candidate beams are required to cover the larger spatial region. For the same coverage radius, a smaller tilt step generates more candidate beams because it creates more radial rings. Therefore, there is a clear trade-off between codebook accuracy and codebook size. A finer codebook improves spatial alignment but increases the number of steering states that must be stored and searched.

Together, these results show that the proposed codebook can provide accurate spatial steering with a finite number of codewords. They also show that the sweep step should be chosen carefully because it has a strong effect on the spatial mismatch. This codebook evaluation is important because the resulting gain matrix is later used by the ORIS-assisted NOMA resource allocation algorithm.

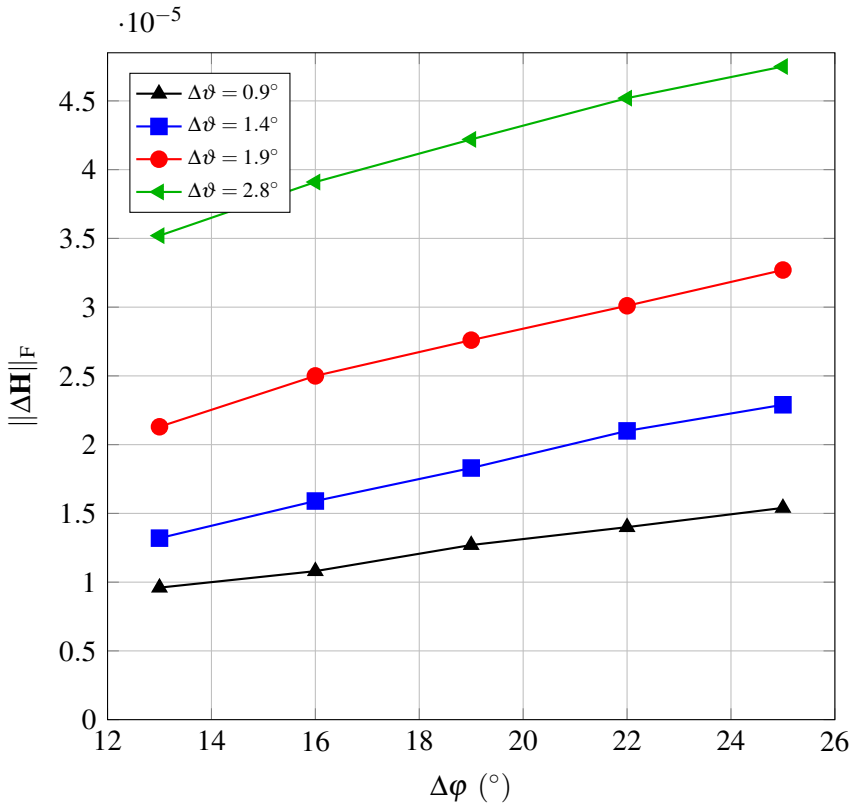


Figure 4.7: Frobenius norm error versus sweep step for different tilt-step values.

4.5.4 NOMA Sum-Rate and Fairness Performance

After evaluating the codebook, the next step is to study its impact on the multi-user NOMA-VLC system. The ORIS contains a 15×15 reflecting array unless otherwise stated. The four schemes compared are LoS+GRPA, LoS+SSA, LoS+ORIS+GRPA, and LoS+ORIS+SSA. The LoS-only schemes show the baseline without reflected assistance, while the ORIS-assisted schemes show the gain obtained from the reflecting surface.

Figure 4.9 shows the sum rate versus the number of ORIS elements for $K = 3$ users. The LoS-only schemes remain almost constant because they do not depend on the number of reflecting elements. In contrast, the ORIS-assisted schemes show a clear increase in sum rate because adding more reflecting elements strengthens the effective optical channels

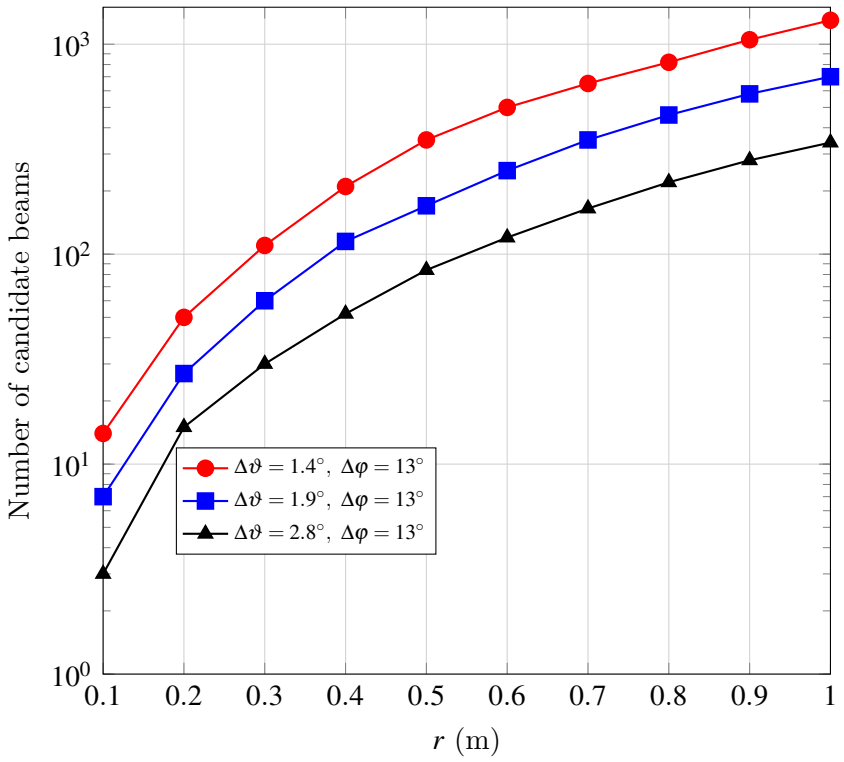


Figure 4.8: Number of candidate beams versus coverage radius for different tilt-step values.

available for NOMA transmission. The proposed LoS+ORIS+SSA scheme achieves the highest sum rate across the entire range, increasing from approximately 4.4 bps/Hz to 9.6 bps/Hz. This shows that the ORIS improves the channel quality, while SSA uses the improved channels more efficiently than the fixed GRPA rule.

Figure 4.10 shows Jain's fairness index versus the number of ORIS elements for $K = 3$ users. The LoS-only schemes remain almost constant because their channels are not affected by the ORIS size. The LoS+ORIS+GRPA scheme improves the sum rate but can reduce fairness because the reflected gain is not equally distributed among users. In contrast, the LoS+ORIS+SSA scheme shows a gradual improvement in fairness as the number of elements increases. This indicates that the logarithmic-utility optimisation uses the additional ORIS gain in a more balanced way across the users. Therefore, the proposed scheme should be interpreted as a throughput–fairness trade-off, rather than a method that only maximises Jain's index.

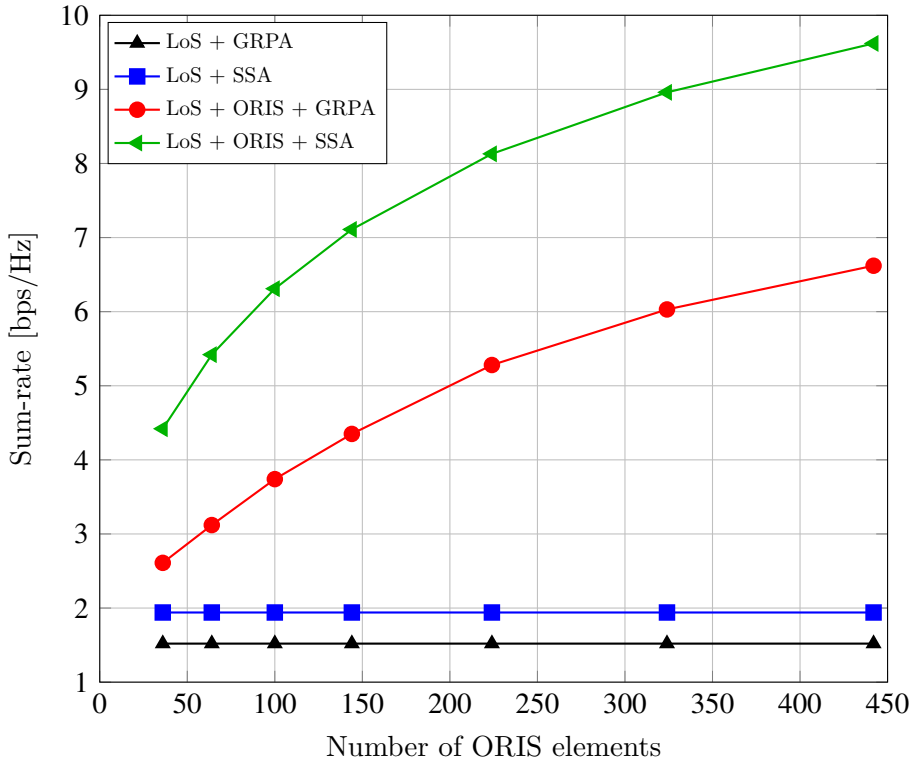


Figure 4.9: Sum rate versus number of ORIS elements for $K = 3$ users.

Figure 4.11 shows the sum rate versus the maximum transmit power $P_{\max}$ for $K = 3$, 5, and 7 users. For all user counts, the sum rate increases with $P_{\max}$ because a larger power budget improves the received SINR. The LoS-only schemes achieve the lowest rates because they rely only on the direct optical path. Once the ORIS is included, both GRPA and SSA achieve a clear throughput gain, confirming the channel-enhancement role of the reflecting surface. Among all schemes, LoS+ORIS+SSA achieves the highest sum rate across the entire power range because SSA directly optimises the logarithmic utility instead of following the fixed gain-ratio rule used by GRPA.

Figure 4.12 shows Jain's fairness index versus $P_{\max}$ for $K = 3$, 5, and 7 users. The LoS+SSA scheme achieves high fairness because the LoS-only channels are less affected by ORIS-induced geometric variations, and SSA can balance the transmit powers more easily. When the ORIS is introduced, the effective channels become more diverse because different users receive different reflected gains depending on their positions and assigned

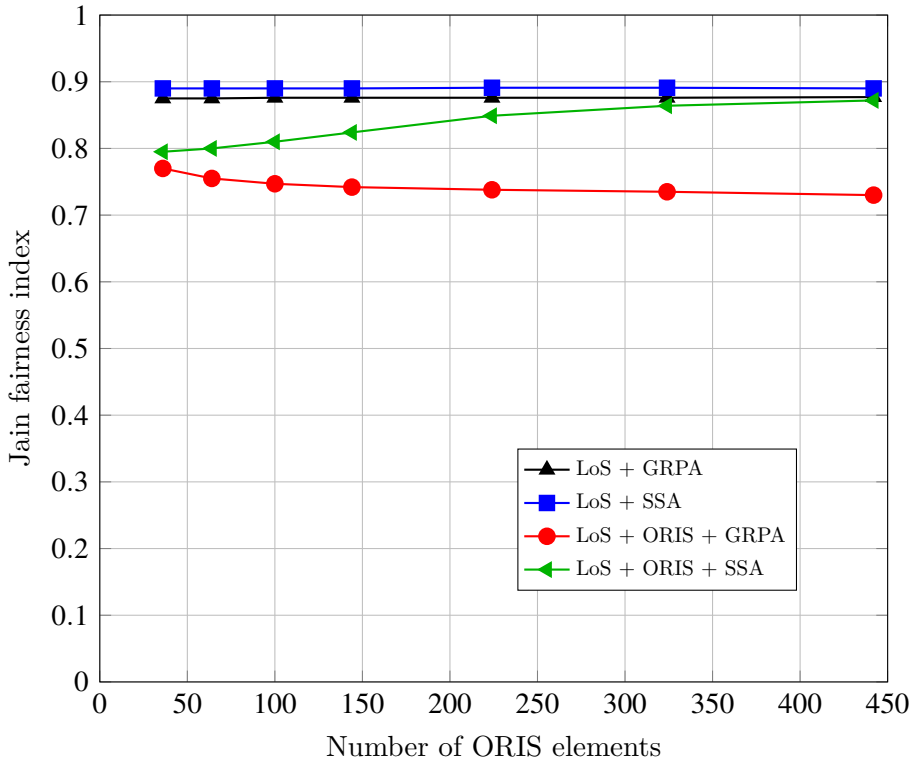


Figure 4.10: Jain fairness index versus number of ORIS elements for $K = 3$ users.

elements. Under this condition, LoS+ORIS+GRPA gives the lowest fairness because it does not directly control the rate imbalance. The proposed LoS+ORIS+SSA scheme consistently improves fairness compared with LoS+ORIS+GRPA, while still achieving a much higher sum rate than the LoS-only schemes.

Finally, Figure 4.13 shows the sum rate as the number of users increases from $K = 2$ to $K = 7$. The LoS+GRPA curve decreases because the fixed transmit-power budget is shared among more users and the fixed GRPA rule cannot adapt sufficiently. The LoS+SSA curve remains more stable because the logarithmic-utility optimisation assigns power so that additional users still contribute non-negligible rates. When the ORIS is included, both ORIS-assisted schemes achieve much higher sum rates than their LoS-only counterparts. However, their sum rates decrease with increasing K be-

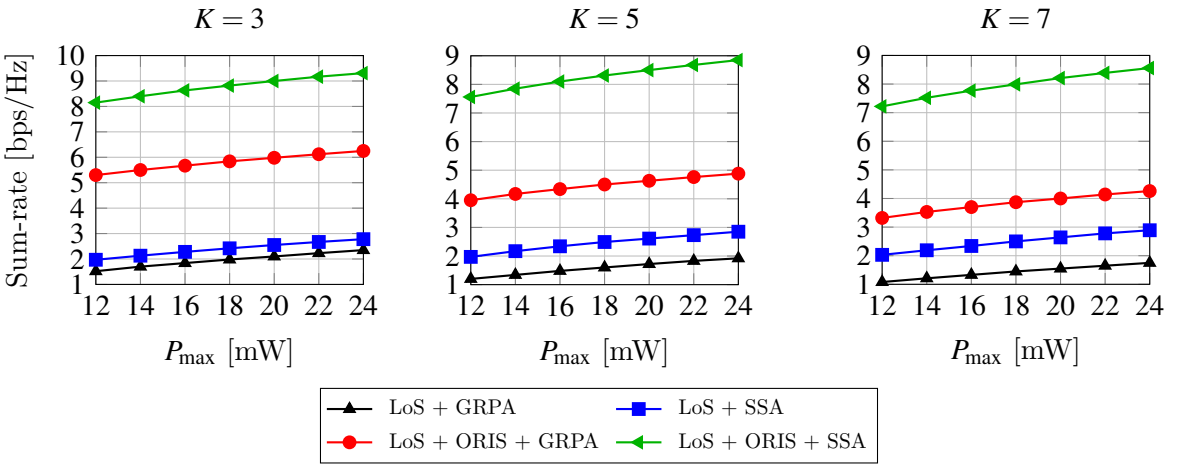


Figure 4.11: Sum rate versus maximum transmit power for $K = 3$, 5, and 7 users.

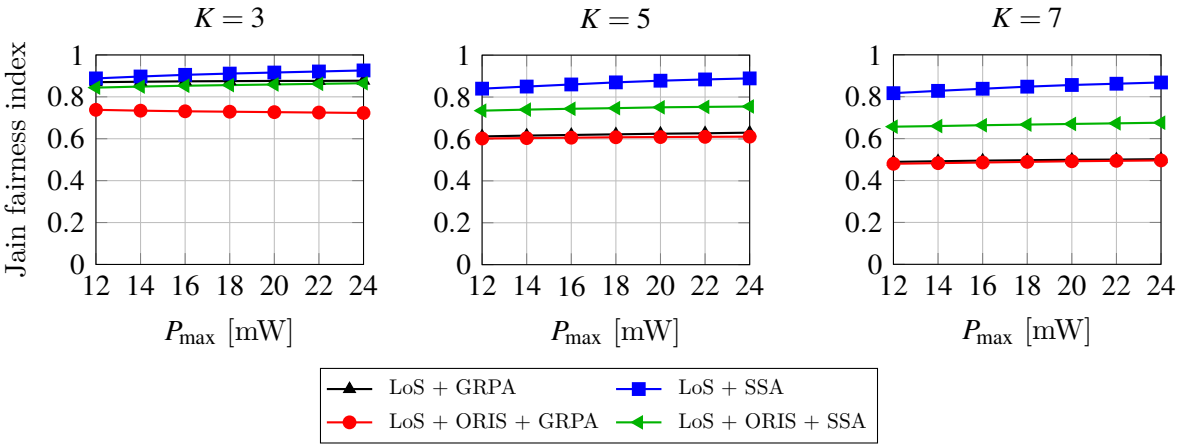


Figure 4.12: Jain fairness index versus maximum transmit power for $K = 3$, 5, and 7 users.

cause the same ORIS aperture and transmit-power budget must support more users, and the NOMA interference also increases. Even under this heavier load, the proposed LoS+ORIS+SSA scheme remains the best-performing scheme, confirming the benefit of jointly using ORIS-based channel enhancement and SSA-based power optimisation.

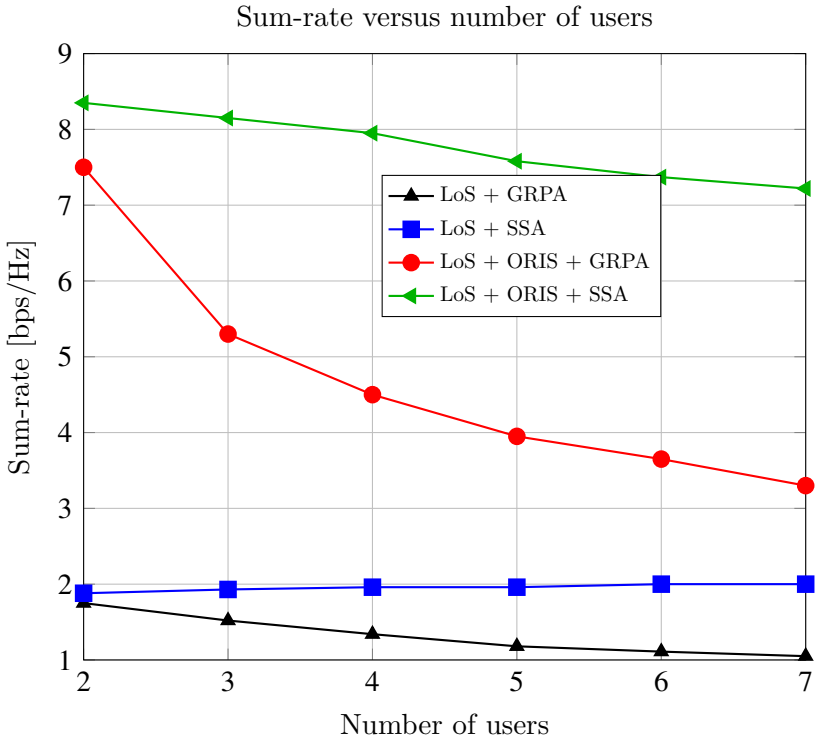


Figure 4.13: Sum rate versus number of users.

4.6 Summary

This chapter presented a non-uniform codebook design and NOMA-based resource allocation framework for ORIS-assisted indoor VLC systems. The chapter first introduced the system model, in which the received signal consists of the direct LoS component and the reflected contribution from a wall-mounted ORIS. A codebook-based beam-steering model was then developed to avoid continuous real-time optimisation of the mirror tilt and sweep angles. Since uniform angular codebooks produce non-uniform spatial coverage on the receiver plane, a geometric-optics-based non-uniform codebook was introduced to achieve more balanced beam-hit mapping for each ORIS element. The resulting codebook was used to construct an ORIS gain matrix, which connects the offline beam-steering design with online multi-user resource allocation. For NOMA transmission, a fairness-aware optimisation problem was formulated by jointly considering ORIS element assignment, transmit-power allocation, minimum-rate requirements, and optical power constraints. A two-stage solution was then presented, in which QoS-

oriented greedy allocation assigns the ORIS elements to users, while SSA optimises the NOMA power vector, with GRPA used as a benchmark. Simulation results showed that the proposed non-uniform codebook reduced spatial mapping error compared with uniform angular sampling, and that the combined LoS+ORIS+SSA scheme improved the sum rate and the throughput–fairness trade-off compared with LoS-only and GRPA-based schemes. Overall, this chapter demonstrated that practical finite codebook design and intelligent resource allocation are both essential for realising efficient and fair ORIS-assisted VLC networks. Building on these optical beam-management results, the next chapter moves to the LeRIS framework for integrated localisation, mapping, and mmWave communication.

Chapter 5

Integrated Localisation, Mapping, and Communication Through VCSEL-Based LeRIS

5.1 Introduction

The previous chapter investigated non-uniform codebook design and NOMA-based resource allocation for ORIS-assisted VLC systems. This chapter moves from ORIS-assisted optical beam management to a multi-functional LeRIS framework in which localisation, mapping, and communication are jointly supported. In future 6G indoor networks, the wireless environment is expected to become programmable, adaptive, and aware of the surrounding space [85]. This is especially important for high-frequency mmWave communication, in which signals can suffer from severe path loss and blockage [41], [86]. Therefore, accurate knowledge of user positions and surrounding obstacles is essential for reliable LeRIS configuration and robust wireless access.

To address these challenges, a LeRIS-enabled PWE can reshape mmWave propagation and improve communication reliability [61], [87], [88]. A multi-functional LeRIS can extend this role by incorporating optical sensing, localisation, and environmental awareness into the wireless infrastructure [43], [54]. However, relying only on electromagnetic measurements may introduce trade-offs between communication, localisation, and sensing, because optimising the LeRIS configuration for one task can reduce its effectiveness for another.

Optical sources provide a practical way to add environmental awareness to LeRIS-enabled indoor systems. Because optical measurements are strongly dependent on geometry and operate in a spectral band separate from the RF or mmWave communication link, they can provide spatial references for localisation and mapping [43], [89]. Several studies have investigated LED-based optical anchors for indoor positioning, using their broad illumination patterns and existing lighting infrastructure to achieve centimetre-level localisation accuracy through received-signal-strength and geometric positioning methods [70], [71].

VCSELs offer a different set of source characteristics, including narrow Gaussian beams, compact form factor, fast modulation, and low-power operation. Previous studies have shown that VCSEL arrays can support reliable optical access under random user orientation, deep-learning-based position and orientation estimation, and high-speed multi-gigabit optical transmission [38], [39], [40]. Their directional emission is particularly suitable for scanning-based localisation and environmental sensing, whereas LEDs remain well suited to broad illumination and coverage-oriented positioning.

Building on these complementary source characteristics, this chapter considers a VCSEL-based LeRIS. Compact VCSEL sources are arranged along each LeRIS panel to provide narrow Gaussian beams for user localisation and obstacle-aware mapping, while the reflecting elements support mmWave communication. The selected source configuration is therefore matched to the spatially selective sensing requirements of the proposed framework [43], [62].

This chapter develops a VCSEL-based LeRIS framework in which localisation, mapping, and mmWave communication are jointly considered. The framework derives closed-form localisation and orientation estimates from VCSEL measurements, proposes a VCSEL-based method for detecting obstructed links, and uses the resulting environmental awareness to guide blockage-resilient LeRIS-assisted mmWave routing.

The main contributions of this chapter are summarised as follows:

- A VCSEL-based LeRIS architecture is presented for indoor PWEs, in which VCSELs are integrated with LeRIS panels to support localisation and sensing in parallel with mmWave communication.
- Closed-form localisation and orientation estimation methods are presented, including a five-VCSEL formulation and a dual-mode three-VCSEL formulation.
- A VCSEL-based obstacle mapping method is described, in which reflected optical signals are used to identify blocked and unblocked links for environment-aware route selection.
- A LeRIS-assisted mmWave communication model is developed, in which the estimated user position and mapping information are used to select feasible routes and improve multi-user communication performance.

The remainder of this chapter is organised as follows. Section 5.2 presents the VCSEL-based LeRIS system and channel model. Section 5.3 introduces the localisation and mapping framework. Section 5.4 presents the obstacle-aware LeRIS-assisted communication model. Section 5.5 discusses the simulation results. Finally, Section 5.6 summarises the chapter.

5.2 System and Channel Model

5.2.1 VCSEL-Based LeRIS Architecture

To realise the ISAC framework introduced above, this section considers a PWE deployed within an indoor space, as shown in Figure 5.1. A mmWave AP, equipped with a directional antenna and located outside the room, aims to communicate with multiple user equipment (UEs) within the enclosed environment. Because high-frequency signals are inherently susceptible to blockage and the room contains obstructing walls and randomly positioned objects, direct LoS transmission from the AP to the UEs becomes infeasible. To overcome this limitation, four LeRIS panels are deployed at the centres of the room walls. Each LeRIS combines a programmable reflecting surface for mmWave beam routing with integrated VCSELs for optical localisation and environmental sensing.

The proposed LeRIS architecture transforms a conventional passive reflecting panel into a multi-functional surface. The reflecting elements manipulate the mmWave signal, while the VCSELs provide spatially structured optical illumination. In this way, the same panel supports three connected functions: user localisation, obstacle-aware mapping, and mmWave communication. The VCSELs are placed along the perimeter of each LeRIS panel, and their narrow Gaussian beams scan small angular sectors to cover the indoor environment.

A TDMA protocol is considered for multi-user access, in which each time slot is assigned to one UE. At the beginning of each slot, the UE estimates its 3D position by receiving optical signals from the VCSELs. To allow beam identification, each VCSEL transmits at a distinct infrared tone, so that the UE can separate the received signals in the frequency domain. The estimated position is then reported to the AP over a control channel.

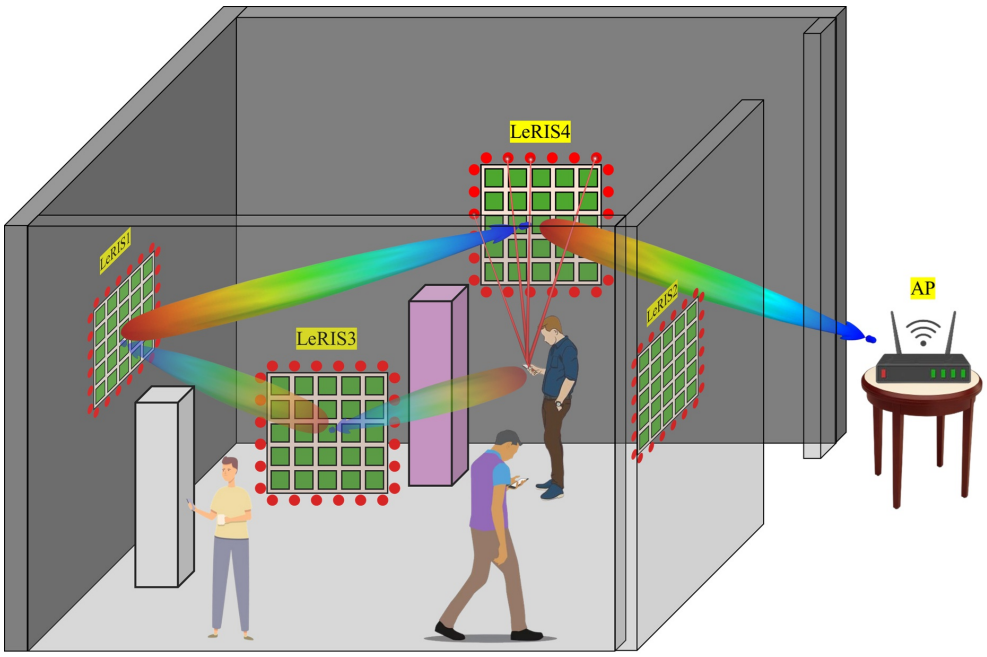


Figure 5.1: Indoor PWE with VCSEL-based LeRIS panels for localisation, mapping, and mmWave communication.

In parallel with localisation, the LeRIS panels also perform environmental sensing. Co-located PDs, positioned near the VCSELs, measure reflected optical signals from objects in the room. Since the VCSELs emit highly directional beams, the measured reflections can be associated with the known beam direction and range, allowing the system to identify potential obstacles and blocked links. The AP then uses the estimated UE position and the obstacle map to select a feasible LeRIS-assisted mmWave route. Therefore, the overall system jointly performs localisation, mapping, and communication within the same programmable environment.

5.2.2 Optical VCSEL Channel Model

The optical channel is used for localisation and sensing. In the proposed architecture, VCSELs generate narrow, low-divergence beams with Gaussian spatial intensity profiles, whereas LEDs are generally associated with broader illumination patterns. The directional VCSEL emission provides the spatial selectivity required to estimate the position and orientation of the UE.

For the localisation and mapping problem considered in this chapter, the Gaussian beam model is written in angular form so that the effects of propagation distance and beam misalignment can be directly included in the received optical power. For a receiver located at an angular offset from the beam axis, the Gaussian beam model can be written in terms of the distance $d_{i,k}$ between the ith VCSEL and the kth UE, and the irradiance angle ϕ. The angular intensity distribution is [39]

$$I_{i,k}(d,\phi) = \frac{2P_{\mathrm{t},i}}{\pi w^2 (d_{i,k}\cos\phi)} \exp\left(-\frac{2d_{i,k}^2 \sin^2\phi}{w^2(d_{i,k}\cos\phi)}\right). \tag{5.1}$$

This expression shows that the received intensity depends not only on the distance between the VCSEL and the UE, but also on the angular alignment between the beam and the receiver.

Based on the angular intensity, the received LoS optical power at the PD of the kth UE is expressed as

$$P_{\mathrm{LoS},i,k} = I_{i,k}(d,\phi) A_{\mathrm{PD}} \cos(\psi_{i,k}) \,\mathrm{rect}\left(\frac{\psi_{i,k}}{\Psi}\right), \tag{5.2}$$

where A_{PD} is the active area of the PD, $\psi_{i,k}$ is the incidence angle, and Ψ is the receiver half-angle FoV. The rectangular function ensures that the received optical signal is considered only when the incidence angle lies inside the receiver FoV. It is defined as

$$\mathrm{rect}\left(\frac{\psi_{i,k}}{\Psi}\right) = \begin{cases} 1, & |\psi_{i,k}| \le \Psi, \\ 0, & |\psi_{i,k}| > \Psi. \end{cases} \tag{5.3}$$

The total received optical power from the ith VCSEL at the kth UE includes both the LoS optical component and the receiver noise. It is written as

$$P_{\mathrm{r},i,k} = P_{\mathrm{LoS},i,k} + P_{\mathrm{n},i,k}, \tag{5.4}$$

where $P_{\mathrm{n},i,k}$ is the optical noise power. The noise power is modelled as

$$P_{\mathrm{n},i,k} = B_{\mathrm{o}} S_{i,k}, \tag{5.5}$$

where B_{o} is the effective optical bandwidth and $S_{i,k}$ is the single-sided noise power spectral density.

The noise spectral density is given by [39]

$$S_{i,k} = A_{\mathrm{K}} + R_{\mathrm{PD}} P_{\mathrm{LoS},i,k} \left(2q + \mathrm{RIN} R_{\mathrm{PD}} P_{\mathrm{LoS},i,k}\right), \tag{5.6}$$

where R_{PD} is the PD responsivity, q is the electron charge, and RIN is the relative intensity noise (RIN). The first term in (5.6) represents the thermal noise contribution, while the remaining terms account for shot noise and RIN. The coefficient A_{K} denotes the thermal-noise current spectral-density term associated with the receiver electronics. It is used here as a compact parameter in the VCSEL RSS model, consistent with the receiver-noise discussion in Chapter 2 and the classical IM/DD optical wireless noise model [44]. This optical channel model captures the Gaussian beam propagation, receiver orientation, and noise effects required for VCSEL-based localisation and sensing.

5.2.3 mmWave Communication Model

After the UE position and obstacle information are obtained through the VCSEL-based localisation and sensing process, the AP selects a cascaded LeRIS route to serve the kth UE. The selected route may include L participating LeRIS panels. Each intermediate LeRIS steers the incident mmWave signal towards the next LeRIS, while the final LeRIS steers the signal towards the estimated direction of the UE. The estimated direction of the kth UE is denoted by $(\hat{\theta}_{\mathrm{r},k}, \hat{\varphi}_{\mathrm{r},k})$.

Each LeRIS panel is composed of $M_{\mathrm{x}} \times N_{\mathrm{y}}$ square reflecting elements with side length D. Here, M_{x} and N_{y} denote the number of reflecting elements along the two panel dimensions. This notation is used to avoid confusion with the number of users K and other indices used elsewhere in the thesis. The effective directional gain of a LeRIS in the target direction (θ, φ) is given by

$$G(\theta,\varphi) = \eta_{\mathrm{eff}} \frac{4\pi |F(\theta,\varphi)|^2}{\int_0^{2\pi} \int_0^{\frac{\pi}{2}} |F(\theta,\varphi)|^2 \sin(\theta)\, \mathrm{d}\theta\, \mathrm{d}\varphi}, \tag{5.7}$$

where η_{eff} is the aperture efficiency, and $F(\theta,\varphi)$ is the far-field radiation pattern of the LeRIS array.

The far-field radiation pattern is expressed as

$$F(\theta,\varphi) = \sum_{a=1}^{M_{\mathrm{x}}} \sum_{b=1}^{N_{\mathrm{y}}} \exp\left[j \left(k_0 \zeta_{ab}(\theta,\varphi) + \omega_{ab} + \Phi_{ab} \right) \right], \tag{5.8}$$

where a and b are the element indices along the two dimensions of the LeRIS panel, $k_0 = 2\pi/\lambda_{\mathrm{m}}$ is the mmWave wavenumber, λ_{m} is the mmWave wavelength, $\zeta_{ab}(\theta,\varphi)$ is the geometry-dependent phase term, ω_{ab} is the propagation phase offset, and Φ_{ab} is the phase shift applied by the (a,b)th reflecting element.

The geometry-dependent phase term can be written as

$$\begin{aligned} \zeta_{ab}(\theta,\varphi) =& D \sin(\theta) \left[\left(a - \frac{1}{2} \right) \cos(\varphi) + \left(b - \frac{1}{2} \right) \sin(\varphi) \right] \\ &+ (x_{\mathrm{T}} - x_{\mathrm{R}}) \sin(\theta) \cos(\varphi) + (y_{\mathrm{T}} - y_{\mathrm{R}}) \sin(\theta) \sin(\varphi) \\ &+ (z_{\mathrm{T}} - z_{\mathrm{R}}) \cos(\theta), \end{aligned} \tag{5.9}$$

where $(x_{\mathrm{T}}, y_{\mathrm{T}}, z_{\mathrm{T}})$ are the coordinates of the transmitting or reflecting node, and $(x_{\mathrm{R}}, y_{\mathrm{R}}, z_{\mathrm{R}})$ denotes the centre of the receiving node.

The propagation phase offset ω_{ab} accounts for the path delay from the transmitting node to the (a,b)th reflecting element. It can be written as

$$\omega_{ab} = k_0 d_{\mathrm{T},ab}, \tag{5.10}$$

where $d_{\mathrm{T},ab}$ is the distance from the transmitting node to the (a,b)th reflecting element. This term captures the phase accumulated before the signal reaches each reflecting element.

To steer the reflected signal towards the estimated UE direction $(\hat{\theta}_{\mathrm{r},k}, \hat{\varphi}_{\mathrm{r},k})$, the phase shift applied by the (a,b)th element is configured as

$$\Phi_{ab} = -k_0 D \left[a\cos(\hat{\varphi}_{\mathrm{r},k})\sin(\hat{\theta}_{\mathrm{r},k}) + b\sin(\hat{\varphi}_{\mathrm{r},k})\sin(\hat{\theta}_{\mathrm{r},k}) \right] - \omega_{ab}. \tag{5.11}$$

This phase configuration compensates for the propagation phase offset and steers the outgoing wavefront towards the estimated UE direction.

When a LeRIS panel steers towards another LeRIS with known position and orientation, the beam is assumed to be perfectly aligned. Under this condition, the far-field response is maximised and the achievable gain becomes

$$G_{\max} = \eta_{\mathrm{eff}} M_{\mathrm{x}} N_{\mathrm{y}}. \tag{5.12}$$

For a cascaded route with L participating LeRIS panels, the cumulative gain contributed by the first $L-1$ panels is

$$G_{\mathrm{cas}} = \prod_{\ell=1}^{L-1} \left(A_{\mathrm{eff}} G_{\max} \right), \tag{5.13}$$

where the effective aperture of each LeRIS panel is

$$A_{\mathrm{eff}} = \frac{M_{\mathrm{x}} N_{\mathrm{y}} \lambda_{\mathrm{m}}^2}{4\pi}. \tag{5.14}$$

For the last participating LeRIS, the beam is steered towards the estimated UE direction. However, because the UE direction is obtained from the optical localisation stage, localisation errors may create angular mismatch between the estimated direction $(\hat{\theta}_{\mathrm{r},k}, \hat{\varphi}_{\mathrm{r},k})$ and the true direction $(\theta_{\mathrm{u},k}, \varphi_{\mathrm{u},k})$ [90]. Therefore, the gain of the final LeRIS in the true UE direction is

$$G_L(\theta_{\mathrm{u},k}, \varphi_{\mathrm{u},k}) = \eta_{\mathrm{eff}} \frac{4\pi \left|F(\theta_{\mathrm{u},k}, \varphi_{\mathrm{u},k})\right|^2}{\int_0^{2\pi} \int_0^{\pi} |F(\theta, \varphi)|^2 \sin(\theta)\, \mathrm{d}\theta\, \mathrm{d}\varphi}. \tag{5.15}$$

The total directional gain accumulated along the complete route is then expressed as

$$G_{\mathrm{r},k} = G_{\mathrm{cas}} A_{\mathrm{eff}} G_L(\theta_{\mathrm{u},k}, \varphi_{\mathrm{u},k}). \tag{5.16}$$

The baseband signal received by the kth UE is given by

$$y_k = \sqrt{l_{\mathrm{p}} G_{\mathrm{t}} G_{\mathrm{r}} P_{\mathrm{t}} G_{\mathrm{r},k}}\, x + w_k, \tag{5.17}$$

where x is the transmitted symbol with unit energy, G_{t} and G_{r} are the antenna gains of the AP and the UE, respectively, P_{t} is the mmWave transmit power, $G_{\mathrm{r},k}$ is the total route gain, and w_k is additive white Gaussian noise (AWGN) with variance σ_k^2.

The total path loss over a cascaded route with L participating LeRIS panels is [91]

$$l_{\mathrm{p}} = \prod_{\ell=1}^{L+1} C_0 \left(\frac{d_{\mathrm{r},\ell}}{d_{\mathrm{r},0}} \right)^{-n_\ell}, \tag{5.18}$$

where $d_{\mathrm{r},\ell}$ is the distance of the ℓth route segment, n_ℓ is the path loss exponent of that segment, and $d_{\mathrm{r},0}$ is the reference distance. The free-space path loss at the reference distance is

$$C_0 = \frac{\lambda_{\mathrm{m}}^2}{(4\pi d_{\mathrm{r},0})^2}. \tag{5.19}$$

Finally, the achievable spectral efficiency of the kth UE is given by

$$R_k = \log_2\left(1 + l_{\mathrm{p}} G_{\mathrm{t}} G_{\mathrm{r}} G_{\mathrm{r},k} \gamma_{\mathrm{t}}\right), \tag{5.20}$$

where $\gamma_{\mathrm{t}} = P_{\mathrm{t}}/\sigma_k^2$ is the transmit SNR. In this form, the noise variance is included through γ_{t} and is not divided a second time inside the logarithm. This expression captures the joint effect of route path loss, cascaded LeRIS gain, beam steering accuracy, and localisation error on the end-to-end mmWave communication performance.

5.3 VCSEL-Based Localisation and Mapping

This section presents the VCSEL-based localisation and mapping framework used by the proposed LeRIS architecture. The localisation part uses received optical power measurements from the VCSELs to estimate the UE position and orientation. The mapping part uses reflected optical signals captured by co-located PDs to detect obstacles and identify blocked LeRIS–UE links. Together, these two functions provide the environmental awareness required for reliable mmWave route selection.

5.3.1 Closed-Form User Localisation

The position of the kth UE is estimated from the RSS measurements received from the VCSELs. Let the ith VCSEL be located at position $\mathbf{s}_i \in \mathbb{R}^3$, and let the PD of the UE be located at position $\mathbf{r} \in \mathbb{R}^3$. The unit normal vector of the PD surface is denoted by $\mathbf{n} \in \mathbb{R}^3$, with $\|\mathbf{n}\| = 1$. The distance between the ith VCSEL and the UE is

$$d_i = \|\mathbf{s}_i - \mathbf{r}\|, \tag{5.21}$$

and the unit vector pointing from the UE towards the ith VCSEL is

$$\mathbf{u}_i = \frac{\mathbf{s}_i - \mathbf{r}}{d_i}. \tag{5.22}$$

For highly directional VCSEL beams and assuming that the beam is aligned with the PD FoV, the received optical power from the ith VCSEL can be written as

$$P_i = \beta_i(d_i)\left(\mathbf{n}^{\mathrm{T}}\mathbf{u}_i\right), \tag{5.23}$$

where

$$\beta_i(d_i) = \frac{2P_{\mathrm{t},i}A_{\mathrm{PD}}}{\pi w^2(d_i)}. \tag{5.24}$$

Here, $\beta_i(d_i)$ captures the distance-dependent optical power scaling of the ith VCSEL. Equation (5.23) shows that the measured RSS depends on both the UE position and the PD orientation.

For N_{V} received VCSEL signals, the measurements can be collected in vector form as

$$\mathbf{V}(\mathbf{r})\mathbf{n} = \mathbf{p}, \tag{5.25}$$

where

$$\mathbf{p} = [P_1, P_2, \ldots, P_{N_{\mathrm{V}}}]^{\mathrm{T}}, \tag{5.26}$$

and

$$\mathbf{V}(\mathbf{r}) = \begin{bmatrix} (\beta_1(d_1)\mathbf{u}_1)^{\mathrm{T}} \\ (\beta_2(d_2)\mathbf{u}_2)^{\mathrm{T}} \\ \vdots \\ (\beta_{N_{\mathrm{V}}}(d_{N_{\mathrm{V}}})\mathbf{u}_{N_{\mathrm{V}}})^{\mathrm{T}} \end{bmatrix}. \tag{5.27}$$

For a fixed candidate position $\mathbf{r}$, the unknown orientation vector $\mathbf{n}$ appears linearly in (5.25). However, in practice, the received power measurements are affected by noise, and the equations may not intersect exactly at one point. Therefore, the localisation problem is formulated as a constrained least-squares problem,

$$\min_{\mathbf{r}\in\mathbb{R}^3,\,\|\mathbf{n}\|=1} \frac{1}{2}\left\|\mathbf{V}(\mathbf{r})\mathbf{n} - \mathbf{p}\right\|_2^2. \tag{5.28}$$

For a fixed $\mathbf{r}$, the orientation estimation subproblem becomes

$$\min_{\|\mathbf{n}\|=1} \frac{1}{2} \|\mathbf{V}\mathbf{n} - \mathbf{p}\|_2^2. \tag{5.29}$$

Using the Lagrangian method, the regularised normal equation is obtained as

$$\left(\mathbf{V}^{\mathrm{T}}\mathbf{V} + \lambda \mathbf{I}_3\right) \mathbf{n} = \mathbf{V}^{\mathrm{T}}\mathbf{p}, \tag{5.30}$$

where λ is the Lagrange multiplier and $\mathbf{I}_3$ is the 3×3 identity matrix. Therefore, the orientation vector for a given λ can be expressed as

$$\mathbf{n}(\lambda) = \left(\mathbf{V}^{\mathrm{T}}\mathbf{V} + \lambda \mathbf{I}_3\right)^{-1} \mathbf{V}^{\mathrm{T}}\mathbf{p}. \tag{5.31}$$

Here, λ is the Lagrange multiplier introduced by the unit-norm constraint on the PD orientation vector, not an arbitrary fitting parameter. For each candidate position $\mathbf{r}$, λ is selected so that the recovered orientation satisfies $\|\mathbf{n}(\lambda)\|_2 = 1$. Therefore, (5.31) is a constrained least-squares orientation estimate for a fixed candidate position. The value of λ is selected to satisfy the unit-norm constraint,

$$\varphi(\lambda) = \|\mathbf{n}(\lambda)\|_2^2 - 1 = 0. \tag{5.32}$$

Thus, for each candidate position $\mathbf{r}$, the corresponding orientation vector can be uniquely obtained as $\hat{\mathbf{n}}(\mathbf{r})$.

The position estimation problem can then be written as

$$\hat{\mathbf{r}} = \arg\min_{\mathbf{r} \in \mathbb{R}^3} J(\mathbf{r}), \tag{5.33}$$

where

$$J(\mathbf{r}) = \frac{1}{2} \|\mathbf{V}(\mathbf{r})\hat{\mathbf{n}}(\mathbf{r}) - \mathbf{p}\|_2^2. \tag{5.34}$$

Although $J(\mathbf{r})$ is continuously differentiable, it is not globally convex because d_i and $\mathbf{u}_i$ depend nonlinearly on $\mathbf{r}$. Therefore, the position estimate in (5.33) is obtained using the Levenberg–Marquardt method in variable-projection form, as detailed in Appendix A.

After the position is estimated, the UE orientation is obtained as

$$\hat{\mathbf{n}} = \hat{\mathbf{n}}(\hat{\mathbf{r}}). \tag{5.35}$$

This formulation shows that five independent VCSEL measurements are sufficient to uniquely recover the 3D position and the two orientation degrees of freedom of the UE. This is the basis of the five-VCSEL localisation method in the proposed LeRIS framework.

5.3.2 Dual-Mode VCSEL Localisation

The number of required VCSELs can be reduced when each VCSEL operates in two distinguishable optical modes. Different modes produce Gaussian beams with different beam-waist and Rayleigh-range parameters. Therefore, a single VCSEL can provide more than one independent measurement without increasing the number of physical sources.

Assume that each VCSEL emits sequentially in two optical modes, denoted by a and b. The received power from the ith VCSEL in mode $m_{\mathrm{o}} \in \{a, b\}$ is

$$P_i^{(m_{\mathrm{o}})} = \beta_i^{(m_{\mathrm{o}})}(d_i)\left(\mathbf{n}^{\mathrm{T}}\mathbf{u}_i\right), \tag{5.36}$$

where

$$\beta_i^{(m_{\mathrm{o}})}(d) = \frac{2A_{\mathrm{PD}}P_{\mathrm{t},i}^{(m_{\mathrm{o}})}}{\pi\left(w^{(m_{\mathrm{o}})}(d)\right)^2}. \tag{5.37}$$

Because the two modes originate from the same VCSEL, they share the same direction vector $\mathbf{u}_i$. Therefore, the orientation-dependent factor $\mathbf{n}^{\mathrm{T}}\mathbf{u}_i$ can be eliminated by taking the ratio of the received powers,

$$R_i = \frac{P_i^{(a)}}{P_i^{(b)}} = \frac{\beta_i^{(a)}(d_i)}{\beta_i^{(b)}(d_i)}. \tag{5.38}$$

This ratio depends only on the distance d_i and the known optical mode parameters.

Using the two-mode Gaussian beam parameters, the distance between the ith VCSEL and the kth UE can be recovered in closed form as

$$d_i = \sqrt{\frac{1-\widetilde{R}_i}{\widetilde{R}_i\left(z_{\mathrm{R}}^{(a)}\right)^{-2} - \left(z_{\mathrm{R}}^{(b)}\right)^{-2}}}, \tag{5.39}$$

where

$$\widetilde{R}_i = \frac{R_i B_b}{B_a}, \tag{5.40}$$

and

$$B_{m_{\mathrm{o}}} = \frac{2A_{\mathrm{PD}}P_{\mathrm{t},i}^{(m_{\mathrm{o}})}}{\pi\left(w_0^{(m_{\mathrm{o}})}\right)^2}. \tag{5.41}$$

Thus, each dual-mode VCSEL provides a direct estimate of the distance to the UE, independently of the unknown UE orientation.

With distance estimates from three non-collinear VCSELs, the UE position can be recovered using trilateration. The position satisfies

$$\|\mathbf{r}-\mathbf{s}_i\|^2 = d_i^2, \qquad i = 1,2,3. \tag{5.42}$$

Subtracting the first equation from the second and third equations eliminates the quadratic terms and gives the linear system

$$2\begin{bmatrix}(\mathbf{s}_2-\mathbf{s}_1)^{\mathrm{T}}\\(\mathbf{s}_3-\mathbf{s}_1)^{\mathrm{T}}\end{bmatrix}\mathbf{r}=\begin{bmatrix}\|\mathbf{s}_2\|^2-\|\mathbf{s}_1\|^2-(d_2^2-d_1^2)\\\|\mathbf{s}_3\|^2-\|\mathbf{s}_1\|^2-(d_3^2-d_1^2)\end{bmatrix}. \tag{5.43}$$

The intersection of this line with one of the original spheres in (5.42) gives two candidate points, but only one lies inside the feasible indoor region illuminated by the VCSELs. This point is selected as the UE position.

Once the position $\hat{\mathbf{r}}$ is obtained, the orientation vector is recovered. The unit vector from the UE to the ith VCSEL is

$$\hat{\mathbf{u}}_i=\frac{\mathbf{s}_i-\hat{\mathbf{r}}}{\|\mathbf{s}_i-\hat{\mathbf{r}}\|}. \tag{5.44}$$

For one selected optical mode, define

$$c_i^{(a)}=\frac{P_i^{(a)}}{\beta_i^{(a)}(d_i)}. \tag{5.45}$$

The orientation vector satisfies the linear system

$$\mathbf{U}\mathbf{n}=\mathbf{c}, \tag{5.46}$$

where

$$\mathbf{U}=\begin{bmatrix}\hat{\mathbf{u}}_1^{\mathrm{T}}\\\hat{\mathbf{u}}_2^{\mathrm{T}}\\\hat{\mathbf{u}}_3^{\mathrm{T}}\end{bmatrix},\qquad \mathbf{c}=\begin{bmatrix}c_1^{(a)}\\c_2^{(a)}\\c_3^{(a)}\end{bmatrix}. \tag{5.47}$$

If $\det(\mathbf{U})\neq 0$, the orientation vector can be recovered as

$$\tilde{\mathbf{n}}=\mathbf{U}^{-1}\mathbf{c}. \tag{5.48}$$

This shows that three dual-mode VCSELs can be sufficient for unique localisation and orientation recovery under the required geometric conditions.

In the presence of noise, the distance estimate is perturbed. For the ith VCSEL–kth UE link, the distance estimation error is written as

$$\Delta d_{i,k} = d_{i,k}\left[1 - \frac{1}{\sqrt{1+\alpha_{i,k}}}\sqrt{\alpha_{i,k} - \frac{z_{\mathrm{R},i}^2}{d_{i,k}^2}}\right], \tag{5.49}$$

where

$$\alpha_{i,k} = \frac{P_{\mathrm{LoS},i,k}}{P_{\mathrm{n},i,k}}. \tag{5.50}$$

This expression quantifies how optical noise affects the distance estimation accuracy of the VCSEL-based localisation system.

5.3.3 VCSEL-Based Obstacle Mapping

After the UE position is estimated, the system must determine whether the selected LeRIS–UE and LeRIS–LeRIS links are blocked. This is important because mmWave links are highly sensitive to obstacles, and even small objects can block the LoS path. The proposed LeRIS architecture uses the same VCSEL infrastructure for obstacle-aware mapping. As shown in Figure 5.2, multiple LeRIS panels provide complementary VCSEL coverage across the indoor environment, which supports both user localisation and obstacle-aware mapping.

During obstacle mapping, each VCSEL beam is steered over a finite set of azimuth and elevation angles. The azimuth sweep covers the horizontal direction across the room, while the elevation sweep controls the vertical pointing angle so that the beam can interrogate different heights and ranges in the indoor space. In practice, the angular step size determines the spatial resolution of the map, while the number of scanned directions and the dwell time per direction determine the refresh rate. A narrower beam gives higher spatial precision, but it also requires either more scan points or a longer

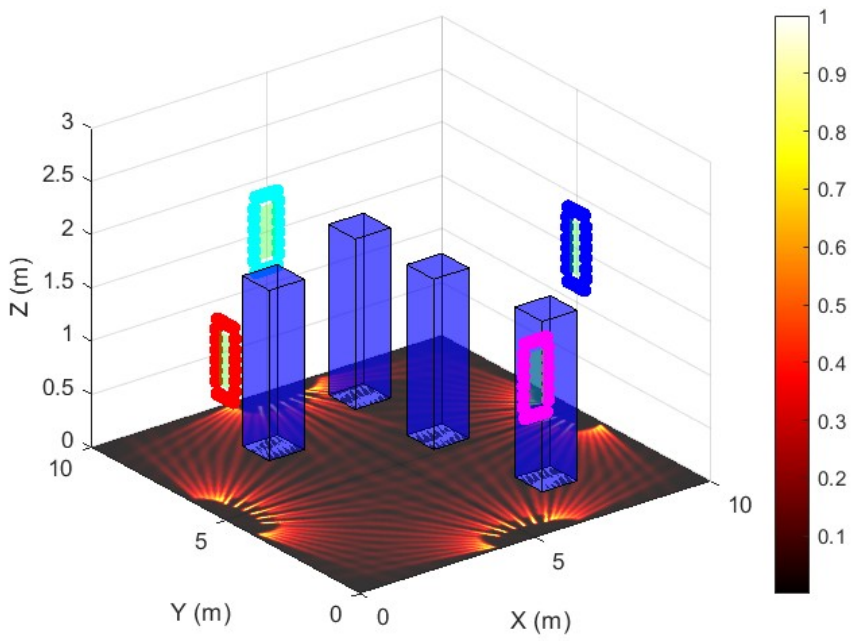


Figure 5.2: VCSEL coverage from multiple LeRIS panels.

scan time to cover the same 3D region. Therefore, the proposed scan is intended to operate over selected angular sectors around candidate communication paths, or in a coarse-to-fine manner, rather than continuously scanning the whole room at the finest angular resolution.

The VCSEL beam is steered in 3D space by varying its azimuth angle φ and elevation angle θ. Each angular pair (θ, φ) therefore defines one unique beam direction from the VCSEL origin. During the VCSEL angular sweep, each emitted beam has a unit direction

$$\mathbf{d} = [\cos\theta\cos\varphi, \cos\theta\sin\varphi, \sin\theta]^{\mathrm{T}}. \tag{5.51}$$

If a reflection is detected at range d_{V}, the corresponding reflection point is

$$\mathbf{r} = \mathbf{P} + d_{\mathrm{V}}\mathbf{d}, \tag{5.52}$$

where $\mathbf{P}$ is the beam origin. The round-trip propagation delay of the reflected optical signal is

$$\tau = \frac{2d_{\mathrm{V}}}{c}, \tag{5.53}$$

where c is the speed of light. Thus, the reflection range can be estimated from the measured time delay.

To determine whether a link between a transmitting node and a receiving node is blocked, consider the LoS segment connecting the transmitting point

$$\mathbf{P}_0 = (x_{\mathrm{T}}, y_{\mathrm{T}}, z_{\mathrm{T}})$$

and the receiving point

$$(x_{\mathrm{R}}, y_{\mathrm{R}}, z_{\mathrm{R}}).$$

The segment can be written as

$$\mathbf{r}(\mu) = \mathbf{P}_0 + \mu \mathbf{d}_{\mathrm{s}}, \qquad 0 \le \mu \le 1, \tag{5.54}$$

where

$$\mathbf{d}_{\mathrm{s}} = [x_{\mathrm{R}} - x_{\mathrm{T}}, y_{\mathrm{R}} - y_{\mathrm{T}}, z_{\mathrm{R}} - z_{\mathrm{T}}]^{\mathrm{T}} \tag{5.55}$$

is the direction vector of the segment.

Let $\mathscr{P}_{\mathrm{p}}$ be a plane that contains the LoS segment, and let $\mathbf{n}_{\mathrm{p}}$ be its unit normal vector, satisfying

$$\mathbf{n}_{\mathrm{p}}^{\mathrm{T}} \mathbf{d}_{\mathrm{s}} = 0. \tag{5.56}$$

For a detected reflection point $\mathbf{r}$, the signed distance from this plane is

$$s(\mathbf{r}) = \mathbf{n}_{\mathrm{p}}^{\mathrm{T}} (\mathbf{r} - \mathbf{P}_0). \tag{5.57}$$

If two consecutive reflection points $\mathbf{r}_1$ and $\mathbf{r}_2$ detected during the sweep satisfy

$$s(\mathbf{r}_1)s(\mathbf{r}_2) < 0, \tag{5.58}$$

then the reflection points lie on opposite sides of the plane, which indicates that an object crosses the LoS segment. Therefore, the link is considered obstructed.

A binary link-availability indicator is defined as

$$\chi_{i,k} = \begin{cases} 0, & \text{if the link between LeRIS } i \text{ and UE } k \text{ is obstructed,} \\ 1, & \text{otherwise.} \end{cases} \tag{5.59}$$

The indicator $\chi_{i,k}$ is later used in the route-selection and communication model to ensure that only feasible unobstructed links are selected. This mapping procedure allows the PWE to identify blocked paths and configure the LeRIS panels for blockage-resilient mmWave communication.

5.4 LeRIS-Assisted Communication

After the UE position has been estimated and the obstacle map has been constructed, the PWE uses this information to configure the LeRIS-assisted mmWave communication link. The main objective is to select a feasible route from the AP to the target UE through one or more LeRIS panels. A route is considered feasible only when all of its individual links are unobstructed. Therefore, the localisation and mapping stages directly support communication by providing the user position, steering direction, and link-availability information required for route selection.

5.4.1 Obstacle-Aware Route Selection

Let π denote a candidate route between the AP and the kth UE. The route may include one or more LeRIS panels. For example, a route can be formed as AP–LeRIS–UE, or it can include multiple cascaded LeRIS panels before reaching the UE. Since each route is composed of several individual segments, its feasibility depends on whether all of these segments are unobstructed.

Let $\mathscr{S}(\pi)$ denote the set of individual segments that form route π. For each segment $s \in \mathscr{S}(\pi)$, the binary indicator χ_s is used to represent whether the segment is available. Specifically, $\chi_s = 1$ means that the segment is unobstructed, while $\chi_s = 0$ means that the segment is blocked. Therefore, the route-availability indicator is defined as

$$\chi_{\pi,k} = \prod_{s \in \mathscr{S}(\pi)} \chi_s. \tag{5.60}$$

If any segment in the route is blocked, then at least one χ_s becomes zero, and hence $\chi_{\pi,k} = 0$. In this case, route π cannot be used to serve the kth UE. On the other hand, if all segments are unobstructed, then $\chi_{\pi,k} = 1$, and the route is feasible.

For each feasible route, the end-to-end spectral efficiency depends on the cascaded path loss, the directional gain of the participating LeRIS panels, and the beam alignment accuracy towards the UE. Therefore, the spectral efficiency of the kth UE through candidate route π is given by

$$R_{\pi,k} = \chi_{\pi,k} \log_2 \left(1 + \frac{P_{\mathrm{t}} G_{\mathrm{t}} G_{\mathrm{r}} l_{\mathrm{p}}(\pi) G_{\mathrm{r},k}(\pi)}{\sigma_k^2} \right), \tag{5.61}$$

where P_{t} is the mmWave transmit power, G_{t} and G_{r} are the transmit and receive antenna gains, respectively, $l_{\mathrm{p}}(\pi)$ is the total path loss of route π, $G_{\mathrm{r},k}(\pi)$ is the cascaded directional gain of the selected route, and σ_k^2 is the noise variance at the kth UE. The indicator $\chi_{\pi,k}$ ensures that blocked routes have zero spectral efficiency.

The optimal route for the kth UE is selected as the route that provides the maximum spectral efficiency among all candidate routes. Thus, the achievable spectral efficiency of the kth UE is written as

$$R_k = \max_{\pi} R_{\pi,k}. \tag{5.62}$$

This equation shows that the final communication performance depends not only on the mmWave channel gain, but also on the accuracy of the localisation and mapping stages. Accurate localisation improves the final LeRIS beam steering direction, while accurate mapping prevents the system from selecting blocked routes. This is the main connection between sensing and communication in the proposed VCSEL-based LeRIS framework.

5.4.2 TDMA-Based Multi-User Rate Optimisation

When multiple UEs are present in the indoor environment, the system must also decide how to share the available transmission time among them. Since a TDMA protocol is adopted, each UE is served during a fraction of the total time. Let τ_k denote the time-allocation factor assigned to the kth UE, with $0 \leq \tau_k \leq 1$. The effective achievable rate of the kth UE is therefore $\tau_k R_k$.

To provide fairness among all UEs, the time-allocation problem is formulated as a max-min optimisation problem. The objective is to maximise the minimum achievable user rate, denoted by $R_{\min}$. The optimisation problem is written as

$$\begin{aligned} \max_{\{\tau_k\}, R_{\min}} \quad & R_{\min} \\ \text{s.t.} \quad & \tau_k R_k \geq R_{\min}, \qquad \forall k \in \mathscr{K}, \\ & \sum_{k=1}^{K} \tau_k = 1, \\ & 0 \leq \tau_k \leq 1, \qquad \forall k \in \mathscr{K}, \end{aligned} \tag{5.63}$$

where $\mathscr{K}$ is the set of UEs and K is the number of UEs. The first constraint ensures that every UE achieves at least the minimum rate $R_{\min}$. The second constraint ensures that the total allocated time is equal to one frame. The last constraint ensures that each time-allocation factor is physically valid.

The problem in (5.63) is convex because the objective is linear and the constraints are affine in the optimisation variables. Therefore, the globally optimal time allocation can be efficiently obtained. This fairness-oriented formulation is important because users may experience different route qualities due to their positions, orientations, and blockage conditions. By optimising the time-allocation factors, the system improves the worst-user performance and avoids serving only users with favourable channel conditions.

The complete operation of the proposed LeRIS-assisted communication framework can therefore be summarised as follows. First, the VCSELs estimate the UE position and orientation. Second, the reflected optical measurements are used to determine which links are blocked or unobstructed. Third, the AP evaluates the feasible LeRIS-assisted routes and selects the route with the highest spectral efficiency for each UE. Finally, the TDMA time-allocation problem is solved to maximise the minimum user rate. In this way, the proposed framework connects localisation, mapping, and communication into one integrated VCSEL-based LeRIS system.

5.5 Simulation Results and Discussion

This section presents the simulation results for the proposed VCSEL-based LeRIS framework. The results evaluate the performance of the system in terms of localisation accuracy, obstacle-aware route selection, spectral efficiency, and multi-user fairness. The simulations consider an indoor PWE with four LeRIS panels deployed at the centres of the room walls. Each LeRIS is equipped with integrated VCSELs for localisation and sensing, and programmable reflecting elements for mmWave communication.

5.5.1 Simulation Setup

The simulation environment consists of a $10 \times 10 \times 3$ m^3 indoor room. Four LeRIS panels are placed at the centres of the four walls. The centre coordinates of the panels are $(0, 5, 1.5)$, $(10, 5, 1.5)$, $(5, 0, 1.5)$, and $(5, 10, 1.5)$, respectively. Each LeRIS panel contains 24 VCSELs arranged along its perimeter. The VCSELs jointly cover an azimuthal sector of 120° and an elevation span of 60°, with each VCSEL rotating over a small angular segment. This arrangement provides wide angular coverage while maintaining the fine spatial resolution of narrow VCSEL beams.

The UEs are uniformly distributed inside the room, with horizontal coordinates selected from $x_\mathrm{u} \in [0, 10]$ m and $y_\mathrm{u} \in [0, 10]$ m. The UE height is fixed at $z_\mathrm{u} = 1.5$ m, which corresponds to a typical indoor user height and is aligned with the LeRIS panel centres. The UE azimuth orientation is uniformly distributed over $[0, 2\pi]$, while the elevation orientation is set to zero. In addition, randomly positioned cuboid obstacles are introduced to model blockage events. Each obstacle has dimensions $1 \times 1 \times 1.6$ m^3.

The main VCSEL simulation parameters are summarised in Table 5.1, while the mmWave communication parameters are summarised in Table 5.2. These values are selected for the specific objective of this chapter, which is to evaluate VCSEL-based localisation, obstacle mapping, and LeRIS-assisted mmWave route selection. Therefore, they are not intended to match the VLC secrecy and codebook studies in Chapters 3 and 4. Instead, they provide a consistent indoor link-level scenario for comparing localisation accuracy, blockage resilience, spectral efficiency, and multi-user fairness within the proposed LeRIS framework.

Table 5.1: Simulation parameters for VCSEL-based localisation and sensing.

Parameter	**Value**
LeRIS 1 centre	$(0,5,1.5)$ m
LeRIS 2 centre	$(10,5,1.5)$ m
LeRIS 3 centre	$(5,0,1.5)$ m
LeRIS 4 centre	$(5,10,1.5)$ m
PD area	$A_{\mathrm{PD}} = 1$ cm^2
VCSEL transmit power	$P_{\mathrm{t},i} = 10$ mW
Beam waist	$w_0 = 5.6$ μm
Speed of light	$c = 3 \times 10^8$ m/s
VCSEL wavelength	$\lambda_{\mathrm{o}} = 950$ nm
Optical bandwidth	$B_{\mathrm{o}} = 1$ GHz
RIN	$\mathrm{RIN} = -155$ dB/Hz
Preamplifier noise figure	$F_{\mathrm{n}} = 5$ dB
PD FoV	$\Psi = 90^\circ$
Optical noise power	$P_{\mathrm{n},i,k} = 2.5 \times 10^{-12}$ W
Load resistance	$R_{\mathrm{L}} = 50$ Ω
Absolute temperature	$T_{\mathrm{k}} = 300$ K
Boltzmann constant	$k_{\mathrm{B}} = 1.380649 \times 10^{-23}$ J/K
PD responsivity	$R_{\mathrm{PD}} = 0.7$ A/W

Table 5.2: Simulation parameters for mmWave communication.

Parameter	**Value**
mmWave wavelength	$\lambda_{\mathrm{m}} = 10^{-2}$ m
Transmit power	$P_{\mathrm{t}} = 1$ W
Transmitter antenna gain	$G_{\mathrm{t}} = 10$ dB
Receiver antenna gain	$G_{\mathrm{r}} = 0$ dB
Reference distance	$d_{\mathrm{r},0} = 1$ m
Path loss exponent	$n_\ell = 2$
Element spacing	$D = \lambda_{\mathrm{m}}/2$
LeRIS efficiency	$\eta_{\mathrm{eff}} = 100\%$
AWGN variance	$\sigma_k^2 = -130$ dB

The dimensional quantities in Tables 5.1 and 5.2 are reported with their physical units, while dimensionless quantities such as LeRIS efficiency, path-loss exponent, and antenna gains in dB are reported in their usual communication-system form. The VCSEL parameters determine the optical sensing accuracy, whereas the mmWave parameters define the link-budget assumptions used for the communication results. This separation is necessary because the optical subsystem is used for localisation and mapping, while the mmWave subsystem is used for data communication.

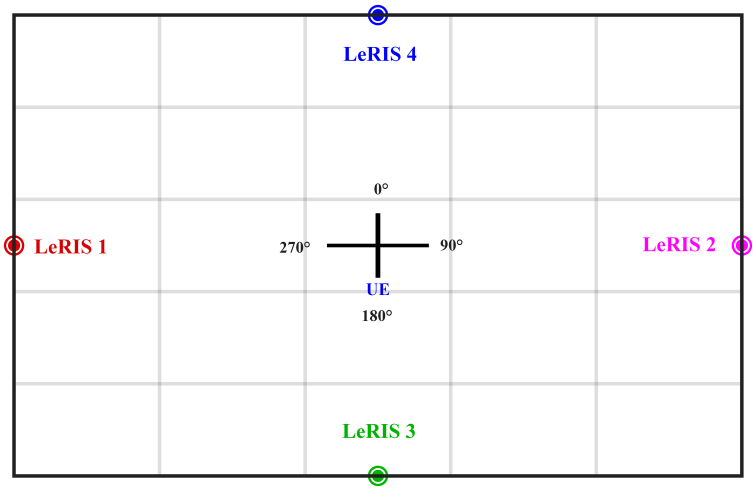


Figure 5.3: Reference geometry for UE azimuth orientation with respect to the four LeRIS panels.

5.5.2 Localisation Performance

Figure 5.3 shows the reference geometry used for the UE azimuth orientation. The angle 0° corresponds to the UE facing LeRIS 4, while 90°, 180°, and 270° correspond to LeRIS 2, LeRIS 3, and LeRIS 1, respectively.

Figure 5.4 shows the localisation error $\Delta d_{i,k}$ as a function of the UE azimuth orientation φ_{UE} for different numbers of active LeRIS panels. When only one LeRIS panel is active, the localisation error remains low only when the UE is oriented towards the coverage region of that panel. However, when the UE rotates away from the active panel, the received optical power decreases and the localisation error increases. This behaviour is expected because VCSELs provide high spatial precision but have narrow angular coverage.

When two opposite LeRIS panels are active, the angular coverage becomes wider, and the localisation error is reduced over a larger range of UE orientations. Finally, when all four LeRIS panels are active, the localisation error remains consistently low over the full 360° orientation range. This confirms that cooperation among multiple VCSEL-based LeRIS panels can overcome the limited angular coverage of individual VCSELs and provide robust localisation regardless of UE orientation.

For the considered simulation settings, the proposed VCSEL-based architecture achieves millimetre-level localisation accuracy, whereas the LED-based LeRIS benchmark provides centimetre-level accuracy. The difference arises from the narrow Gaussian beam profile, strong directionality, and angular scanning capability used in the proposed configuration. Therefore, this configuration provides more precise position information for subsequent mmWave beam routing.

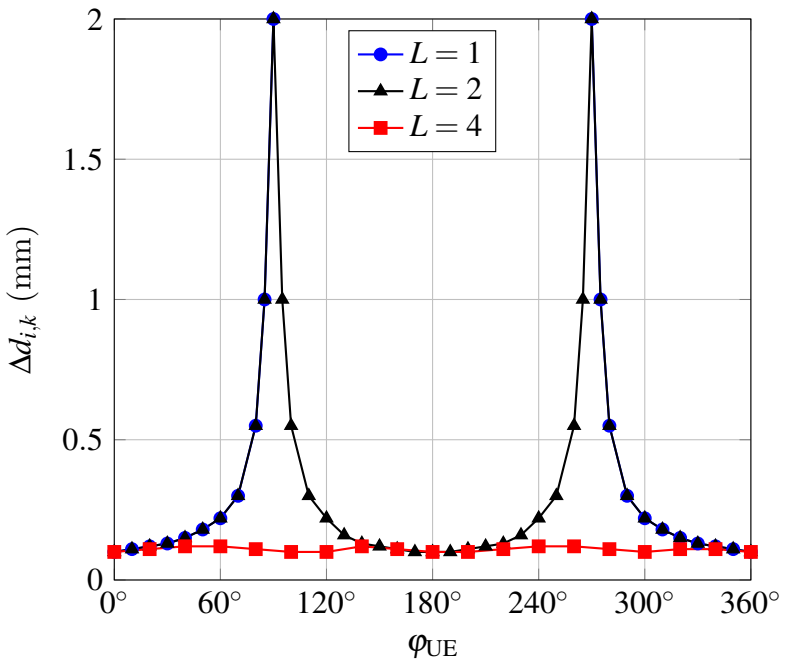


Figure 5.4: Localisation error versus UE azimuth orientation for different numbers of active LeRIS panels.

5.5.3 Spectral Efficiency Performance

Figure 5.5 shows the spectral efficiency R_k as a function of the transmit SNR γ_t for different numbers of participating LeRIS panels. The results show that increasing the number of active LeRIS panels improves spectral efficiency. When only one LeRIS panel is used, the system has limited route diversity and cannot easily avoid blocked paths. Therefore, the communication performance is strongly affected by obstacle placement.

In contrast, when multiple LeRIS panels are active, the system can identify alternative unobstructed routes using the VCSEL-based mapping information. Although cascaded reflection may introduce additional path loss, the availability of multiple routes provides stronger blockage resilience. As a result, the spectral efficiency improves across the considered SNR range. This shows that the sensing function of the VCSEL-based LeRIS is useful not only for mapping but also for directly improving communication through obstacle-aware route selection.

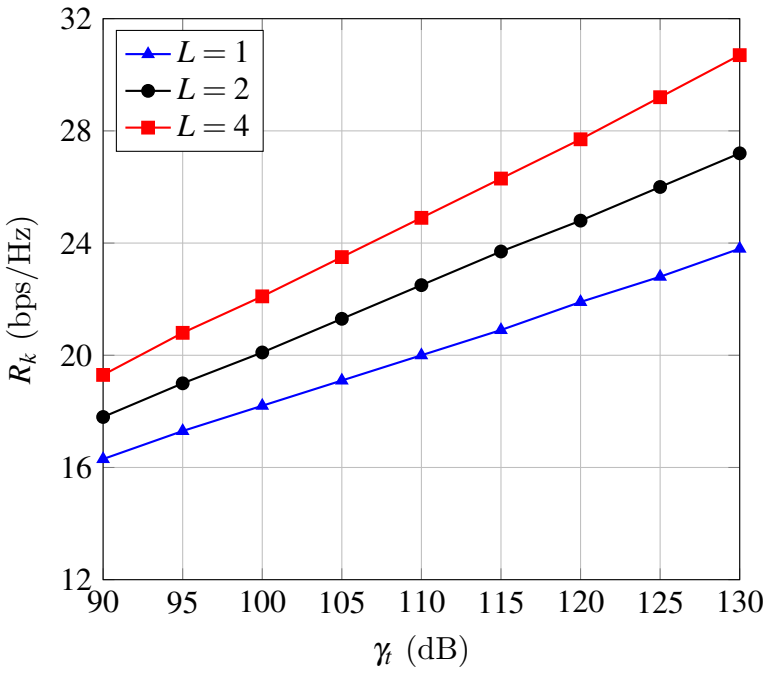


Figure 5.5: Spectral efficiency versus transmit SNR for different numbers of participating LeRIS panels.

Figure 5.6 shows the spectral efficiency as a function of the number of reflecting elements. As the number of elements increases, the beamforming gain of each LeRIS panel also increases. This improves the quality of the reflected route and leads to higher spectral efficiency. However, the benefit of increasing the number of LeRIS panels depends on the number of reflecting elements available at each panel.

For a small number of reflecting elements, the additional cascaded routes created by multiple LeRIS panels may suffer from strong path loss, and the gain over the single-panel case is limited. As the number of elements increases, the higher beamforming gain compensates for the cascaded path loss, and the performance gap between single- and multi-panel deployments becomes larger. Therefore, the number of active panels provides route diversity, while the number of reflecting elements determines how efficiently these routes can be exploited.

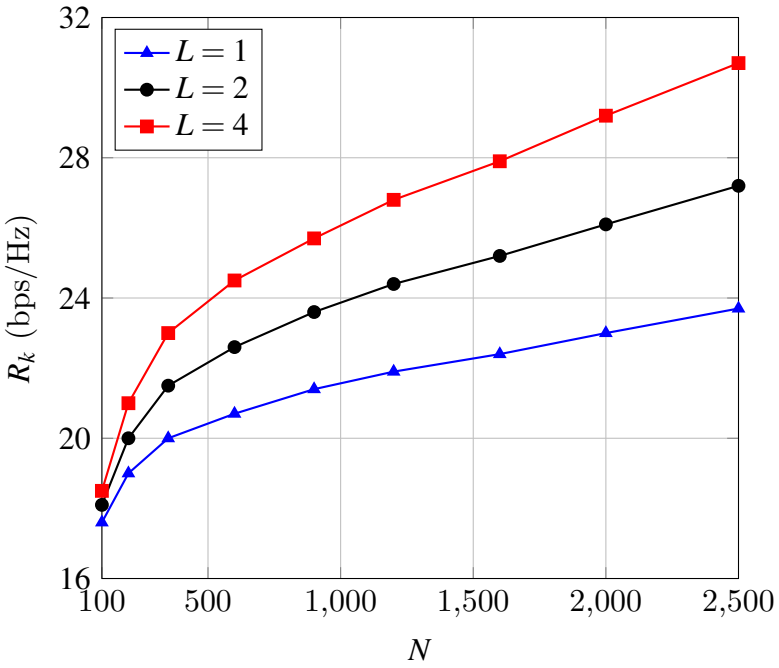


Figure 5.6: Spectral efficiency versus number of reflecting elements for different numbers of LeRIS panels.

5.5.4 Obstacle-Aware Communication Performance

Figure 5.7 presents the spectral efficiency as a function of the transmit SNR for different numbers of obstacles. As expected, increasing the number of obstacles reduces the achievable spectral efficiency, because more links become blocked and fewer feasible routes are available. This degradation is more severe when only one LeRIS panel is active, since the system has limited routing flexibility.

When four LeRIS panels are active, the impact of additional obstacles becomes less severe. This is because the proposed VCSEL-based mapping method identifies blocked links and allows the AP to select alternative unobstructed routes. Therefore, even in dense blockage conditions, the cooperation of multiple LeRIS panels maintains reliable communication. These results demonstrate that obstacle-aware mapping is essential for robust mmWave communication in indoor PWEs.

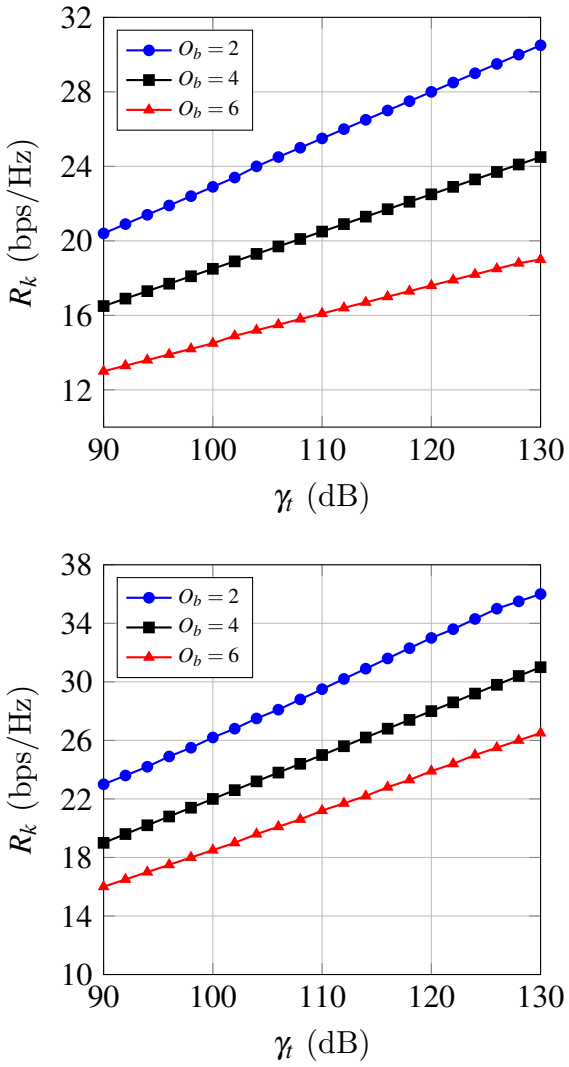


Figure 5.7: Spectral efficiency versus transmit SNR for different numbers of obstacles: (a) one active LeRIS panel and (b) four active LeRIS panels.

5.5.5 Multi-User Fairness Performance

Figure 5.8 shows the cumulative distribution function (CDF) of the minimum user rate $R_{\min}$ under the TDMA-based max-min optimisation. The results compare different numbers of participating LeRIS panels for both single-user and multi-user cases. In the single-user case, the entire transmission time is assigned to one UE, and therefore the achieved minimum rate is mainly determined by the selected route quality and blockage condition.

In the multi-user case, the benefit of multiple LeRIS panels becomes more significant. When only one LeRIS panel is active, several users may experience poor route quality due to blockage or unfavourable position. As a result, the minimum user rate is limited. When four LeRIS panels are active, the route diversity increases, and the system can provide better links to more users. This shifts the distribution of $R_{\min}$ towards higher values and improves fairness across the user set.

These results show that multiple VCSEL-based LeRIS panels are useful not only for increasing the rate of a single user, but also for improving multi-user fairness. The combination of accurate localisation, obstacle-aware mapping, and route diversity allows the system to reduce outage probability and improve the worst-user performance. Therefore, the proposed LeRIS framework provides a practical approach for resilient multi-user indoor mmWave communication.

5.6 Summary

This chapter presented an integrated localisation, mapping, and communication framework based on VCSEL-enabled LeRIS. The proposed architecture combines programmable reflecting elements for mmWave communication with integrated VCSELs for optical localisation and obstacle-aware mapping. A Gaussian VCSEL channel model, including received optical power and noise expressions, was introduced and used to de-

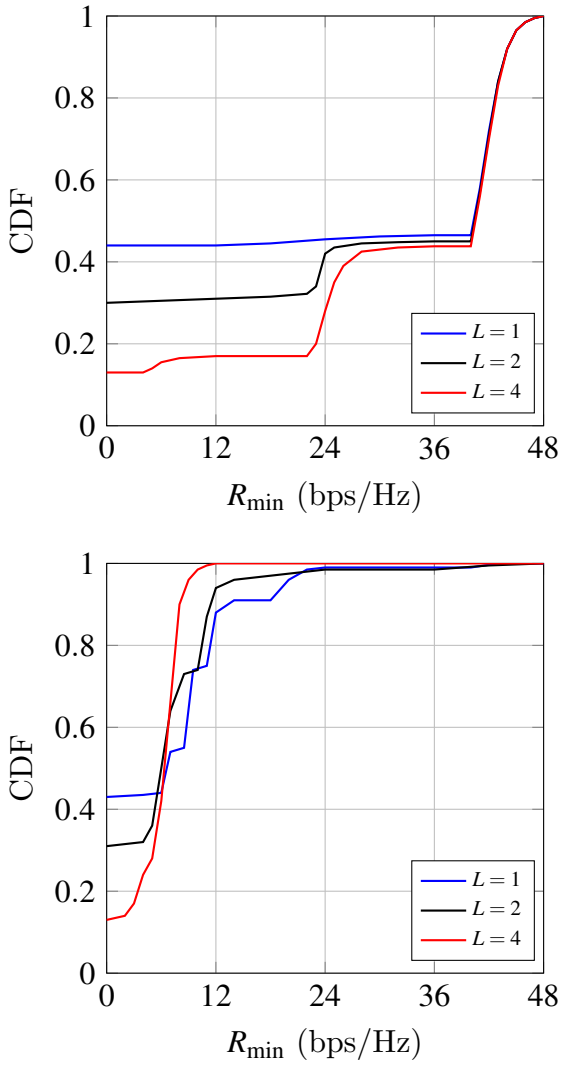


Figure 5.8: CDF of the minimum user rate for different numbers of participating LeRIS panels: (a) single-user case and (b) multi-user case.

rive closed-form localisation and orientation estimation methods. The analysis showed that five independent VCSEL measurements can recover the UE position and orientation, while dual-mode VCSEL operation can reduce this requirement to three VCSELs under suitable geometric conditions. The chapter also described a VCSEL-based mapping method that uses reflected optical signals to identify blocked and unobstructed links, enabling environment-aware LeRIS-assisted route selection. For multi-user access, a TDMA-based max-min optimisation problem was formulated to improve fairness by maximising the minimum user rate. Simulation results showed that the proposed VCSEL-based LeRIS framework achieved millimetre-level localisation accuracy,

improved blockage resilience, increased spectral efficiency, and enhanced multi-user fairness. Overall, this chapter demonstrated that VCSEL-based LeRIS can transform indoor PWEs into multi-functional platforms for joint localisation, mapping, and resilient mmWave communication. The findings from Chapters 3–5 are brought together in the final chapter, which summarises the thesis and outlines future research directions.

Appendix A: Levenberg–Marquardt Method for VCSEL-Based Localisation

The constrained localisation problem in Chapter 5 is solved using the Levenberg–Marquardt method. The objective is to iteratively refine the UE position estimate $\mathbf{r}$ by minimising the mismatch between the measured RSS vector and the modelled RSS vector. This method is suitable because the localisation problem is nonlinear in $\mathbf{r}$, while the orientation vector $\mathbf{n}$ can be estimated in closed form for each candidate position.

The residual vector is defined as

$$\mathbf{e}(\mathbf{r}) = \mathbf{V}(\mathbf{r})\hat{\mathbf{n}}(\mathbf{r}) - \mathbf{p}, \tag{A.1}$$

where $\mathbf{p}$ is the vector of measured received optical powers, $\mathbf{V}(\mathbf{r})$ is the localisation measurement matrix, and $\hat{\mathbf{n}}(\mathbf{r})$ is the orientation vector obtained for a fixed position $\mathbf{r}$. The ith residual term is written as

$$f_i(\mathbf{r},\mathbf{n}) = \beta_i(d_i)\mathbf{n}^{\mathrm{T}}\mathbf{u}_i - P_i, \tag{A.2}$$

where P_i is the measured received optical power from the ith VCSEL.

At iteration t, the Levenberg–Marquardt update is obtained by solving

$$\left(\mathbf{J}^{\mathrm{T}}\mathbf{J} + \mu\mathbf{I}_3\right)\Delta\mathbf{r} = -\mathbf{J}^{\mathrm{T}}\mathbf{e}, \tag{A.3}$$

where $\mathbf{J}$ is the Jacobian matrix of the residual vector with respect to $\mathbf{r}$, μ is the damping parameter, and $\Delta\mathbf{r}$ is the position update vector. The position estimate is then updated as

$$\mathbf{r}^{(t+1)} = \mathbf{r}^{(t)} + \Delta\mathbf{r}. \tag{A.4}$$

The damping parameter μ controls the behaviour of the algorithm. When μ is small, the update behaves similarly to the Gauss–Newton method and provides fast convergence near the solution. When μ is large, the update behaves more like a gradient-descent step, which improves stability when the current estimate is far from the optimum.

The iteration continues until the change in the position estimate or the reduction in the residual norm becomes sufficiently small. Therefore, the stopping condition can be written as

$$\|\Delta \mathbf{r}\|_2 \leq \varepsilon_{\mathrm{LM}} \quad \text{or} \quad \left| J(\mathbf{r}^{(t+1)}) - J(\mathbf{r}^{(t)}) \right| \leq \varepsilon_{\mathrm{J}}, \tag{A.5}$$

where $\varepsilon_{\mathrm{LM}}$ and ε_{J} are small positive convergence thresholds.

After convergence, the final position estimate is denoted by $\hat{\mathbf{r}}$, and the corresponding orientation estimate is obtained using (5.35). This completes the variable-projection implementation of the VCSEL-based localisation method.

Chapter 6

Conclusion and Future Work

6.1 Concluding Remarks

Drawing together the three technical contributions presented in the preceding chapters, this thesis investigated intelligent and adaptive OWC and sensing for future 6G indoor wireless networks. Specifically, the thesis focused on how programmable optical and hybrid wireless environments can improve security, localisation, mapping, blockage awareness, and multi-user communication in indoor scenarios.

In Chapter 3, delay-aware PLS was investigated for ORIS-assisted VLC systems. The motivation for this chapter was that conventional ORIS-assisted VLC studies primarily rely on the reflected path to enhance the received signal power, while the propagation delay introduced by the reflected path is often ignored. Therefore, this chapter explored whether delay can serve as an additional design resource to improve secrecy performance. Both single- and multiple-eavesdropper scenarios were considered, including non-colluding and colluding eavesdroppers. Moreover, delay-aware ORIS element allocation was developed to improve the legitimate receiver's channel while reducing information leakage to eavesdroppers. The results showed that, even in the worst-case geometry where the eavesdropper receives stronger optical power than the legitimate receiver, the secrecy capacity can still be enhanced by exploiting the time-delay difference between the direct and reflected optical paths. For the single-eavesdropper worst-case geometry, the proposed allocation improves the secrecy capacity by 253.7% at an optical trans-

mit power of 3 W compared with the LoS-only case. For multiple eavesdroppers, the proposed PPO-based allocation provides secrecy-capacity improvements of 107% and 235% for the colluding and non-colluding cases, respectively, compared with allocating all ORIS elements to the legitimate receiver.

In Chapter 4, non-uniform codebook design and NOMA-based resource allocation were studied for ORIS-assisted VLC systems. The motivation for this chapter was that practical ORIS deployment cannot rely on continuous mirror-angle optimisation, and a finite codebook is required for real-time beam steering. However, uniform angular codebooks do not provide uniform spatial coverage on the receiver plane due to the nonlinear mapping between mirror angles and reflected beam-hit points. To overcome this limitation, an element-wise non-uniform codebook was developed using GO. Moreover, the resulting codebook was connected to NOMA resource allocation through an ORIS gain matrix. The results showed that the proposed LoS+ORIS+SSA scheme improves the sum rate and the throughput–fairness trade-off compared with LoS-only and GRPA-based schemes. Over the considered ORIS-size range, the proposed framework increases the sum rate from approximately 4.4 bps/Hz to 9.6 bps/Hz, demonstrating the benefit of combining non-uniform beam control with optimised multi-user power allocation.

In Chapter 5, a VCSEL-based LeRIS framework was developed for integrated localisation, mapping, and mmWave communication. The motivation for this chapter was that future indoor wireless systems require not only high data rates, but also accurate environmental awareness. Therefore, the chapter introduced a VCSEL optical sensing model for estimating user position and orientation, and then extended the same sensing capability to obstacle-aware mapping. The mapped environment was subsequently used to support blockage-aware route selection for LeRIS-assisted mmWave communication. The results showed that VCSEL-based LeRIS can provide accurate localisation, improve blockage awareness, and enhance communication reliability in indoor environ-

ments. For the considered simulation settings, the proposed VCSEL-based framework achieves millimetre-level localisation accuracy, compared with centimetre-level accuracy for the LED-based LeRIS benchmark, while the resulting localisation and mapping information supports more reliable blockage-aware route selection.

Overall, this thesis demonstrated that ORIS and LeRIS technologies can play a central role in future indoor wireless networks. Specifically, the results showed that delay, optical beam steering, sensing information, and resource allocation can be jointly exploited to support secure, adaptive, and user-aware communication. Across the three technical contributions, the proposed methods achieve substantial improvements in secrecy capacity and multi-user sum rate, while improving localisation accuracy from the centimetre level to the millimetre level. These findings suggest that future indoor networks should use ORIS and LeRIS technologies as programmable components that can assist communication, localisation, sensing, and network optimisation.

6.2 Future Work

Although this thesis has demonstrated the potential of intelligent and adaptive OWC and sensing for future indoor 6G networks, several important research directions remain open.

First, future work can investigate the integration of semantic communication with OWC, VLC, ORIS, and LeRIS. In semantic communication, the objective is not only to transmit data accurately, but also to convey the information that is most relevant to a particular task. This is especially important in indoor 6G systems where communication, localisation, and sensing may operate jointly. For example, a VCSEL-based sensing system could extract task-relevant information such as blockage state, user mobility, beam-alignment requirements, or localisation confidence. This information could then

be used to support beam steering, route selection, and resource allocation without requiring all raw sensing measurements to be transmitted. Such an approach could reduce signalling overhead, improve energy efficiency, and enable faster environment-aware decision-making.

Second, the proposed framework can be extended towards digital-twin-assisted optical wireless networks. A digital twin could maintain a virtual representation of the indoor environment, including room geometry, user locations, obstacles, ORIS and LeRIS configurations, and channel conditions. The virtual environment could be continuously updated using optical sensing information and subsequently used to predict and optimise beam steering, route selection, codebook selection, and resource allocation. This would allow the network to move from reactive adaptation towards predictive environment-aware operation.

Third, deeper integration between optical sensing and hybrid RF/mmWave communication can be investigated. In this thesis, VCSELs are used to provide localisation and environmental information for mmWave communication. Future work could jointly optimise the optical sensing beams, LeRIS configurations, mmWave routes, and user scheduling. Machine-learning or RL methods could also be employed to support these decisions in dynamic indoor environments with moving users and time-varying blockage.

Fourth, practical hardware implementation and experimental validation are important directions for future research. The proposed VLC, ORIS, and LeRIS frameworks should be evaluated using physical testbeds to examine the effect of practical device limitations. Different implementation technologies, including micro-electro-mechanical system mirrors, liquid-crystal-based optical surfaces, spatial light modulators, and tunable metasurfaces, can be compared in terms of reflection efficiency, steering resolution, switching speed, optical loss, aperture size, fabrication complexity, and integration with optical transmitters and receivers. Such studies would help bridge the gap between analytical modelling and practical indoor deployment.

Finally, the optimisation frameworks developed in this thesis can be extended to more complex multi-user and security scenarios. The ORIS-assisted NOMA framework can be investigated for larger user populations, mobile users, and more practical quality-of-service requirements. Similarly, delay-aware PLS can be combined with adaptive beam control, artificial noise, user authentication, and more advanced security mechanisms to improve robustness against intelligent and mobile eavesdroppers.

Overall, these future research directions can extend the work of this thesis towards more intelligent, predictive, and task-aware indoor 6G networks, where optical sensing, programmable surfaces, semantic communication, digital twins, and hybrid wireless technologies operate together to support secure, adaptive, and environment-aware communication.

References

[1] J. G. Andrews, S. Buzzi, W. Choi, S. V. Hanly, A. Lozano, A. C. K. Soong and J. C. Zhang, 'What will 5G be?' *IEEE J. Sel. Areas Commun.*, vol. 32, no. 6, pp. 1065–1082, 2014.

[2] W. Jiang, B. Han, M. A. Habibi and H. D. Schotten, 'The road towards 6G: A comprehensive survey,' *IEEE Open J. Commun. Soc.*, vol. 2, pp. 334–366, 2021.

[3] International Telecommunication Union. 'Connecting humanity action blueprint: Closing the digital divide by 2030.' Accessed: Jun. 30, 2026. [Online]. Available: `https://www.itu.int/`

[4] Ericsson, 'Ericsson mobility report: Iot connections outlook and mobile traffic trends to 2031,' Telefonaktiebolaget LM Ericsson, Stockholm, Sweden, Tech. Rep., Jun. 2026. [Online]. Available: `https://www.ericsson.com/en/reports-and-papers/mobility-report`

[5] D. C. Nguyen, M. Ding, P. N. Pathirana, A. Seneviratne, J. Li, D. Niyato, O. A. Dobre and H. V. Poor, '6G internet of things: A comprehensive survey,' *IEEE Internet Things J.*, vol. 9, no. 1, pp. 359–383, 2022.

[6] W. Saad, M. Bennis and M. Chen, 'A vision of 6G wireless systems: Applications, trends, technologies, and open research problems,' *IEEE Netw.*, vol. 34, no. 3, pp. 134–142, 2020.

[7] International Telecommunication Union, 'Framework and overall objectives of the future development of IMT for 2030 and beyond,' ITU-R, Recommendation M.2160-0, 2023.

[8] M. Calabrese, 'Solving the spectrum crunch: Dynamic spectrum management systems,' *Dyn. Spectr. Alliance (DSA)*, Oct. 2023.

[9] T. S. Rappaport, Y. Xing, O. Kanhere, S. Ju, A. Madanayake, S. Mandal, A. Alkhateeb and G. C. Trichopoulos, 'Wireless communications and applications above 100 GHz: Opportunities and challenges for 6G and beyond,' *IEEE Access*, vol. 7, pp. 78 729–78 757, 2019.

[10] M. A. Khalighi and M. Uysal, 'Survey on free space optical communication: A communication theory perspective,' *IEEE Commun. Surveys Tuts.*, vol. 16, no. 4, pp. 2231–2258, 2014.

[11] M. Uysal and H. Nouri, 'Optical wireless communications: An emerging technology,' *IEEE Commun. Mag.*, vol. 54, no. 12, pp. 130–131, 2016.

[12] N. Saeed, S. Guo, K.-H. Park, T. Y. Al-Naffouri and M.-S. Alouini, 'Optical camera communications: Survey, use cases, challenges, and future trends,' *Physical Communication*, vol. 37, p. 100 900, 2019. DOI: 10.1016/j.phycom.2019.100900

[13] T. Komine and M. Nakagawa, 'Fundamental analysis for visible-light communication system using LED lights,' *IEEE Trans. Consum. Electron.*, vol. 50, no. 1, pp. 100–107, 2004.

[14] P. H. Pathak, X. Feng, P. Hu and P. Mohapatra, 'Visible light communication, networking, and sensing: A survey, potential and challenges,' *IEEE Commun. Surveys Tuts.*, vol. 17, no. 4, pp. 2047–2077, 2015.

[15] H. Haas, L. Yin, Y. Wang and C. Chen, 'What is LiFi?' *J. Lightw. Technol.*, vol. 34, no. 6, pp. 1533–1544, 2016.

[16] *IEEE standard for local and metropolitan area networks–part 15.7: Short-range optical wireless communications*, IEEE, 2019.

[17] *IEEE standard for multi-gigabit per second optical wireless communications (OWC), with ranges up to 200 m, for both stationary and mobile devices*, IEEE, 2023.

[18] A. Mostafa and L. Lampe, 'Physical-layer security for MISO visible light communication channels,' *IEEE J. Sel. Areas Commun.*, vol. 33, no. 9, pp. 1806–1818, 2015.

[19] M. A. Arfaoui, M. D. Soltani, I. Tavakkolnia, A. Ghrayeb, C. Assi and H. Haas, 'Physical layer security for visible light communication systems: A survey,' *IEEE Commun. Surveys Tuts.*, vol. 22, no. 3, pp. 1887–1908, 2020.

[20] J. Luo, L. Fan and H. Li, 'Indoor positioning systems based on visible light communication: State of the art,' *IEEE Commun. Surveys Tuts.*, vol. 19, no. 4, pp. 2871–2893, 2017.

[21] Z. Zhu, Y. Yang, M. Chen, C. Guo, J. Cheng and S. Cui, 'A survey on indoor visible light positioning systems: Fundamentals, applications, and challenges,' *IEEE Commun. Surveys Tuts.*, pp. 1–1, 2024.

[22] F. Liu, C. Masouros, A. P. Petropulu, H. Griffiths and L. Hanzo, 'Joint radar and communication design: Applications, state-of-the-art, and the road ahead,' *IEEE Trans. Commun.*, vol. 68, no. 6, pp. 3834–3862, 2020.

[23] K. Lee, H. Park and J. R. Barry, 'Indoor channel characteristics for visible light communications,' *IEEE Commun. Lett.*, vol. 15, no. 2, pp. 217–219, 2011.

[24] Y. S. Eroglu, Y. Yapici and I. Guvenc, 'Impact of random receiver orientation on visible light communications channel,' *IEEE Trans. Commun.*, vol. 67, no. 2, pp. 1313–1325, 2019.

[25] M. D. Soltani, A. A. Purwita, I. Tavakkolnia, H. Haas and M. Safari, 'Impact of device orientation on error performance of LiFi systems,' *IEEE Access*, vol. 7, pp. 41 690–41 701, 2019.

[26] M. D. Soltani, M. A. Arfaoui, I. Tavakkolnia, A. Ghrayeb, M. Safari, C. Assi, M. Hasna and H. Haas, 'Bidirectional optical spatial modulation for mobile users: Toward a practical design for LiFi systems,' *IEEE J. Sel. Areas Commun.*, vol. 37, no. 9, pp. 2069–2086, 2019.

[27] S. Aboagye, A. R. Ndjiongue, T. M. N. Ngatched, O. A. Dobre and H. V. Poor, 'RIS-assisted visible light communication systems: A tutorial,' *IEEE Commun. Surveys Tuts.*, vol. 25, no. 1, pp. 251–288, 2023.

[28] G. Pan, J. Ye and Z. Ding, 'On secure VLC systems with spatially random terminals,' *IEEE Commun. Lett.*, vol. 21, no. 3, pp. 492–495, 2017.

[29] S. Cho, G. Chen and J. P. Coon, 'Securing visible light communication systems by beamforming in the presence of randomly distributed eavesdroppers,' *IEEE Trans. Wireless Commun.*, vol. 17, no. 5, pp. 2918–2931, 2018.

[30] S. Sun, F. Yang, J. Song and R. Zhang, 'Intelligent reflecting surface for MIMO VLC: Joint design of surface configuration and transceiver signal processing,' *IEEE Trans. Wireless Commun.*, vol. 22, no. 9, pp. 5785–5799, 2023.

[31] S. Sun, W. Mei, F. Yang, N. An, J. Song and R. Zhang, 'Optical intelligent reflecting surface assisted MIMO VLC: Channel modeling and capacity characterization,' *IEEE Trans. Wireless Commun.*, vol. 23, no. 3, pp. 2125–2139, 2024.

[32] L. Qian, X. Chi, L. Zhao and A. Chaaban, 'Secure visible light communications via intelligent reflecting surfaces,' in *Proc. IEEE Int. Conf. Commun.*, 2021, pp. 1–6.

[33] H. Abumarshoud and M. Biagi, 'Intelligent reflecting surface-aided visible light communications for granting indoor secrecy,' in *Proc. IEEE Int. Conf. Commun.*, Jun. 2024, pp. 3701–3706.

[34] L. Qian, L. Zhao, N. Huang, A. Chaaban and Z. Xu, 'Security enhancement by intelligent reflecting surfaces for visible light communications,' *Opt. Commun.*, vol. 570, p. 130 851, Nov. 2024.

[35] R. Iqbal, M. Biagi, A. Zoha, M. A. Imran and H. Abumarshoud, 'Leveraging IRS induced time delay for enhanced physical layer security in VLC systems,' *IEEE Wireless Commun. Lett.*, vol. 13, no. 11, pp. 3147–3151, 2024.

[36] R. Iqbal, A. Zoha, S. Ikki, M. A. Imran and H. Abumarshoud, 'Enhancing PLS of indoor IRS-VLC systems for colluding and non-colluding eavesdroppers,' *IEEE Open J. Commun. Soc.*, 2026, Early access.

[37] R. Iqbal, D. Bozanis, D. Tyrovolas, C. K. Liaskos, M. A. Imran, G. K. Karagiannidis and H. Abumarshoud, 'Non-uniform codebook design for optical IRS-assisted VLC systems,' in *Proc. IEEE BalkanCom*, Accepted, 2026.

[38] Z. Zeng, M. D. Soltani, M. Safari and H. Haas, 'A VCSEL array transmission system with novel beam activation mechanisms,' *IEEE Trans. Commun.*, vol. 70, no. 3, pp. 1886–1900, 2022.

[39] E. Sarbazi, H. Kazemi, M. D. Soltani, M. Safari and H. Haas, 'A Tb/s indoor optical wireless access system using VCSEL arrays,' in *Proc. IEEE Int. Symp. Pers., Indoor Mobile Radio Commun. (PIMRC)*, 2020, pp. 1–6.

[40] R. Ahmad, H. Kazemi, E. Sarbazi and H. Haas, 'Joint position and orientation estimation in VCSEL-based LiFi networks: A deep learning approach,' in *Proc. IEEE Global Commun. Conf.*, 2023, pp. 3676–3681.

[41] T. S. Rappaport, S. Sun, R. Mayzus, H. Zhao, Y. Azar, K. Wang, G. N. Wong, J. K. Schulz, M. Samimi and F. Gutierrez, 'Millimeter wave mobile communications for 5G cellular: It will work!' *IEEE Access*, vol. 1, pp. 335–349, 2013.

[42] M. R. Akdeniz, Y. Liu, M. K. Samimi, S. Sun, S. Rangan, T. S. Rappaport and E. Erkip, 'Millimeter wave channel modeling and cellular capacity evaluation,' *IEEE J. Sel. Areas Commun.*, vol. 32, no. 6, pp. 1164–1179, 2014.

[43] D. Tyrovolas, D. Bozanis, S. A. Tegos, V. K. Papanikolaou, P. D. Diamantoulakis, C. K. Liaskos, R. Schober and G. K. Karagiannidis, 'Empowering programmable wireless environments with optical anchor-based positioning,' *IEEE Netw.*, vol. 39, no. 1, pp. 14–20, 2025.

[44] J. M. Kahn and J. R. Barry, 'Wireless infrared communications,' *Proc. IEEE*, vol. 85, no. 2, pp. 265–298, 1997.

[45] Z. Ghassemlooy, W. Popoola and S. Rajbhandari, *Optical Wireless Communications: System and Channel Modelling with MATLAB*, 2nd ed. CRC Press, 2019.

[46] A. G. Bell, 'On the production and reproduction of sound by light,' *Am. J. Sci.*, vol. 20, no. 118, pp. 305–324, 1880.

[47] F. R. Gfeller and U. Bapst, 'Wireless in-house data communication via diffuse infrared radiation,' *Proc. IEEE*, vol. 67, no. 11, pp. 1474–1486, 1979.

[48] J. B. Carruthers and J. M. Kahn, 'Modeling of nondirected wireless infrared channels,' *IEEE Trans. Commun.*, vol. 45, no. 10, pp. 1260–1268, 1997.

[49] H. Le Minh, D. O'Brien, G. Faulkner, L. Zeng, K. Lee, D. Jung, Y. Oh and E. T. Won, '100-Mb/s NRZ visible light communications using a postequalized white LED,' *IEEE Photon. Technol. Lett.*, vol. 21, no. 15, pp. 1063–1065, 2009.

[50] H. Elgala, R. Mesleh and H. Haas, 'Indoor optical wireless communication: Potential and state-of-the-art,' *IEEE Commun. Mag.*, vol. 49, no. 9, pp. 56–62, 2011.

[51] S. Dimitrov and H. Haas, *Principles of LED Light Communications: Towards Networked Li-Fi*. Cambridge University Press, 2015.

[52] H. Abumarshoud, L. Mohjazi, O. A. Dobre, M. Di Renzo, M. A. Imran and H. Haas, 'LiFi through reconfigurable intelligent surfaces: A new frontier for 6G?' *IEEE Veh. Technol. Mag.*, vol. 17, no. 1, pp. 37–46, Mar. 2022. DOI: 10.1109/MVT.2021.3121647

[53] M. D. Soltani, E. Sarbazi, N. Bamiedakis, P. de Souza, H. Kazemi, J. M. H. Elmirghani, I. H. White, R. V. Penty, H. Haas and M. Safari, 'Safety analysis for laser-based optical wireless communications: A tutorial,' *Proceedings of the IEEE*, vol. 110, no. 8, pp. 1045–1072, 2022. DOI: 10.1109/JPROC.2022.3181968

[54] A. Tishchenko, M. Khalily, A. Shojaeifard, F. Burton, E. Bjornson, M. Di Renzo and R. Tafazolli, 'The emergence of multi-functional and hybrid reconfigurable intelligent surfaces for integrated sensing and communications – a survey,' *IEEE Commun. Surveys Tuts.*, pp. 1–1, 2025.

[55] J. Armstrong, 'OFDM for optical communications,' *J. Lightw. Technol.*, vol. 27, no. 3, pp. 189–204, 2009.

[56] P. Djahani and J. M. Kahn, 'Analysis of infrared wireless links employing multibeam transmitters and imaging diversity receivers,' *IEEE Trans. Commun.*, vol. 48, no. 12, pp. 2077–2088, 2000.

[57] Z. Wang, D. Tsonev, S. Videv and H. Haas, 'On the design of a solar-panel receiver for optical wireless communications with simultaneous energy harvesting,' *IEEE J. Sel. Areas Commun.*, vol. 33, no. 8, pp. 1612–1623, 2015.

[58] Z. Zeng, M. D. Soltani, M. Safari and H. Haas, 'Angle diversity receiver in LiFi cellular networks,' in *Proc. IEEE Int. Conf. Commun.*, 2019, pp. 1–6.

[59] H. Marshoud, P. C. Sofotasios, S. Muhaidat, G. K. Karagiannidis and B. S. Sharif, 'Visible light communications in the presence of interference and noise,' *IEEE Trans. Commun.*, vol. 64, no. 9, pp. 3803–3818, 2016.

[60] S. M. R. Islam, N. Avazov, O. A. Dobre and K.-S. Kwak, 'Power-domain non-orthogonal multiple access (NOMA) in 5G systems: Potentials and challenges,' *IEEE Commun. Surveys Tuts.*, vol. 19, no. 2, pp. 721–742, 2017.

[61] C. Liaskos, S. Nie, A. Tsioliaridou, A. Pitsillides, S. Ioannidis and I. Akyildiz, 'A new wireless communication paradigm through software-controlled metasurfaces,' *IEEE Commun. Mag.*, vol. 56, no. 9, pp. 162–169, 2018.

[62] R. Iqbal, D. Bozanis, D. Tyrovolas, C. K. Liaskos, M. A. Imran, G. K. Karagiannidis and H. Abumarshoud, 'Enabling mmWave communications with VCSEL-based light-emitting reconfigurable intelligent surfaces,' in *Proc. IEEE Int. Conf. Commun.*, 2026.

[63] D. J. Love, R. W. Heath, V. K. N. Lau, D. Gesbert, B. D. Rao and M. Andrews, 'An overview of limited feedback in wireless communication systems,' *IEEE J. Sel. Areas Commun.*, vol. 26, no. 8, pp. 1341–1365, 2008.

[64] S. Kutty and D. Sen, 'Beamforming for millimeter wave communications: An inclusive survey,' *IEEE Commun. Surveys Tuts.*, vol. 18, no. 2, pp. 949–973, 2016.

[65] A. D. Wyner, 'The wire-tap channel,' *Bell Syst. Tech. J.*, vol. 54, no. 8, pp. 1355–1387, 1975.

[66] M. Bloch and J. Barros, *Physical-Layer Security: From Information Theory to Security Engineering*. Cambridge University Press, 2011.

[67] R. Iqbal, D. Bozanis, D. Tyrovolas, C. K. Liaskos, M. A. Imran, G. K. Karagiannidis and H. Abumarshoud, 'Non-uniform codebook design for uniform spatial mapping with NOMA-based OIRS-assisted VLC,' submitted for publication, 2026.

[68] H. Marshoud, P. C. Sofotasios, S. Muhaidat and G. K. Karagiannidis, 'Non-orthogonal multiple access for visible light communications,' *IEEE Photon. Technol. Lett.*, vol. 28, no. 1, pp. 51–54, 2016.

[69] L. Yin, X. Wu and H. Haas, 'Performance evaluation of non-orthogonal multiple access in visible light communication,' *IEEE Trans. Commun.*, vol. 64, no. 12, pp. 5162–5175, 2016.

[70] D. Bozanis, N. G. Evgenidis, V. K. Papanikolaou, P. S. Bouzinis, S. A. Tegos, A. A. Dowhuszko, P. D. Diamantoulakis and G. K. Karagiannidis, 'Indoor 3D visible light positioning analysis with channel estimation errors,' in *Proc. Int. Conf. Syst., Signals Image Process. (IWSSIP)*, 2023, pp. 1–4.

[71] D. Bozanis, D. Tyrovolas, V. K. Papanikolaou, S. A. Tegos, P. D. Diamantoulakis, C. K. Liaskos, R. Schober and G. K. Karagiannidis, 'Closed-form location and orientation estimation in optical wireless systems,' in *Proc. IEEE Wireless Commun. Netw. Conf.*, 2025, pp. 1–6.

[72] O. E. Ayach, S. Rajagopal, S. Abu-Surra, Z. Pi and R. W. Heath, 'Spatially sparse precoding in millimeter wave MIMO systems,' *IEEE Trans. Wireless Commun.*, vol. 13, no. 3, pp. 1499–1513, 2014.

[73] A. Arafa, E. Panayirci and H. V. Poor, 'Relay-aided secure broadcasting for visible light communications,' *IEEE Trans. Commun.*, vol. 67, no. 6, pp. 4227–4239, 2019.

[74] A. Mostafa and L. Lampe, 'Physical-layer security for indoor visible light communications,' in *Proc. IEEE Int. Conf. Commun.*, 2014, pp. 3342–3347.

[75] H. Abumarshoud, M. D. Soltani, M. Safari and H. Haas, 'Realistic secrecy performance analysis for LiFi systems,' *IEEE Access*, vol. 9, pp. 120 675–120 688, 2021.

[76] M. Haider, A. E. Aziz and R. Iqbal, 'Can IRS assist PLS for indoor VLC?' *Phys. Commun.*, vol. 71, p. 102 703, Aug. 2025.

[77] V. Jungnickel, V. Pohl, S. Nönnig and C. von Helmolt, 'A physical model of the wireless infrared communication channel,' *IEEE Journal on Selected Areas in Communications*, vol. 20, no. 3, pp. 631–640, Apr. 2002. DOI: 10.1109/49.995522

[78] C. Chen, S. Huang, H. Abumarshoud, I. Tavakkolnia, M. Safari and H. Haas, 'Frequency-domain channel characteristics of intelligent reflecting surface assisted visible light communication,' *J. Lightw. Technol.*, 2023.

[79] A. M. Khalid, J. P. Linnartz, P. V. Voorthuisen, X. Deng and S. Mardanikorani, 'Productization experiences of G.vlc (ITU) based LiFi system for high speed indoor wireless access,' in *1st Optical Wireless Communication Conference (OWCC)*, 2020.

[80] S. Mardanikorani, X. Deng and J.-P. M. G. Linnartz, 'Sub-carrier loading strategies for DCO-OFDM LED communication,' *IEEE Trans. Commun.*, vol. 68, no. 2, pp. 1101–1117, 2020.

[81] M. D. Higgins, R. J. Green and M. S. Leeson, 'A genetic algorithm method for optical wireless channel control,' *J. Lightw. Technol.*, vol. 27, no. 6, pp. 760–772, 2009.

[82] D. Bozanis, N. A. Mitsiou, S. A. Tegos, P. D. Diamantoulakis, G. K. Karagiannidis and V. K. Papanikolaou, 'On the beamforming design of cross-band OWC/RF cell-free MIMO,' *IEEE Commun. Lett.*, pp. 1–1, 2025.

[83] A. R. Hussen, R. Iqbal, A. Zoha, M. A. Imran and H. Abumarshoud, 'Sum rate maximisation for IRS-assisted VLC using reinforcement learning,' in *Proc. IEEE Middle East Conf. Commun. Netw. (MECOM)*, 2024, pp. 464–469.

[84] H. Abumarshoud, C. Chen, I. Tavakkolnia, H. Haas and M. A. Imran, 'Intelligent reflecting surfaces for enhanced physical layer security in NOMA VLC systems,' in *Proc. IEEE Int. Conf. Commun.*, 2023, pp. 3284–3289.

[85] C. Liaskos, A. Tsioliaridou, S. Nie, A. Pitsillides, S. Ioannidis and I. F. Akyildiz, 'On the network-layer modeling and configuration of programmable wireless environments,' *IEEE/ACM Trans. Netw.*, vol. 27, no. 4, pp. 1696–1713, 2019.

[86] Z. Zhang, Y. Xiao, Z. Ma, M. Xiao, Z. Ding, X. Lei, G. K. Karagiannidis and P. Fan, '6G wireless networks: Vision, requirements, architecture, and key technologies,' *IEEE Commun. Surveys Tuts.*, vol. 23, no. 1, pp. 70–120, 2021.

[87] E. Basar, M. Di Renzo, J. de Rosny, M. Debbah, M.-S. Alouini and R. Zhang, 'Wireless communications through reconfigurable intelligent surfaces,' *IEEE Access*, vol. 7, pp. 116 753–116 773, 2019.

[88] M. Di Renzo, A. Zappone, M. Debbah, M.-S. Alouini, C. Yuen, J. de Rosny and S. Tretyakov, 'Smart radio environments empowered by reconfigurable intelligent surfaces: How it works, state of research, and the road ahead,' *IEEE J. Sel. Areas Commun.*, vol. 38, no. 11, pp. 2450–2525, 2020.

[89] N. Chaudhary, O. I. Younus, L. N. Alves, Z. Ghassemlooy, S. Zvanovec and H. Le-Minh, 'An indoor visible light positioning system using tilted LEDs with high accuracy,' *Sensors*, vol. 21, no. 3, p. 920, Jan. 2021.

[90] G. Golub and V. Pereyra, 'Separable nonlinear least squares: The variable projection method and its applications,' *Inverse Probl.*, vol. 19, R1–R26, 2003.

[91] D. Tyrovolas, S. A. Tegos, E. C. Dimitriadou-Panidou, P. D. Diamantoulakis, C. K. Liaskos and G. K. Karagiannidis, 'Performance analysis of cascaded reconfigurable intelligent surface networks,' *IEEE Wireless Commun. Lett.*, vol. 11, no. 9, pp. 1855–1859, 2022.